

Pentacoordinate Cobalt(II) Single Ion Magnets with Pendant Alkyl Chains: Shall We Go for Chloride or Bromide?

Jana Juráková,^a Jana Dubnická Midlíková,^a Jakub Hrubý,^a Andrii Kliukov,^b Vinicius Tadeu Santana,^a Ján Pavlik,^c Ján Moncoľ,^c Erik Čižmár,^b Milan Orlita,^d Ivan Mohelský,^d Petr Neugebauer,^a Denis Gentili,^e Massimiliano Cavallini,^e Ivan Šalitroš^{acf*}

a) Central European Institute of Technology, Brno University of Technology, Purkyňova 123, 61200 Brno Czech Republic

b) Institute of Physics, Faculty of Science, P.J. Šafárik University Park Angelinum 9, 04154 Košice, Slovakia

c) Department of Inorganic Chemistry, Faculty of Chemical and Food Technology, Slovak University of Technology in Bratislava. Bratislava SK-81237, Slovakia. *e-mail: ivan.salitros@stuba.sk

d) LNCMI-EMFL, CNRS UPR3228, Univ. Grenoble Alpes, Univ. Toulouse, Univ. Toulouse 3, INSA-T, Grenoble and Toulouse, France

e) Consiglio Nazionale delle Ricerche, Istituto per lo Studio dei Materiali Nanostrutturati (CNR-ISMN) Via P. Gobetti 101, 40129 Bologna, Italy.

f) Department of Inorganic Chemistry, Faculty of Science, Palacký University, 17. listopadu 12, 771 46 Olomouc, Czech Republic

S1 Experimental section

Materials and methods

1-Iodooctane p.a.; K₂CO₃; Dimethylformamide p.a.; 1-Bromododecane p.a.; Acetonitrile p.a.; Dichloromethane p.a.; CoCl₂ · 6H₂O; CoBr₂ · 6H₂O; Chloroform p.a.

Chemicals were purchased from Sigma-Aldrich and Mikrochem used as received without any further purification. The starting material 2,6-bis(benzimidazol-2-yl)pyridine was prepared according to the previously reported procedure.¹ IR spectra in the interval from 4000 to 400 cm⁻¹ of herein reported compounds were measured on Nicolet 5700 spectrometer (ATR technique). Elemental analysis of carbon, hydrogen and nitrogen was carried out by EA CHNS(O) Flash 1112 machine. The NMR spectra were recorded on Bruker DPX 500 spectrometer. The UV-VIS spectra were measured in solid state on Specord 200 spectrophotometer in the range of 800 – 200 nm. DSC measurement was performed using a differential scanning calorimeter Shimadzu DSC-60 (Tokyo, Japan) cooled with liquid nitrogen. A sample of 3.67 mg was placed into a standard aluminum pan, cooled down to 140 K at -5 K/min and reheated at 5 K/min to 200 K. The temperature scale of the instrument was calibrated to s/s transition of cyclohexane.

Synthesis

Synthesis of 2,6-bis(1-octyl-1H-benzimidazol-2-yl)pyridine (L1)

50 ml round-bottom flask was charged with 2,6-bis(benzimidazol-2-yl)pyridine (0.5 g, 1.6 mmol, 1eq) and dissolved in 10 ml DMF. Then, K₂CO₃ (1.11g, 8.0 mmol, 5eq) was added into the solution and suspension was stirred for 2 hours at 70°C. 1-iodooctane (0.70 ml, 4.0 mmol, 2.5eq) was added dropwise over the stirring suspension. The reaction mixture was refluxed at 120°C for 36 hours and cooled down to room temperature. Solvent was removed by vacuum distillation, the residue was treated with distilled water (50 ml) and extracted with CH₂Cl₂ (3 x 200 ml). The chloroform solvent was removed using a rotary evaporator and the oily residue was column chromatographed on silica gel with CHCl₃/methanol (100:1) as an eluent. The main product **L1** was isolated as first fraction ($R_f = 0.59$) in 71 % (0.6 g, 0.71mmol) yield as orange oily liquid. The minor side-product of this reaction – 2-(6-(1H-benzimidazol-2-yl)pyridin-2-yl)-1-octyl-1H-benzimidazole (**L1_m**) was collected as the second and more polar fraction ($R_f = 0.54$) in 15 % (0.1 g, 0.15 mmol) yield form as yellowish powder.

L1: FT-IR (ATR, $\tilde{\nu}_{\text{max}}/\text{cm}^{-1}$): 2923, 2853 (m, v(C_{al}-H)); 1571, 1434, 1409 (m, v(C_{ar}-C_{ar}) and/or v(CN)), 740 (s, δ(CH)). ¹H NMR (300 MHz, d₆-DMSO, 25 °C, δ/ppm): 8.32 (d, J = 1.5 Hz, 1 H), 8.29 (d, 1 H), 8.23-8.18 (m, 1 H), 7.76-7.74 (m, 2 H), 7.68 (dd, J₁ = 7.1 Hz, J₂ = 1.2 Hz, 2 H), 7.3 (m, 4 H), 4.73 (t, J = 7.2 Hz, 4 H, -N-CH₂), 1.64 (p, J = 7.0 Hz, 4 H, -N-CH₂-CH₂), 1.05-0.84 (m, 20 H), 0.66 (t, 6 Hz, -CH₃). ¹³C NMR (75 MHz, d₆-DMSO, 25 °C, δ/ppm): 149.57, 149.48, 142.27, 138.47, 136.03, 125.14, 123.13, 122.27, 119.62, 110.86, 44.06, 30.87, 29.43, 28.41, 28.21, 25.82, 21.84, 13.68. UV-VIS (nujol, λ/nm): 251 (π→π*), 346 (n→π*)

L1_m: FT-IR (ATR, $\tilde{\nu}_{\text{max}}/\text{cm}^{-1}$): 3399 (m, v(N-H)); 3038 (m, v(C_{ar}-H)); (2920(m, v(C_{al}-H)); 1570, 1499, 1449, 1408 (m, v(C_{ar}-C_{ar}) or v(CN)); 730,720 (s, δ(CH) and/or ρ(CH₂)_n). ¹H NMR (300 MHz, d₆-DMSO, 25 °C, δ/ppm): 8.45 (d, J = 7.7 Hz, 1 H), 8.31 – 8.28 (m, 1 H), 8.18 (t, J = 7.8 Hz, 1 H), 7.77 (dd, J₁ = 7.6 Hz, J₂ = 3.1 Hz, 2 H), 7.69 (dd, J₁ = 6.0 Hz, J₂ = 3.2 Hz, 2 H), 7.38-7.25 (m, 4 H), 5.0 (t, J = 7.2 Hz, 2 H, -N-CH₂), 1.59 (p, J = 6.9 Hz, 2 H, -N-CH₂-CH₂), 1.06-0.79 (m, 10 H), 0.60 (t, J = 3 H, -CH₃). ¹³C NMR (75 MHz, d₆-DMSO, 25 °C, δ/ppm): 150.05, 149.28, 148.00, 142.05, 138.69, 136.29, 125.28, 123.33, 122.78, 122.40, 122.05, 119.60, 110.96, 44.38, 30.91, 29.46, 28.41, 28.15, 25.89, 21.84, 13.71. UV-VIS (nujol, λ/nm): 251 (π→π*), 331 (n→π*)

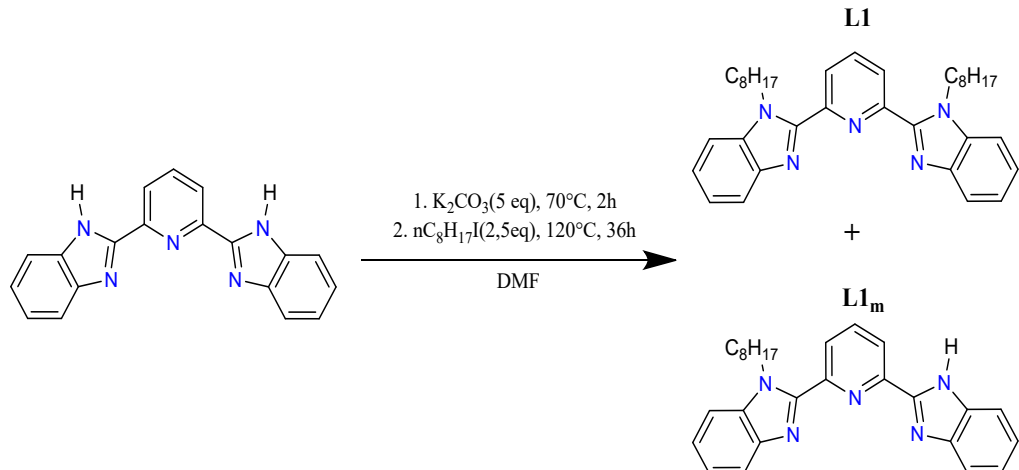


Figure S1 Scheme of synthesis of ligands L1 and L1_m.

Synthesis of 2,6-bis(1-dodecyl-1H-benzimidazol-2-yl)-pyridine (L2)

50 ml round-bottom flask was charged with 2,6-bis(benzimidazol-2-yl)pyridine (0.5 g, 1.6 mmol, 1eq) and dissolved in 10 ml DMF. Then, K₂CO₃ (1.11 g, 8.0 mmol, 5eq) was added into the solution and suspension was stirred for 2 hours at 70 °C. 1-bromododecane (0.95 ml, 4.0 mmol, 2.5 eq) was added dropwise over the stirring suspension. The reaction mixture was refluxed at 120°C for 36 hours and cooled down to room temperature. Solvent was removed by vacuum distillation, the residue was treated with distilled water (50 ml) and extracted with CH₂Cl₂ (3 x 200 ml). The organic fractions were combined and CH₂Cl₂ solvent was removed using a rotary evaporator. The oily residue was column chromatographed on silica gel with CHCl₃/methanol (100:1) as an eluent (R_f = 0.55). The combined slightly yellow solutions yielded upon evaporation and drying in vacuum to 0.83 g (1.28 mmol, 80 %) of yellowish oily liquid.

Elemental analysis for C₄₃H₆₁N₅ (M_w = 648.00 g·mol⁻¹) found % (expected %): C 80.00 (79.70); N 10.90 (10.81); H 9.50 (9.49). FT-IR (ATR, $\tilde{\nu}_{\text{max}}/\text{cm}^{-1}$): 2921, 2851 (s, v(C_{al}-H)); 1572, 1452, 1435 (m, vC_{ar}-C_{ar} or v(CN)), 741 (s, δ CH). ¹H NMR (300 MHz, CDCl₃, 25 °C, δ/ppm): 8.33 (d, J = 7 Hz, 2 H), 8.08-8.03 (m, 1 H), 7.90-7.87 (m, 2 H), 7.49-7.45 (m, 2 H), 7.40-7.32 (m, 4H), 4.71 (t, J = 7.3 Hz, 4 H, N-CH₂), 1.74 (p, J = 7 Hz, 4H, N-CH₂-CH₂), 1.29-1.01 (m, 36 H), 0.9-0.86 (m, 6 H). ¹³C NMR (300 MHz, CDCl₃, 25 °C, δ/ppm): 150.00, 149.89,

142.68, 137.91, 136.12, 125.29, 123.30, 122.54, 127.17, 110.16, 44.74, 31.75, 29.92, 29.38, 29.37, 29.24, 29.21, 29.15, 28.93, 26.53, 22.53, 13.98. UV-VIS (nujol, λ/nm): 246 ($\pi\rightarrow\pi^*$), 340 ($n\rightarrow\pi^*$).

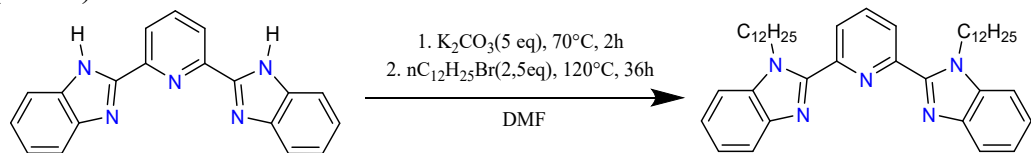


Figure S2 Scheme of synthesis of ligand L2.

*Synthesis of complexes **1** [$\text{Co}(\text{L1})\text{Cl}_2$] and **2** [$\text{Co}(\text{L1})\text{Br}_2$]*

$\text{CoCl}_2 \cdot 6\text{H}_2\text{O}$ (44 mg, 0.19 mmol, 1 eq) or $\text{CoBr}_2 \cdot 6\text{H}_2\text{O}$ (61 mg, 0.19 mmol, 1 eq) was dissolved in 5 ml of acetonitrile and added into the acetonitrile solution (40 ml) of ligand **L1** (100 mg, 0.19 mmol, 1 eq). When Co(II) salt was added, the yellow to green color change occurred immediately without the formation of precipitation. Reaction mixture was refluxed overnight, filtered and mother liquor was submitted for the controlled crystallization at room temperature. The green crystals of **1** or **2** were collected by filtration after several days.

Complex 1 [$\text{Co}(\text{L1})\text{Cl}_2$]: Yield 39% (49 mg, 0.07 mmol). Elemental analysis for $\text{C}_{35}\text{H}_{45}\text{Cl}_2\text{CoN}_5$ ($M_w = 665.60 \text{ g mol}^{-1}$) found % (expected %): C 62.79 (63.16); N 10.09 (10.52); H 6.66 (6.81). FT-IR (ATR, $\tilde{\nu}_{\text{max}}/\text{cm}^{-1}$): 3060 (m, $\nu(\text{C}_{\text{ar}}-\text{H})$, 2923, 2853 (m, $\nu(\text{C}_{\text{al}}-\text{H})$); 1514, 1485, 1456, 1436 (m, $\nu(\text{C}_{\text{ar}}-\text{C}_{\text{ar}})$ and/or $\nu(\text{CN})$), 774, 749, 734 (s, $\delta(\text{CH})$). UV-VIS (nujol, λ/nm): 213 ($\pi\rightarrow\pi^*$), 323 ($n\rightarrow\pi^*$), 636, 669, 712 (MLCT and/or d-d)

Complex 2 [$\text{Co}(\text{L1})\text{Br}_2$]: Yield 34% (49 mg, 0.06 mmol). Elemental analysis for $\text{C}_{35}\text{H}_{45}\text{Br}_2\text{CoN}_5$ ($M_w = 754.52 \text{ g mol}^{-1}$) found % (expected %): C 54.41 (55.72); N 8.99 (9.28); H 5.92 (6.01). FT-IR (ATR, $\tilde{\nu}_{\text{max}}/\text{cm}^{-1}$): 2918, 2855 (m, $\nu(\text{C}_{\text{al}}\text{H})$); 1597, 1432 (m, $\nu(\text{C}_{\text{ar}}-\text{C}_{\text{ar}})$ or $\nu(\text{CN})$), 748 (s, $\delta(\text{CH})$). UV-VIS (nujol, λ/nm): 206 ($\pi\rightarrow\pi^*$), 330 ($n\rightarrow\pi^*$), 579, 633 (MLCT and/or d-d).

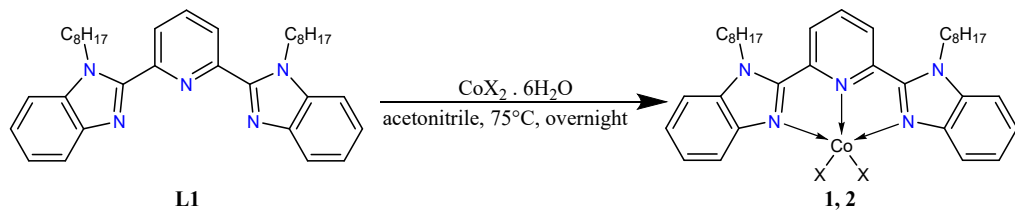


Figure S3 Scheme of synthesis of complexes **1** ($X = \text{Cl}$) and **2** ($X = \text{Br}$).

*Synthesis of complexes **3** [$\text{Co}(\text{L2})\text{Cl}_2$] and **4** [$\text{Co}(\text{L2})\text{Br}_2$]*

$\text{CoCl}_2 \cdot 6\text{H}_2\text{O}$ (36 mg, 0.15 mmol, 1 eq) or $\text{CoBr}_2 \cdot 6\text{H}_2\text{O}$ (50 mg, 0.15 mmol, 1 eq) was dissolved in 5 ml of acetonitrile and added into the acetonitrile solution (40 ml) of ligand **L2** (100 mg, 0.15 mmol, 1 eq). When Co(II) salt was added, the slightly yellowish solution turned to green immediately and no precipitation occurred. Reaction mixture was refluxed overnight, filtered and mother liquor was submitted for the controlled crystallization at room temperature. After several days, green crystals of **3** or **4** were collected by filtration.

Complex 3 [$\text{Co}(\text{L2})\text{Cl}_2$]: Yield 35% (51 mg, 0.05 mmol). Elemental analysis for $\text{C}_{43}\text{H}_{61}\text{Cl}_2\text{CoN}_5$ ($M_w = 777.83 \text{ g mol}^{-1}$) found % (expected %): C 66.52 (66.40); N 9.12 (9.00); H 7.85 (7.90). FT-IR (ATR, $\tilde{\nu}_{\text{max}}/\text{cm}^{-1}$): 2923, 2850 (s, $\nu(\text{C}_{\text{al}}-\text{H})$); 1599, 1477, 1458, 1432 (m, $\nu(\text{C}_{\text{ar}}-\text{C}_{\text{ar}})$ and/or $\nu(\text{CN})$), 747 (s, $\delta(\text{CH})$). 720 (sh, $\rho(\text{CH}_2)n$). UV-VIS (nujol, λ/nm): 210 ($\pi\rightarrow\pi^*$), 335 ($n\rightarrow\pi^*$), 625 (MLCT and/or d-d)

Complex 4 [$\text{Co}(\text{L2})\text{Br}_2$]: Yield 40% (52 mg, 0.06 mmol). Elemental analysis for $\text{C}_{43}\text{H}_{61}\text{Br}_2\text{CoN}_5$ ($M_w = 866.74 \text{ g mol}^{-1}$) found % (expected %): C 58.39 (59.59); N 7.47 (8.08);

H 7.01 (7.09). FT-IR (ATR, $\tilde{\nu}_{\text{max}}/\text{cm}^{-1}$): 2917, 2849 (m, v(C_{al}H)); 1599, 1467, 1432 (m, vC_{ar}-C_{ar} or v(CN)); 747 (s, δ (CH)). UV-VIS (nujol, λ/nm): 204 ($\pi \rightarrow \pi^*$), 335 (n → π*), 580, 631 (MLCT and/or d-d).

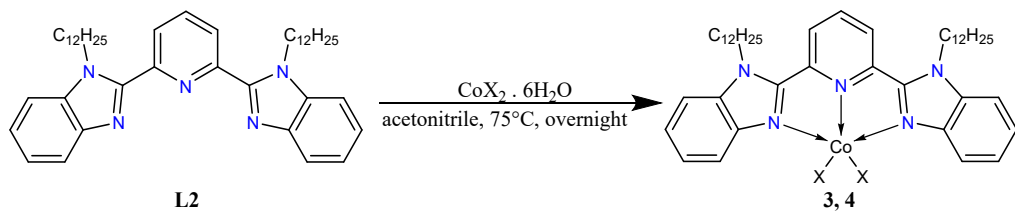


Figure S4 Scheme of synthesis of complexes 3 (X = Cl) and 4 (X = Br).

Diffraction experiments

Data collection and cell refinement for **1**, **2** and **4** were carried out using a Stoe StadiVari diffractometer with Xenocs Genix3D Cu HF and Dectris Pilatus3R 300K detector at 100K. The intensity data for **2** at 200K were collected with a Rigaku SuperNova diffractometer with AtlasS2 detector. The intensity data for **3** collected with a Rigaku XtalLAB diffractometer with an AFC11 goniometer, equipped with a Saturn 724+ HG detector and MicroMax-007HF DW microfocused rotating anode source at 120 K. The structures were solved using program Sir11² or ShelXT,³ and refined by a full-matrix least-squares procedure with the ShelXL (ver. 2018/3)⁴ integrated in Olex2 package.⁵

Magnetic measurements

Herein reported magnetic investigation have been carried out on MPMS XL-7 SQUID or MPMS 3 magnetometer (Quantum design Inc., San Diego, CA, USA). The gelatine capsules were used as sample holders and their small diamagnetic contribution is negligible in the overall magnetization, which was dominated by the sample. The exact amount of sample under the study was mixed with melted eicosane and filled into the gelatine capsule, which has been used as the sample holder. In the case of magnetic experiments at static magnetic field (DC), the temperature-dependency was recorded in the thermal range 1.9 – 300 K at $B = 0.1$ T using the 1 K/min sweeping rate, and field-dependency was measured at isothermal conditions in the range $B = 0 - 7$ T. Collected data were corrected for the diamagnetism of eicosane, gelatine capsule as well as for the molecular diamagnetic contribution calculated using the Pascal constants⁶ and transformed into the χT vs T and M_{mol} vs B dependencies. The experimental details about the magnetic experiments at AC magnetic field are given in the S4 section (*vide infra*).

Computational details

The fitting of the magnetic susceptibility and magnetization of all compounds was performed with the program PHI 3.1.3⁷. Calculations of magnetic parameters were carried out within the program ORCA 4.2.0.⁸ The ZFS parameters and crystal-field terms energies were obtained using the state averaged complete active space self-consistent field method⁹ (SA-CAS[7,5]SCF) complemented by strongly-contracted N-electron valence perturbation theory of second-order (NEVPT2).¹⁰ In either case 10 spin quartet states and 40 spin doublet reference states were taken into account. The second order Douglass-Kroll-Hess correction (DKH2)¹¹ and the resolution of identity approximation for Coulomb and exchange integrals (RI-JK)^{12,13} were set on. For all atoms the relativistically re-contracted Ahlrichs' basis DKH-def2-TZVP¹⁴ was used with an automatically generated auxiliary basis set.¹⁵ Prior to this calculation, the positions of all hydrogen atoms were optimized on the model fragments using the method PBEh-3c¹⁶ and all other atoms were kept in their positions as obtained from the X-ray analysis. The ZFS parameters were calculated by quasi-degenerate perturbation theory (QDPT),^{17,18} in which an

approximation to the Breit-Pauli form of the spin-orbit coupling operator (SOMF approximation)¹⁸ and the effective Hamiltonian theory were utilized.¹⁹ In all calculations the increased integration grid was used (level 5 in ORCA convention).

EPR spectroscopy

The spectra of electron paramagnetic resonance (EPR) were studied using Bruker ELEXSYS II E500 X-band spectrometer with an operating frequency of 9.4 GHz equipped with ESR910 helium flow-type cryostat. The measurements were performed in the temperature range from 2 K up to 40 K. Nascent polycrystalline samples were embedded in eicosane wax as used for magnetization measurements and attached to the Suprasil sample holder.

Far Infrared Magnetic Spectroscopy

The magneto-optical response of the studied compound has been also explored in the THz/infrared range, using the standard Faraday configuration (i.e. in transmission mode, with the magnetic field parallel to the wave vector of the probing radiation). To ensure the transparency in this spectral range, the compounds were mixed with eicosane in the indicated ratio, and subsequently pressed into pellets. To measure magneto-transmission, the radiation of a globar, or alternatively, of a mercury lamp, has been analyzed by the Vertex 80v Fourier-transform spectrometer, and using light-pipe optics, delivered to the pellet placed inside a superconducting coil and kept in the helium heat-exchange gas at T=4.2K. After passing through the pellet, the radiation was detected using a composite bolometer placed just below.

Lithography and surface characterization

Drop casting: Thin deposits were prepared by drop casting, depositing 20 $\mu\text{l}/\text{cm}^2$ of 10 g/L or saturated solution in chloroform (Aldrich, chromatography grade), on 1 x 1 cm^2 Si wafer covered by native oxide. Substrates were cleaned by sonication in acetone for 10 min, then in 2-propanol for 10 min, and dry in a stream of nitrogen and heated at 100 °C for 15 min. All the operations were performed in air under laminar flow hood at room temperature.

Lithographically Controlled Wetting: Elastomeric polydimethylsiloxane (PDMS, Sylgard 184 Dow Corning) molds were prepared by replica molding of Compact Disk supports or silicon masters. The stamp motifs consist of parallel protruding lines (220 nm thick, 700 nm width and 1.5 μm periodicity). After curing for 6 h at 60 °C, PDMS stamps were peeled off, cleaned by sonication in ethanol for 10 min, and dried under nitrogen flow. 5 μL of solution of compound **3** dissolved in chloroform at room temperature were drop cast on the silicon substrate, then a PDMS stamp was placed on the top and the solvent was allowed to evaporate for 24 h. Afterwards, the stamp was removed and, before characterization, the samples were aged for 2 hours. A detailed description of LCW was reported previously.²⁰

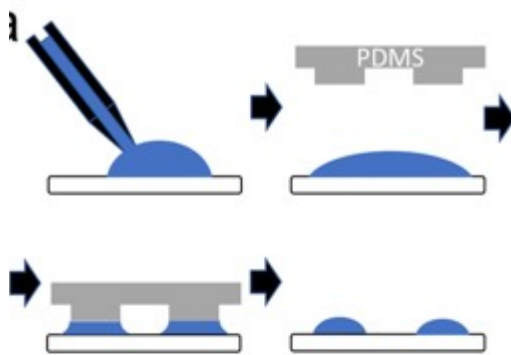


Figure S5 Scheme of lithographically controlled wetting.

Optical Microscopy: Optical images were recorded by a Nikon i-80 optical microscope equipped with an epi-illuminator and crossed polarizers.

Atomic Force Microscopy: AFM images were recorded by a Bruker Multimode VIII (Bruker Nano Surface) and operated in the Peakforce Mode. The probes used were standard ScanAsyst cantilever (Bruker AFM Probes) with a nominal spring constant of 0.4 N/m and a nominal curvature radius of 2 nm. Images were collected at 1 Hz, then processed using the open-source software Gwyddion.

Thermal sublimation

We used a home-built high-vacuum sublimation chamber equipped with a quartz crucible heated by silicon nitride heater (BACH RC GmbH, Seefeld, Germany) with a thermocouple in thermal contact with the crucible. The base chamber pressure during the sublimation was 1×10^{-6} mbar. The compounds started to sublime in the range from 350 - 370 °C.

X-ray photoelectron spectroscopy (XPS)

X-ray photoelectron (XPS) measurements were carried out with a Kratos Axis Supra (Kratos Analytical, Manchester, United Kingdom) spectrometer at room temperature and under ultra-high vacuum (UHV) conditions. The instrument was equipped with a monochromatic Al K α source of 1486.6 eV (15 mA, 15 kV) and a hemispherical analyzer with a hybrid magnetic and electrostatic lens for enhanced electron collection. Survey and detailed XPS spectra were acquired at normal emission with fixed pass energies of 160 and 20 eV, respectively. All spectra were calibrated to the hydrocarbon peak set to 284.8 eV. The Kratos charge neutralizer system was used on all specimens. The inelastic backgrounds in all the spectra were subtracted according to the Shirley method²¹. Data analysis was based on a standard deconvolution method using a mixed Gaussian (G) and Lorentzian (L) line shape (G = 70% and L = 30%, Gaussian–Lorentzian product) for each component in the spectra. The spectra were analyzed using the CasaXPS software (version 2.3.18).

S2 Spectral characterization of prepared compounds

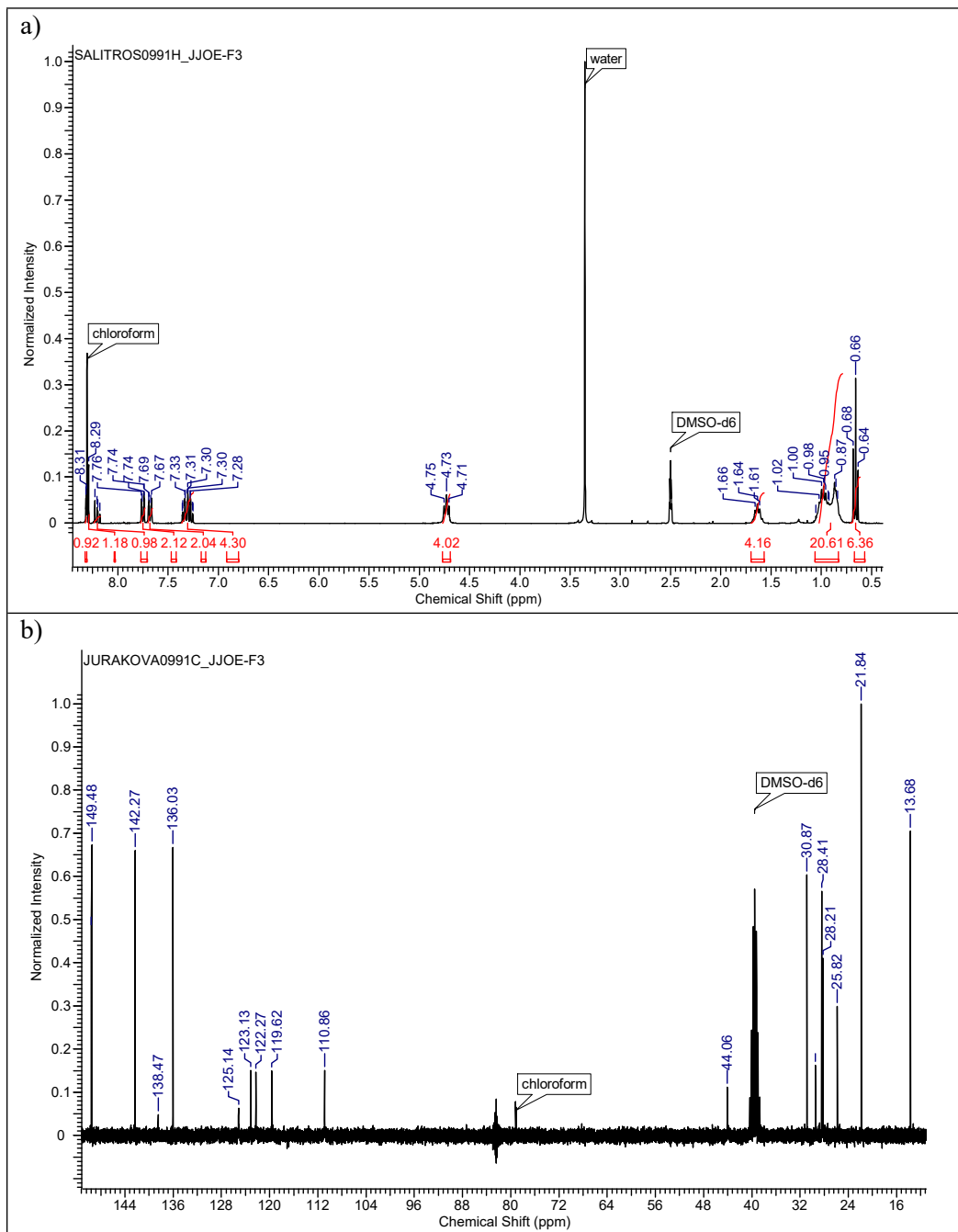


Figure S6 ^1H NMR (a) and ^{13}C NMR (b) spectra of L1.

a)

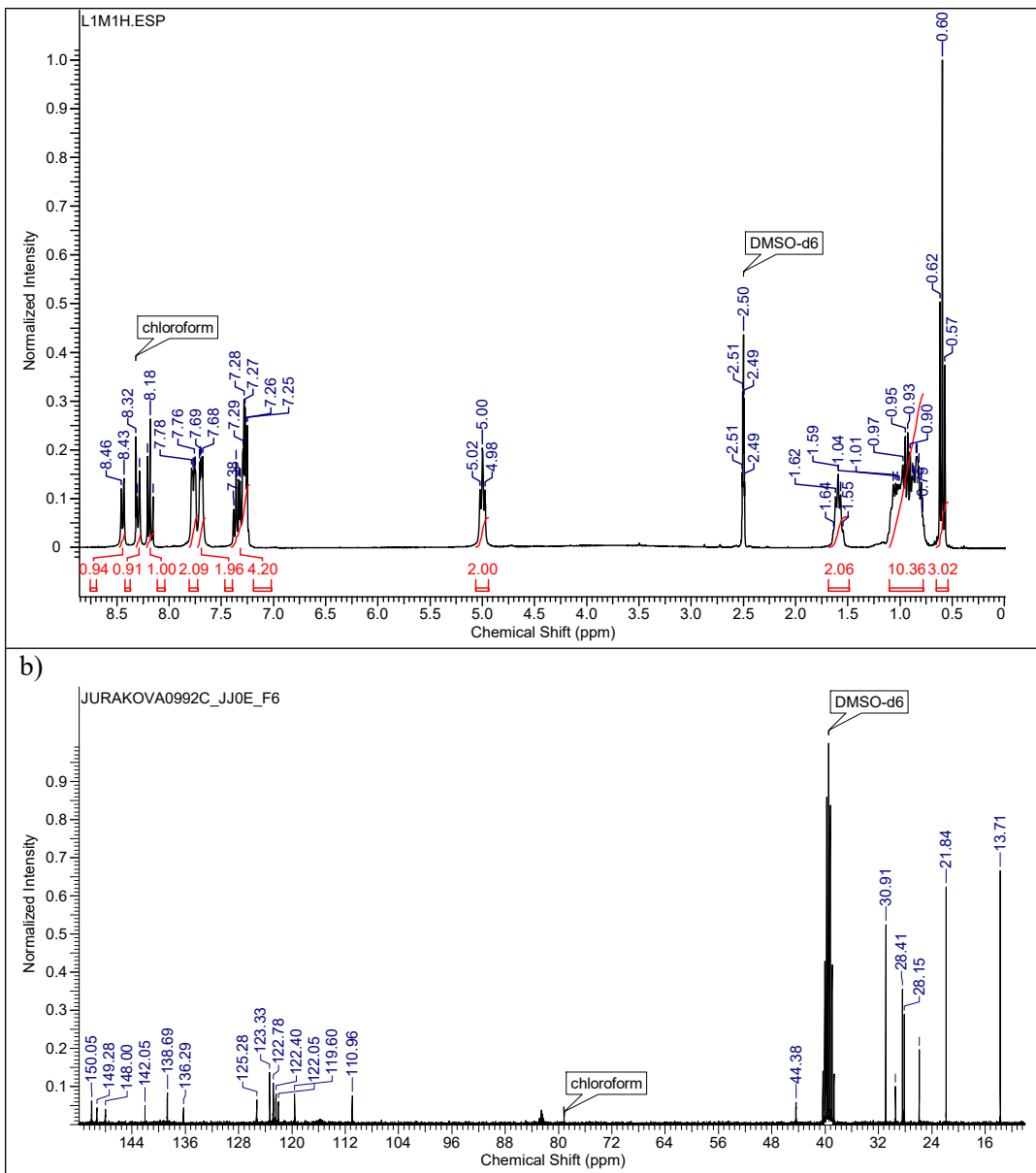


Figure S7 ^1H NMR (*a*) and ^{13}C NMR (*b*) spectra of L1_m .

a)

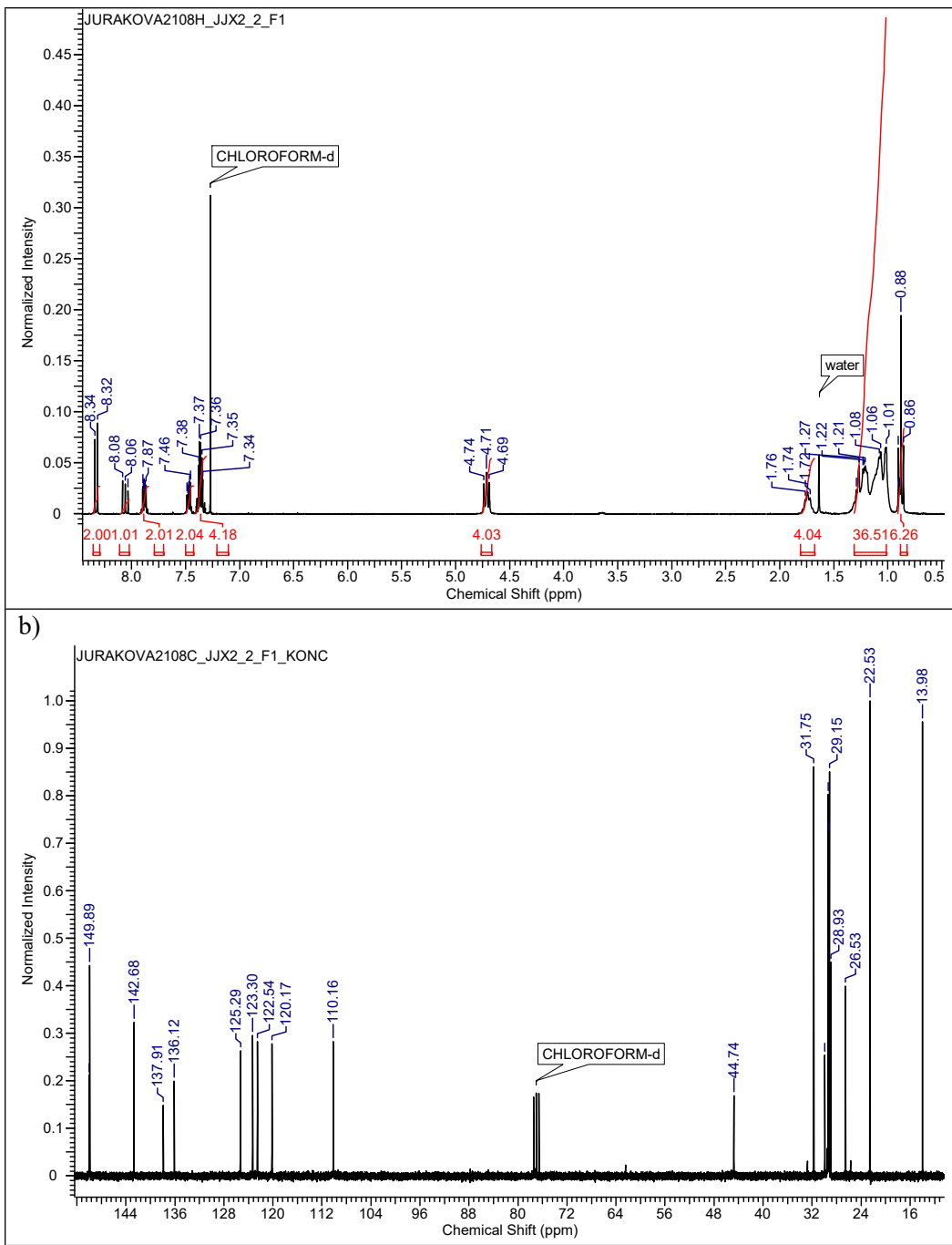


Figure S8 ^1H NMR (*a*) and ^{13}C NMR (*b*) spectra of L2.

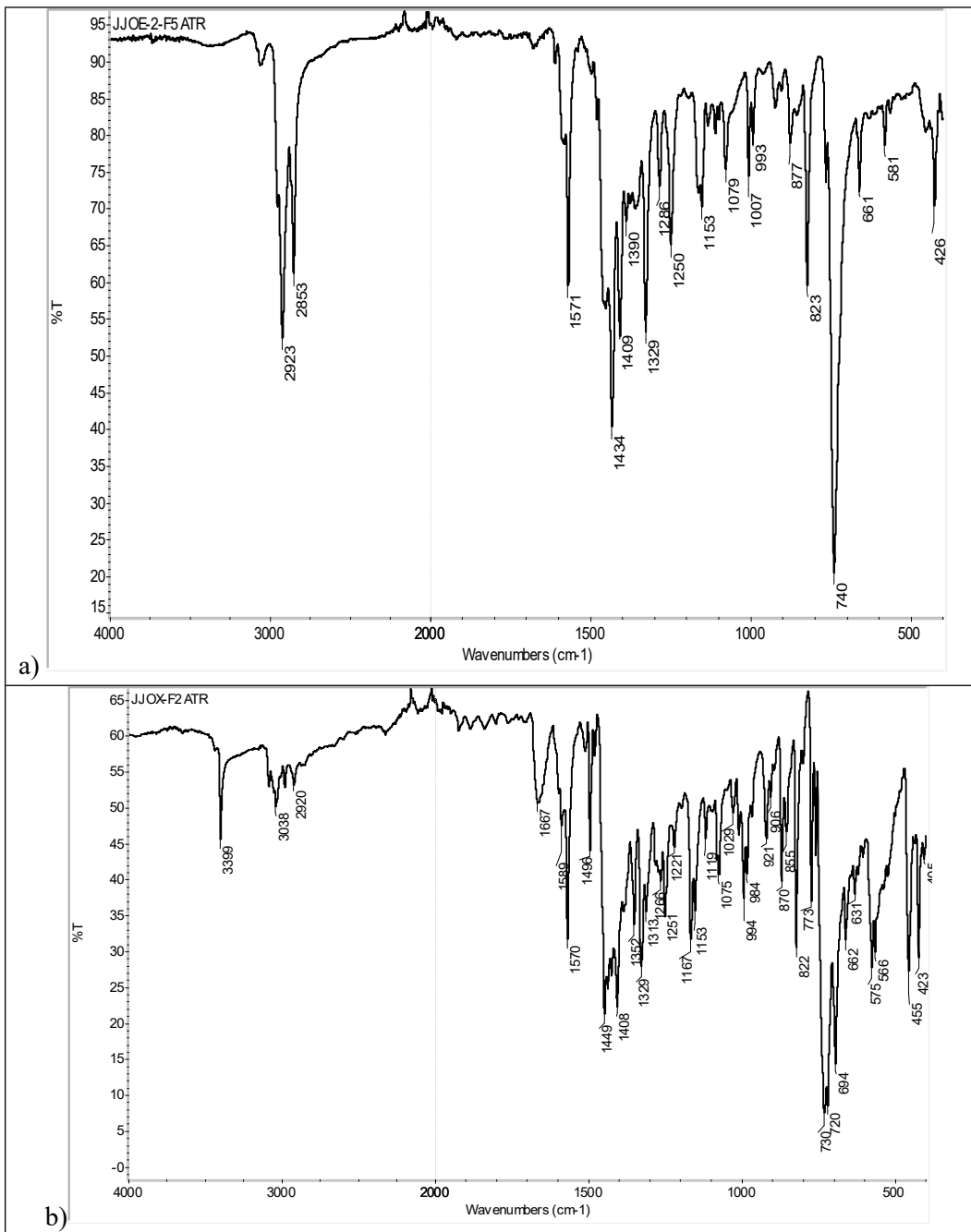


Figure S9 FT-IR spectra of L1 (*a*) and L1_m (*b*).

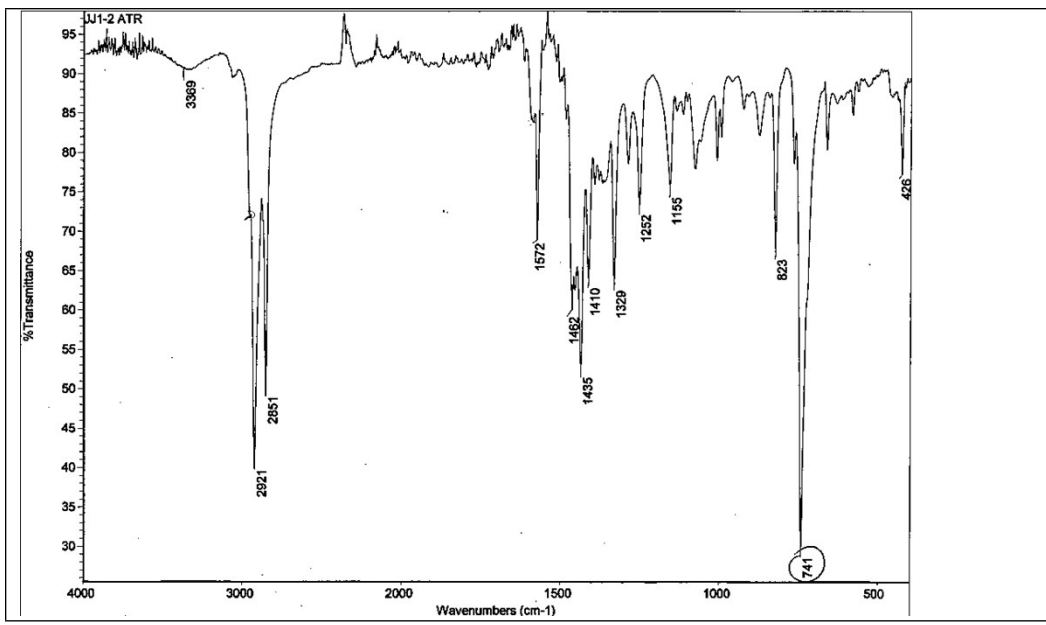


Figure S10 FT-IR spectra of L2.

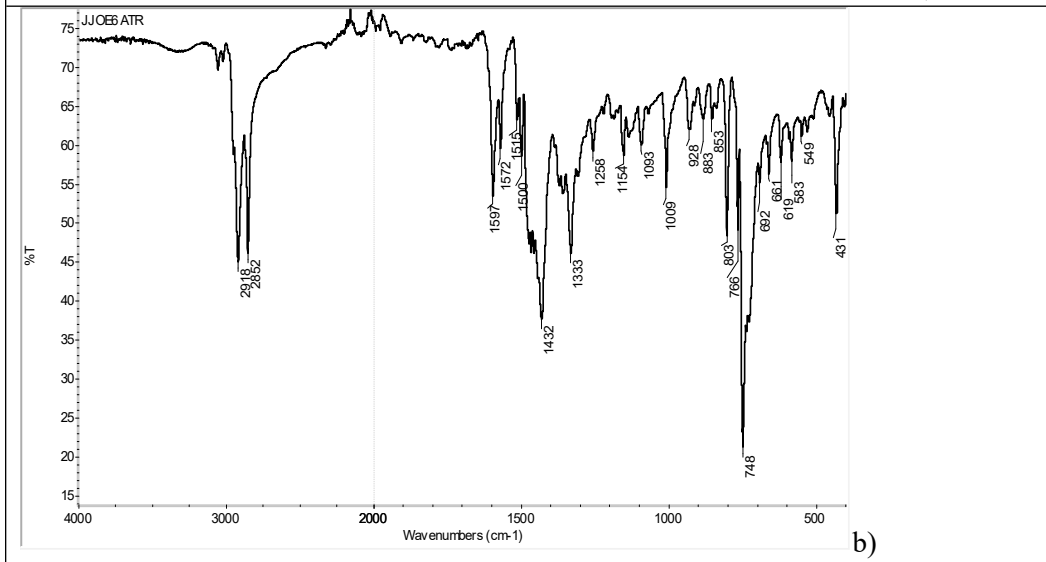
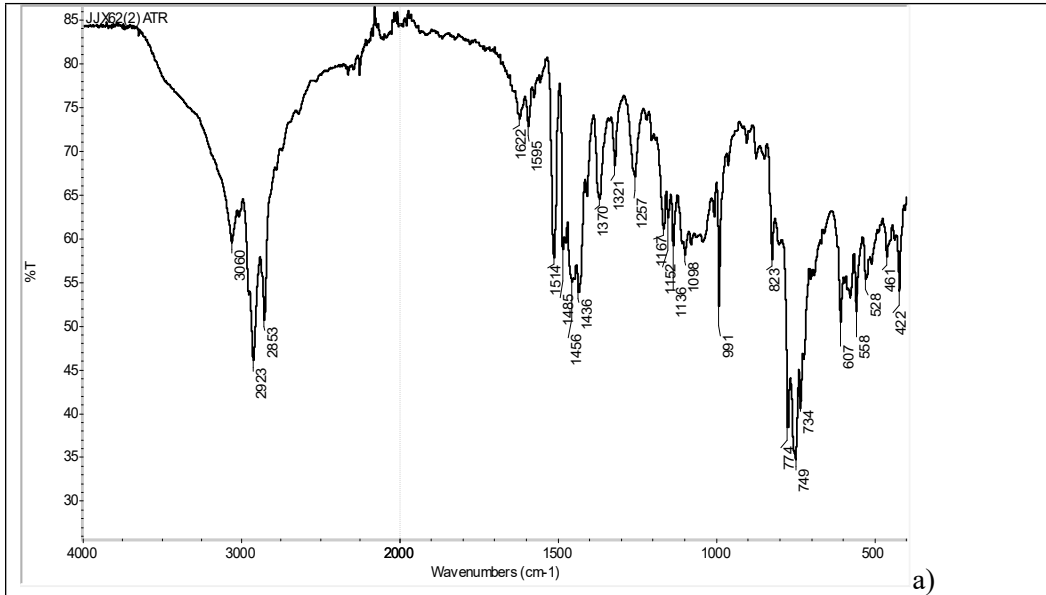


Figure S11 FT-IR spectra of 1 (a) and 2 (b).

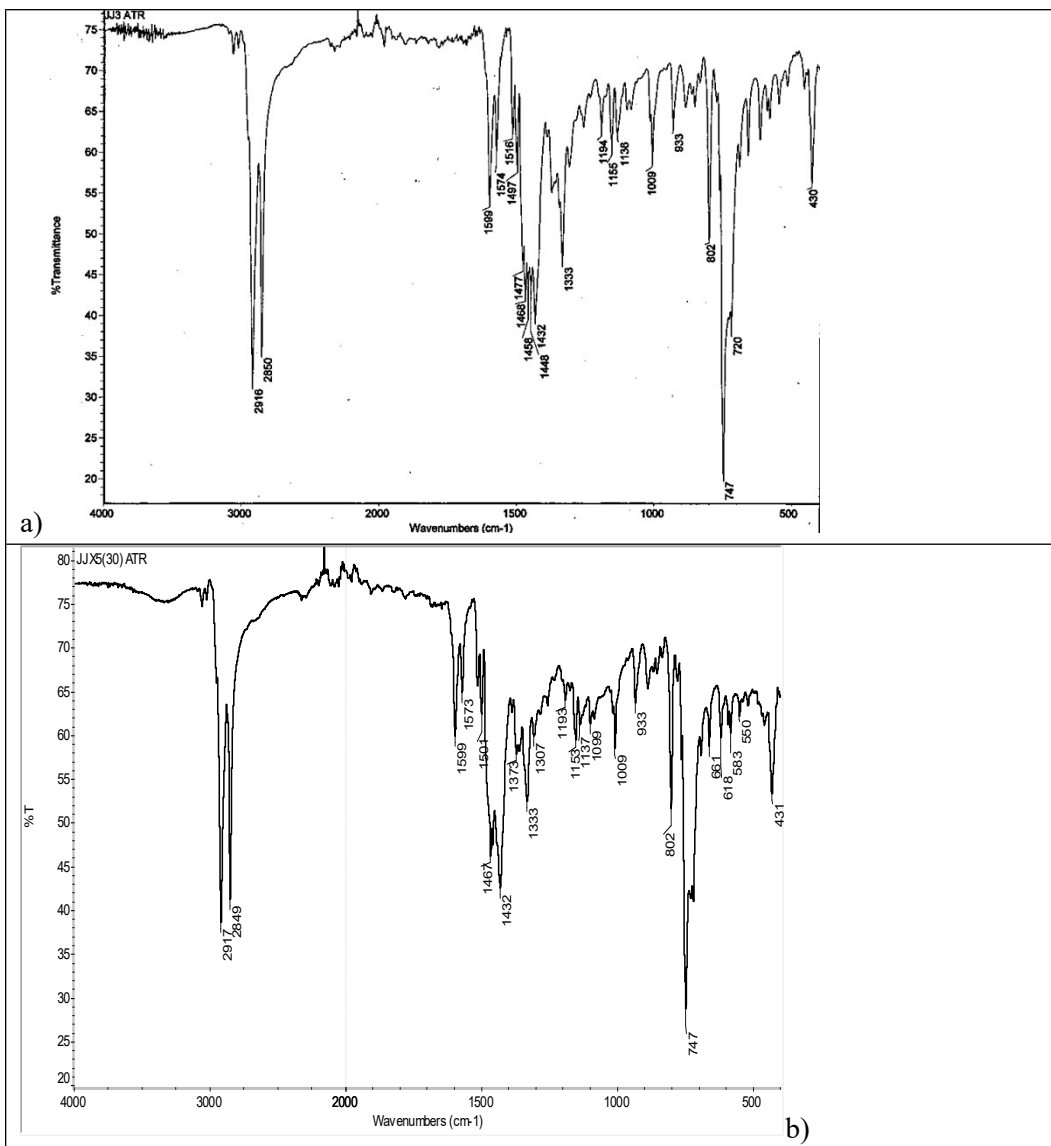


Figure S12 FT-IR spectra of 3 (a) and 4 (b).

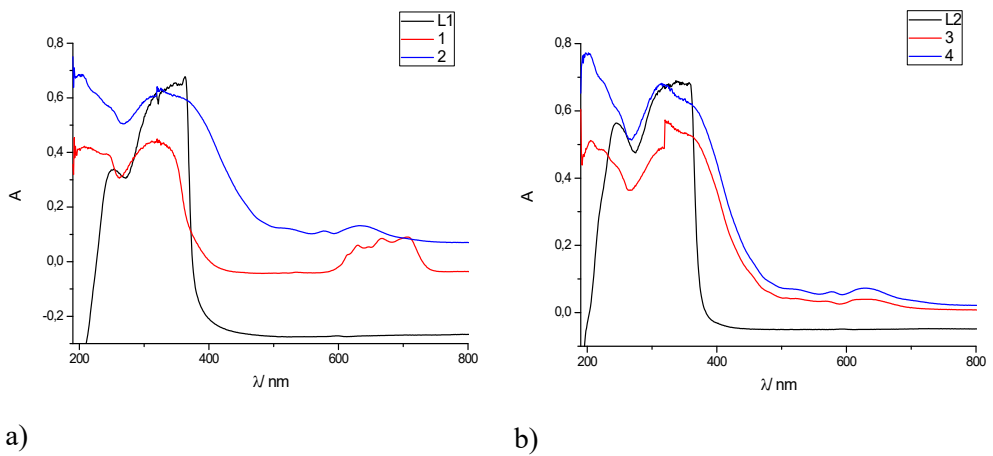


Figure S13 UV-VIS spectra of L1, 1, 2 (a) and L2, 3, 4 (b) measured in the nujol suspension.

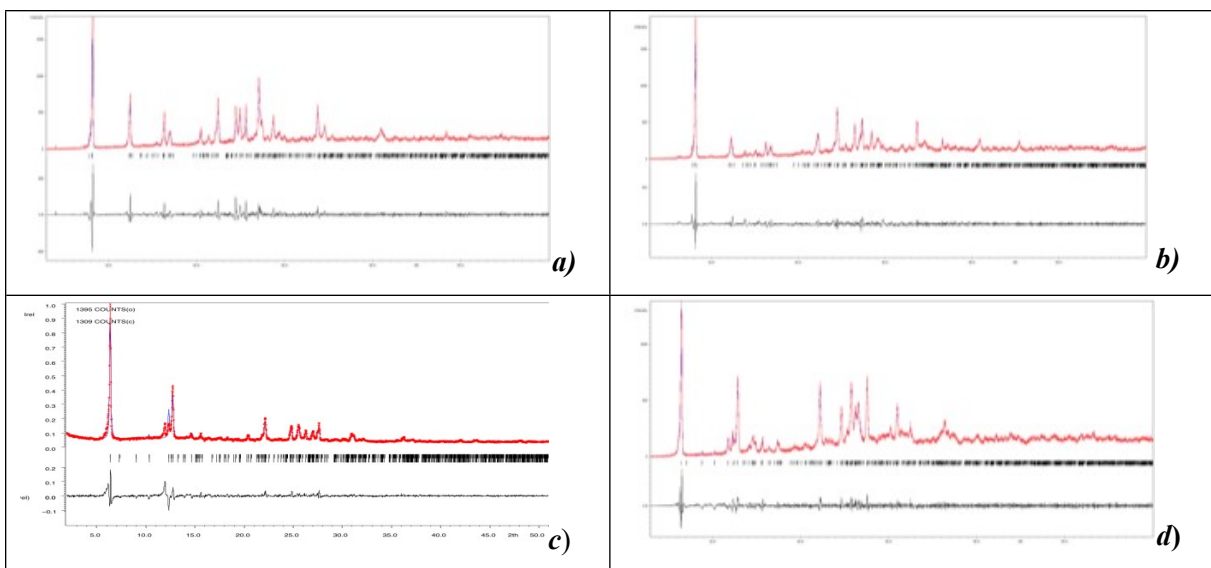


Figure S14 X-ray powder diffractograms of **1** (**a**), **2HT** (**b**), **3** (**c**) and **4** (**d**). The red and blue lines present experimental and simulated diffractions, respectively. The black lines present subtracted differences between the measured and simulated spectra.

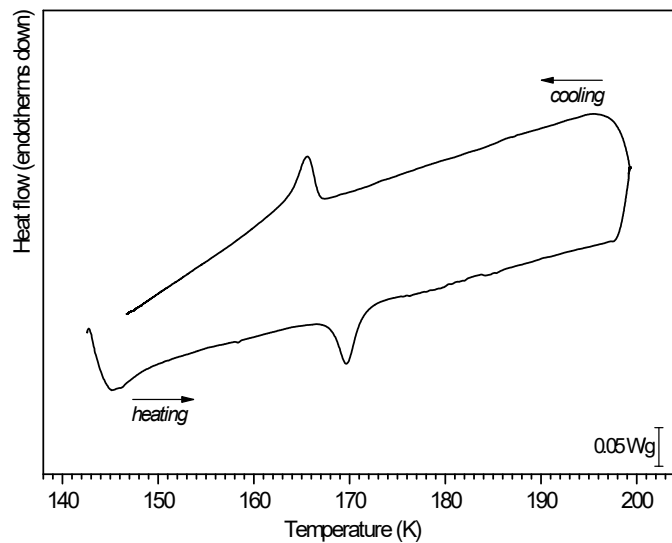


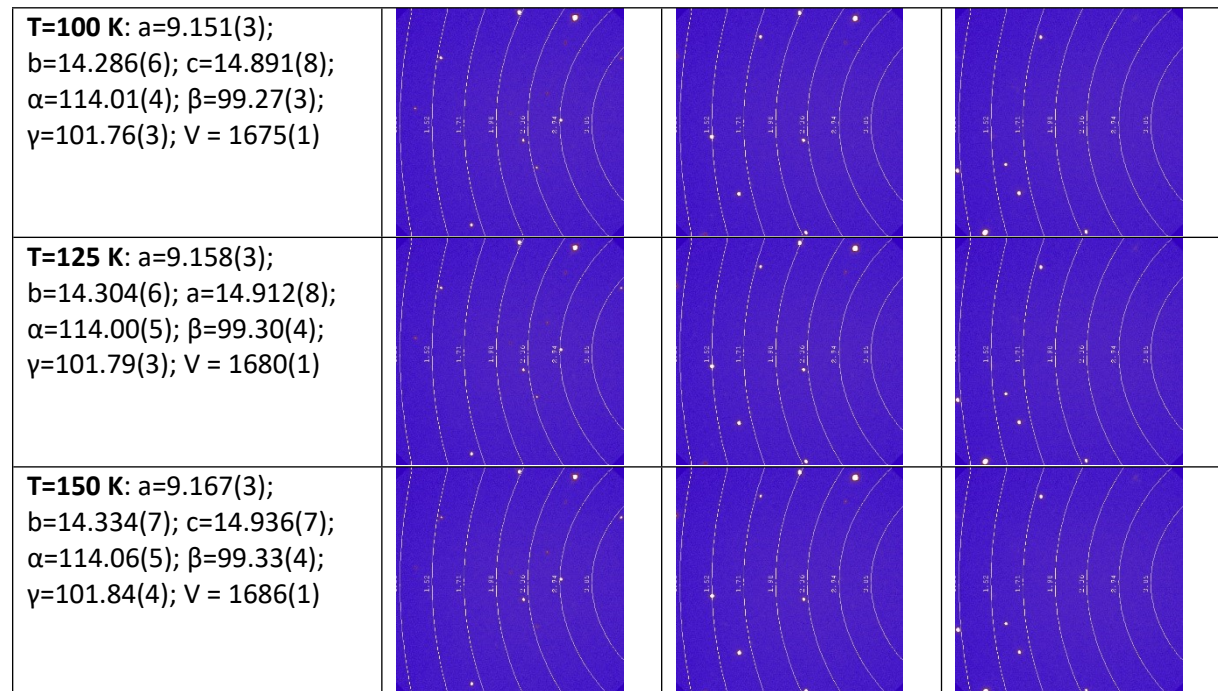
Figure S15 DSC thermogram for compound **2**. The crystallographic phase transition is taking place at 166.9 K on cooling and 167.8 K on heating.

S3 Structural information

Table S1 Selected crystallographic information for reported complexes **1-4**.

	1	2LT	2HT	3	4
Formula	$\text{CoN}_5\text{C}_{35}\text{H}_{45}\text{Cl}_2$		$\text{CoN}_5\text{C}_{35}\text{H}_{45}\text{Br}_2$	$\text{CoN}_5\text{C}_{43}\text{H}_{61}\text{Cl}_2$	$\text{CoN}_5\text{C}_{43}\text{H}_{61}\text{Br}_2$
$M_w / \text{g mol}^{-1}$	665.59		754.51	777.79	866.71
T / K	100(1)	100(1)	200(1)	120(1)	100(1)
$\lambda / \text{\AA}$	1.54186		1.54186	0.71073	1.54186
Crystal system	triclinic		triclinic	triclinic	triclinic
Space group	<i>P</i> -1		<i>P</i> -1	<i>P</i> -1	<i>P</i> -1
a/Å	8.8019(2)	9.1563(2)	9.0194(1)	8.7609(6)	8.8827(3)
b/Å	14.2971(3)	14.2913(2)	14.5433(1)	14.5870(10)	14.7126(5)
c/Å	15.0944(4)	14.9077(3)	15.0595(1)	16.6456(12)	16.4876(6)
$\alpha/^\circ$	114.993(2)	114.1250(10)	113.130(1)	95.622(2)	95.394(3)
$\beta/^\circ$	97.681(2)	99.1010(10)	99.658(1)	101.075(2)	100.857(3)
$\gamma/^\circ$	101.592(2)	101.8280(10)	102.824(1)	99.327(2)	100.080(3)
Volume/Å ³	1634.62(7)	1677.42(6)	1698.17(3)	2041.63	2065.45(13)
Z; $\rho_{\text{calc}}/\text{g}\cdot\text{cm}^{-3}$	2; 1.352	2; 1.494	2; 1.476	2; 1.265	2; 1.394
μ/mm^{-1}	5.863	7.039	6.953	0.587	5.788
F(000)	702	774	774	830	902
Final Rindices	$R_1 = 0.0366$, $[I > 2\sigma(I)]^a$ $wR_2 = 0.0920$	$R_1 = 0.0248$, $wR_2 = 0.0649$	$R_1 = 0.0263$, $wR_2 = 0.0719$	$R_1 = 0.0274$, $wR_2 = 0.0753$	$R_1 = 0.0382$, $wR_2 = 0.0951$
R indices (all data) ^a	$R_1 = 0.0393$, $wR_2 = 0.0958$	$R_1 = 0.0262$, $wR_2 = 0.0658$	$R_1 = 0.0269$, $wR_2 = 0.0723$	$R_1 = 0.0278$, $wR_2 = 0.0756$	$R_1 = 0.0500$, $wR_2 = 0.1025$
GoF on F^2	1.049	1.038	1.048	1.063	1.045
CCDC no.	2025270	2025271	2025272	2025273	2025274

$$^a R1 = \sum (F_0 - F_C) / \sum (F_0); wR2 = \sqrt{\sum [w(F_0^2 - F_C^2)] / \sum [w(F_0^2)]}$$



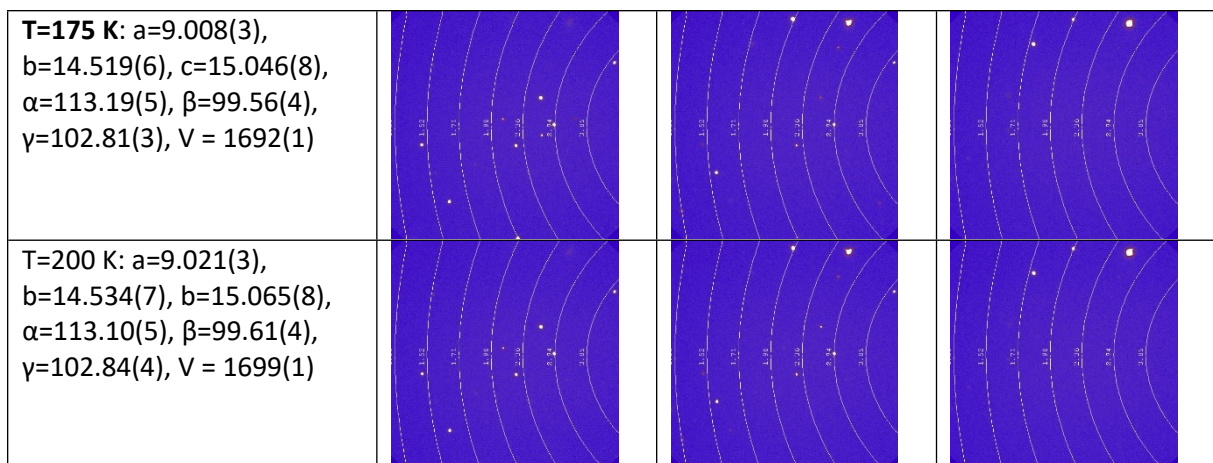


Figure S16 Temperature dependent diffraction experiments for compound **2**.

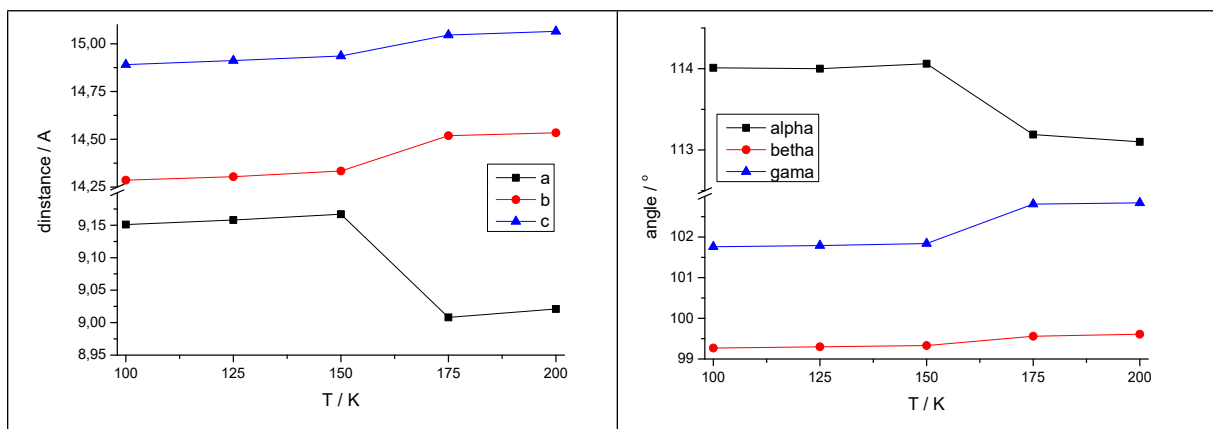


Figure S17 Thermal evolution of unit cell parameters in compound **2**.

Table S2 Bond distances and miscellaneous structural parameters of coordination polyhedra calculated for the reported compounds **1-4**.

	1 [Co(L1)Cl ₂] @ 100K	2 [Co(L1)Br ₂] LT@100K HT@ 200K	3 [Co(L1)Cl ₂] @ 120K	4 [Co(L2)Br ₂] @ 100K
Co-N1 / Å	2.1438(16)	2.1115(16)	2.129(2)	2.1469(11)
Co-N3 / Å	2.0926(16)	2.1372(15)	2.110(2)	2.1000(11)
Co-N4 / Å	2.1201(16)	2.1102(16)	2.111(2)	2.1213(11)
Co-X1 / Å	2.2911(5)	2.4498(3)	2.4580(3)	2.2996(4)
Co-X2 / Å	2.3112(5)	2.4674(4)	2.4387(4)	2.3239(4)
d(Co···{N1,N3, N4,X} basal plane) / Å	0.553(3)	0.467(3)	0.537(6)	0.544(2)
τ_5	0.18	0.13	0.08	0.12
PP ^a	32.174	31.392	32.393	31.785
vOC ^a	4.639	4.078	4.756	4.362
TBPY ^a	3.457	6.649	4.697	4.052
SPY ^a	2.403	2.122	2.435	2.215
JTBPY ^a	7.415	9.662	9.373	8.016

^aResults of the SHAPE calculations for coordination polyhedra **1-4**. PP (D_{3h}) – pentagon; vOC (C_{4v}) vacant octahedron; TBPY (D_{3h}) trigonal bipyramidal; SPY (C_{4v}) spherical square pyramid; JTBPY (D_{3h}) Johnson trigonal bipyramidal.

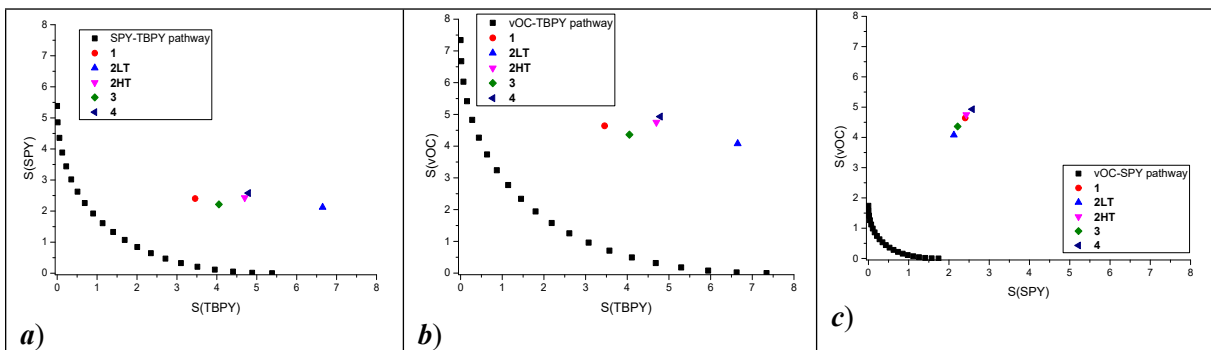
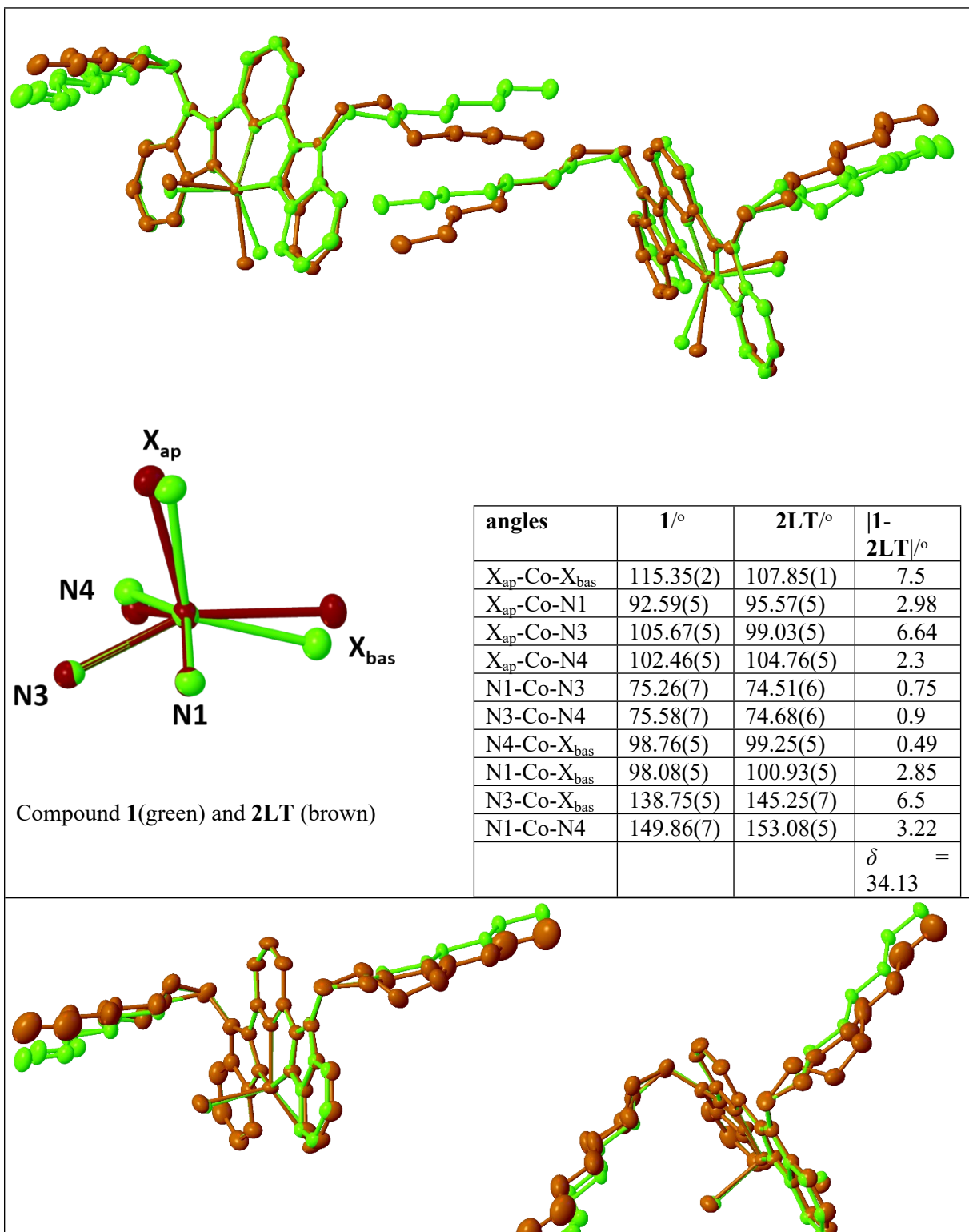
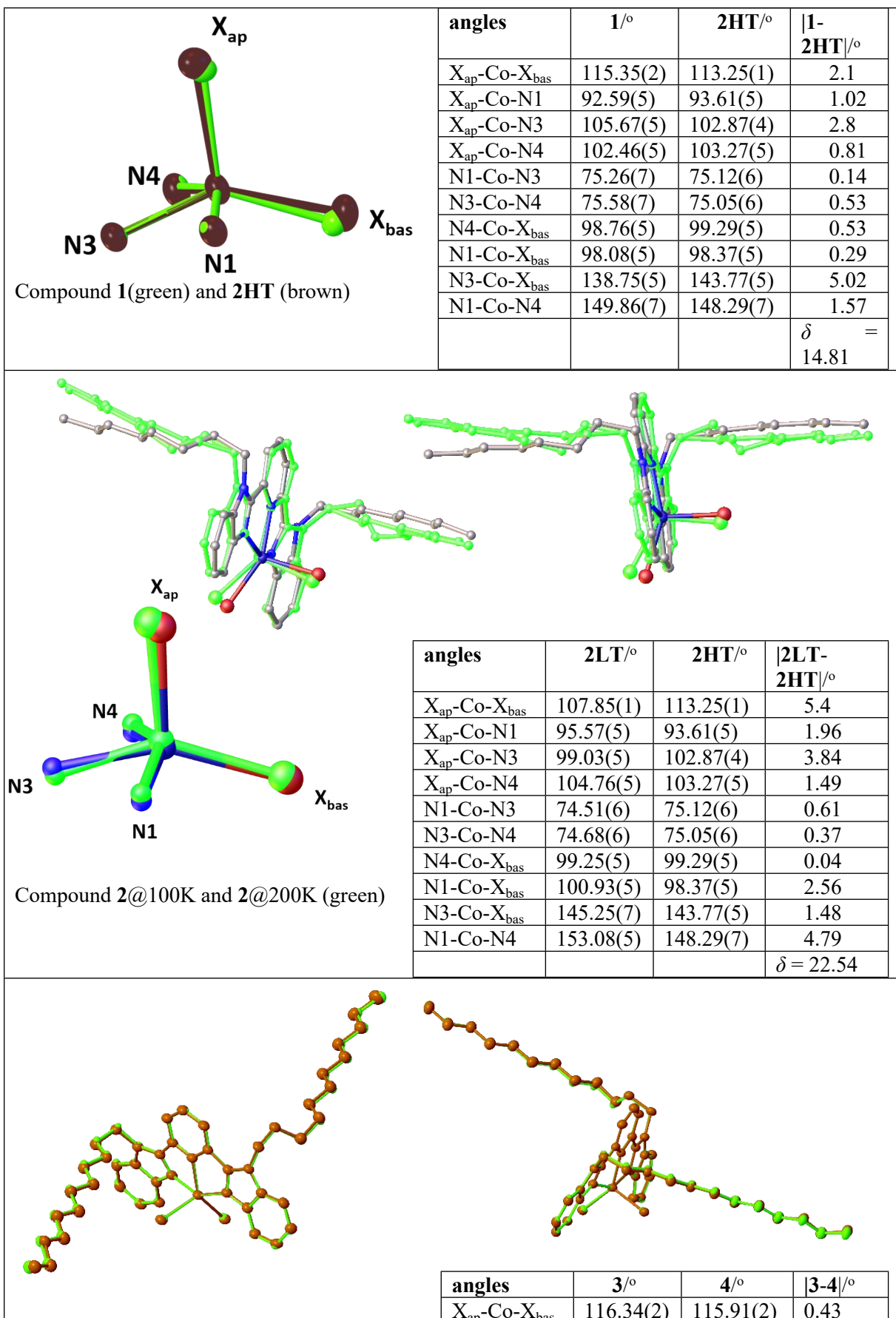


Figure S18 Symmetry measure parameters of reported structures obtained by SHAPE structural analysis and their positions on the continuous shape maps of **a)** SPY-TBPY (Berry) distortion, **b)** vOC-TBPY and **c)** vOC-SPY distortion pathways.

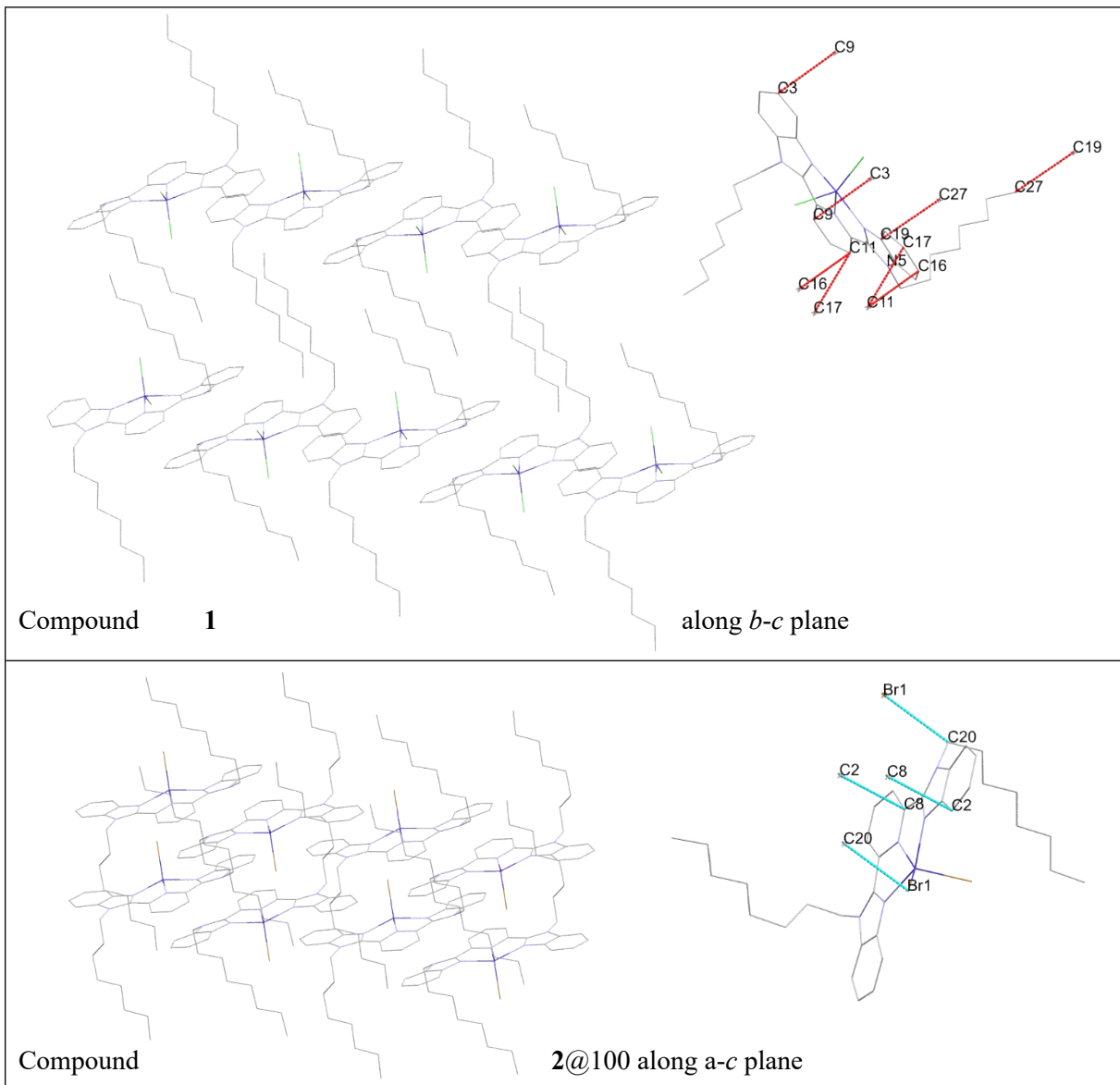




X _{ap} -Co-N1	91.56(3)	91.40(8)	0.16
X _{ap} -Co-N3	101.81(3)	100.49(8)	1.32
X _{ap} -Co-N4	104.29(3)	105.01(8)	0.72
N1-Co-N3	74.97(5)	75.0(1)	0.03
N3-Co-N4	75.59(5)	75.6(1)	0.01
N4-Co-X _{bas}	97.05(3)	96.87(8)	0.18
N1-Co-X _{bas}	99.65(3)	99.86(8)	0.21
N3-Co-X _{bas}	141.70(4)	143.46(8)	1.76
N1-Co-N4	148.83(5)	148.5(1)	0.33
			$\delta = 5.15$

Compound 3 and 4 (brown)

Figure S19 The spatial differences of the molecular structures and coordination polyhedra of reported compounds. Inserted tables compare 10 angles of coordination polyhedra and their absolute values of differences and sum of absolute differences (parameter δ). The isomorphous couples **1-2HT** and **3-4** have the smallest sum of differences. The further δ parameters for couples **1-3**, **2LT-4** and **2HT-4** are 15.27° , 25.17° and 14.09° , respectively. X_{ap} , X_{bas} are corresponding halogenido (Cl^- or Br^-) donor atoms located in the apex and in the basal plane of tetragonal pyramid, respectively.



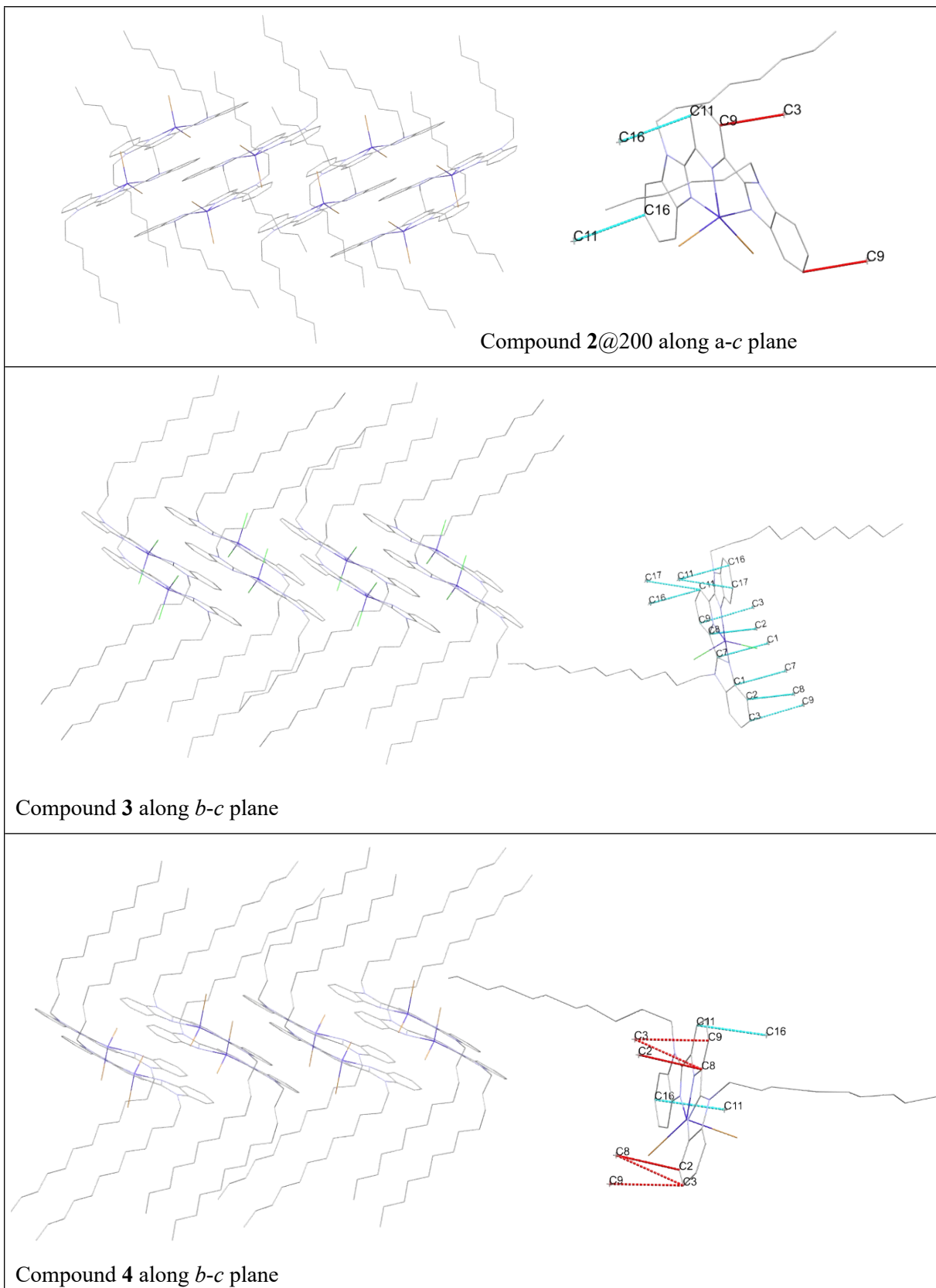


Figure S20 Supramolecular arrangement of **1-4**. Compound **1 (a)**: $C_3 \cdots C_9 = 3.341(2) \text{ \AA}$, $C_{11} \cdots C_{16} = 3.273(2) \text{ \AA}$; $C_{11} \cdots C_{17} = 3.375(3) \text{ \AA}$; $C_{19} \cdots C_{27} = 3.366(3) \text{ \AA}$, $N_5 \cdots C_{19} = 3.489(2) \text{ \AA}$; $d(\text{Co}\cdots\text{Co})_{\text{dimer}} = 7.4093(5) \text{ \AA}$, $d(\text{Co}\cdots\text{Co})_{\text{outofdimer}} = 8.5149(5) \text{ \AA}$. Compound **2LT (b)**: $C_2 \cdots C_8 = 3.325(2) \text{ \AA}$, $\text{Br}_1 \cdots C_{20} = 3.540(2) \text{ \AA}$, $d(\text{Co}\cdots\text{Co})_{\text{dimer}} = 6.7203(5) \text{ \AA}$, $d(\text{Co}\cdots\text{Co})_{\text{outofdimer}} = 8.9442(5) \text{ \AA}$. Compound **2HT (c)**: $C_3 \cdots C_9 = 3.399(3) \text{ \AA}$, $C_{11} \cdots C_{16} = 3.349(3) \text{ \AA}$, $d(\text{Co}\cdots\text{Co})_{\text{dimer}} = 7.1831(4) \text{ \AA}$, $d(\text{Co}\cdots\text{Co})_{\text{outofdimer}} = 8.7091(5) \text{ \AA}$. Compound **3 (d)**: $C_9 \cdots C_3 = 3.364(2) \text{ \AA}$; $C_8 \cdots C_2 = 3.391(2) \text{ \AA}$; $C_7 \cdots C_1 = 3.378(2) \text{ \AA}$; $d(\text{Co}\cdots\text{Co})_{\text{dimer}} = 7.1194(6) \text{ \AA}$,

$d(\text{Co}\cdots\text{Co})_{\text{outofdimer}}=8.3818(6)$ Å. Compound 4 (*e*): C8···C2=3.397(4) Å; C8···C3=3.396(4) Å; C9···C3=3.366(5) Å; C11···C16=3.331(5) Å; C16···C11=3.331(5) Å; $d(\text{Co}\cdots\text{Co})_{\text{dimer}}=7.1064(8)$ Å, $d(\text{Co}\cdots\text{Co})_{\text{outofdimer}}=8.5049(9)$ Å.

S4 Computational Study and Static Magnetic Properties

The change of orbital ordering due to geometry distortion was tested on the same model system as in the previous seminal work²². Namely, the complex cation $[\text{Co}(\text{NH}_3)_5]^{2+}$ was fixed in vOC geometry and in SPY geometry, in either case all Co-N bond lengths were fixed at 1.86 Å and in the latter case the Co atom was elevated from the basal plane by 0.5 Å. The CAS[7,5]SCF-NEVPT2/AILFT was used according to the same settings which were used for **I-IV** (see Computational Details for more information). The resulting orbital ordering is shown in Figure S21 concluding with qualitatively the same result as was provided by a less accurate DFT method.²²

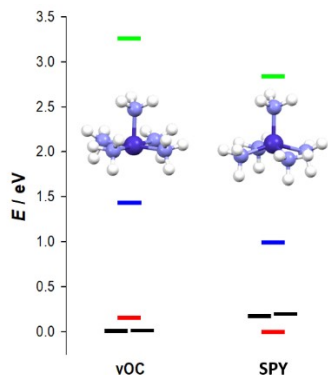


Figure S21 Energy of CASSCF-NEVPT2/AILFT orbitals for $[\text{Co}(\text{NH}_3)_5]^{2+}$ in the case of vOC geometry (*left*) and SPY geometry (*right*). black: e orbitals, red: b_2 orbitals, blue: a_1 orbitals, green: b_1 orbitals.

For every model molecule a state-averaged CAS[7,5]SCF calculation was performed, that is, an optimal set of five molecular d -like orbitals (called complete active space, CAS) was sought, which can best describe all possible spin doublet and spin quartet states arising from seven electrons in these d -like orbitals (CAS roots). As a next step, the energy of every CAS root was corrected for interaction between seven electrons from within CAS and all other electrons in molecule using the method NEVPT2. Finally, ab-initio Ligand-Field Theory²³²³ (AILFT) was employed, by which energy of all states is projected upon the effective ligand-field Hamiltonian. One-electron eigenstates of AILFT Hamiltonian resemble then the textbook atomic d -orbitals and their corresponding eigenvalues can be interpreted as information on the splitting of d -orbitals due to the crystal-field. Resulting AILFT d -orbitals with assigned symmetry labels of group C_4v are displayed in Figure S22 and their energy ordering is displayed in Figure 2a (in the main text).

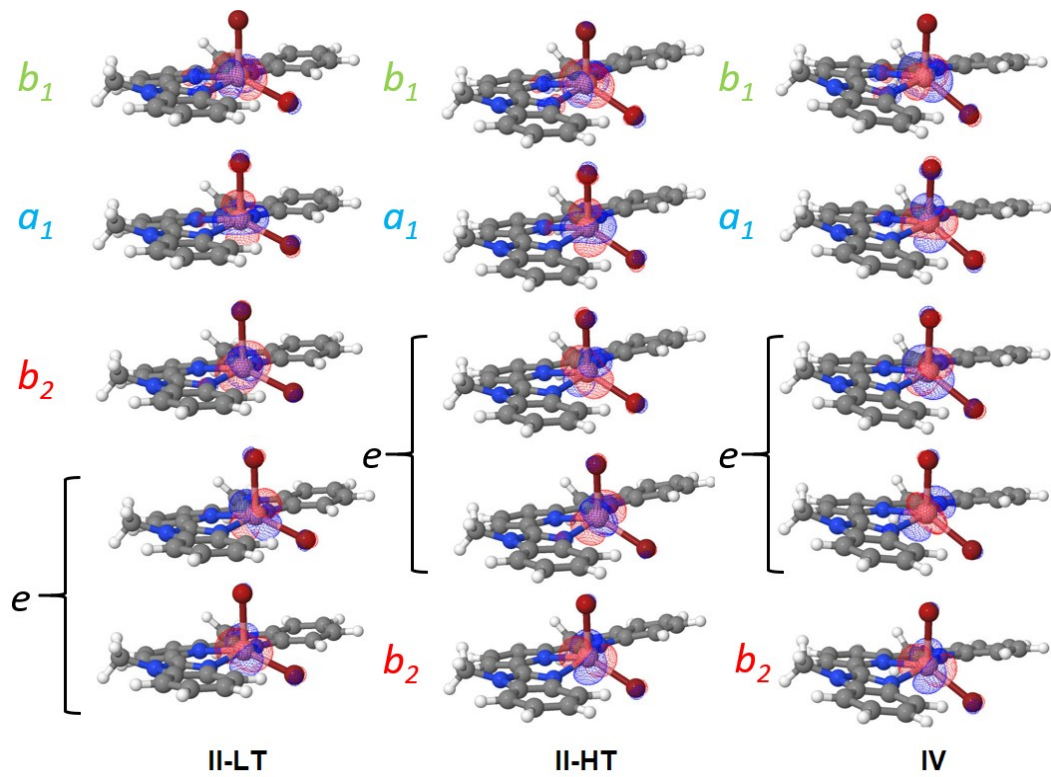


Figure S22 AILFT orbitals for **II-LT** (left), **II-HT** (middle) and **IV** (right) with assigned symmetry labels within the C_{4v} group.

In Table S3 the composition of six lowest quartet CAS roots is displayed with respect to CAS configurations. In every case the weighted average configuration is calculated, and the best fitting integer-number configuration(s) is deduced. For example, the average occupancy of the first orbital in ground state of **I** (labelled as state “0” by ORCA convention) is obtained as $0.84819 \times 2 + 0.13163 \times 1 + 0.00985 \times 1 + 0.00374 \times 2 + 0.00293 \times 1 = 1.84873$. Indicated crystal field terms are derived according to Ref. 24 based on the symmetry labels of AILFT orbitals. For example the electronic configuration $e^2b_2^2a_1^1b_1^2$ gives three possible representations of crystal-field symmetry since $e \otimes e \otimes b_2 \otimes b_2 \otimes a_1 \otimes b_1 \otimes b_1 = a_2 \oplus a_1 \oplus e$. However, only a_2 is consistent with the spin quartet state, therefore the resulting CFT term was identified as 4A_2 . Straightforward application of the CFT assignment technique predicts orbital degeneracy for most of higher-lying CFTs (i.e. E terms), which however does not appear to be the case when looking at considerable energetic gaps between the higher lying CAS roots (pink color in Figure 2b). Such discrepancy can be attributed to non-ideal geometry of the coordination environment of model molecules. Indeed, by symmetry transition from C_{4v} to D_{3h} in pentacoordinate Co(II) systems, the induced splitting of degenerate terms is expected to be more pronounced for the excited ones.²⁵

Table S3 Composition of six lowest quartet CAS roots for molecules **I-IV** with indication of best matching quartet crystal-field term or its component.

	I	II-LT	II-HT	III	IV
0		0.74486: 22111 0.12366: 12211 0.08949: 21121 0.02197: 21211 0.00741: 21112			
0.84819: 22111			0.44096: 21211 0.37605: 12211 0.13455: 21121	0.82387: 22111 0.13491: 11221	0.42020: 12211 0.30466: 21211 0.14511: 22111
0.13163: 11221					

	0.00985: 12121 0.00374: 21211 0.00293: 12211 ----- 1.85,1.86,1.13,1.14,1.00 22111→⁴A₂	0.00735: 12121 0.00267: 11212 0.00254: 11221 ----- 1.86,1.88,1.15,1.10,1.01 22111→⁴A₂	0.03917: 22111 0.00527: 21112 0.00260: 12112 ----- 1.62,1.42,1.82,1.13,1.01 21211→⁴E(a)	0.02640: 21211 0.00605: 12121 0.00444: 21121 ----- 1.85,1.83,1.16,1.14,1.00 22111→⁴A₂	0.11661: 21121 0.00657: 11221 0.00447: 21112 ----- 1.57,1.56,1.73,1.12,1.00 12211+21211→⁴E(a)
1	0.79097: 12211 0.10939: 12121 0.05257: 21211 0.04022: 21121 0.00458: 12112 ----- 1.09,1.90,1.84,1.14,1.00 12211→⁴E(a)	0.77499: 21211 0.15718: 12121 0.05202: 12211 0.01054: 11221 ----- 1.77,1.20,1.83,1.16,1.00 21211→⁴E(a)	0.77239: 22111 0.15367: 11221 0.06758: 21211 ----- 1.83,1.77,1.21,1.15,1.00 22111→⁴A₂	0.88485: 12211 0.06580: 12121 0.03694: 21121 0.00386: 12112 0.00330: 21211 0.00312: 22111 ----- 1.04,1.96,1.89,1.10,1.00 12211→⁴E(a)	0.62634: 22111 0.22041: 21211 0.13614: 11221 0.01337: 12211 ----- 1.84,1.64,1.37,1.13,1.00 22111→⁴A₂
2	0.55249: 21211 0.20764: 12121 0.10162: 12211 0.05801: 21112 0.04544: 21121 0.02024: 11221 0.01073: 12112 0.00338: 22111 ----- 1.66,1.32,1.67,1.27,1.06 21211→⁴E(b)	0.43570: 12211 0.25698: 21121 0.16892: 22111 0.05552: 11212 0.03518: 11221 0.01791: 12121 0.01637: 21112 0.01083: 21211 ----- 1.45,1.62,1.53,1.31,1.07 12211→⁴E(b)	0.35872: 21211 0.26672: 12211 0.16736: 12121 0.12066: 21121 0.05847: 12112 0.01417: 22111 0.01368: 11221 ----- 1.49,1.51,1.64,1.30,1.06 21211+12211→⁴E(b)	0.58999: 21211 0.26143: 12121 0.05736: 21112 0.03035: 12211 0.02111: 12112 0.01491: 22111 0.01468: 11221 0.00974: 21121 ----- 1.67,1.33,1.63,1.29,1.08 21211→⁴E(b)	0.34161: 21211 0.23242: 12211 0.19300: 12121 0.11211: 21121 0.05975: 12112 0.04618: 22111 0.01297: 11221 ----- 1.50,1.53,1.59,1.32,1.06 21211+12211→⁴E(b)
3	0.69070: 11221 0.13141: 12211 0.49356: 21121 0.24628: 12121 0.13992: 21211 0.06872: 12112 0.04780: 21112 0.00344: 12211 ----- 1.68,1.32,1.14,1.74,1.12 21121→⁴E(a)	0.75451: 12121 0.09381: 12211 0.03277: 11212 0.01620: 12121 0.00773: 21112 0.00763: 22111 0.00464: 21211 ----- 1.12,1.15,1.86,1.81,1.04 11221→⁴B₂	0.47459: 21121 0.30969: 12121 0.08252: 12112 0.05316: 21211 0.00601: 21112 0.00543: 11221 0.00390: 21121 ----- 1.06,1.93,1.15,1.76,1.09 12121→⁴E(a)	0.74521: 12121 0.08317: 12112 0.07254: 12211 0.05557: 21211 0.03353: 11221 0.00444: 22111 0.00360: 21112 ----- 1.62,1.37,1.12,1.79,1.09 21211→⁴E(a)	0.74521: 12121 0.08317: 12112 0.07254: 12211 0.05557: 21211 0.03353: 11221 0.00444: 22111 0.00360: 21112 ----- 1.06,1.90,1.16,1.78,1.08 12121→⁴E(a)
4	0.34297: 21112 0.23243: 21121 0.34126: 21112 0.25614: 12121 0.22239: 21121 0.10898: 12112 0.04481: 12211 0.01907: 21211 0.00442: 11221 ----- 1.58,1.41,1.07,1.48,1.45 21112+12121+21121→⁴E(b)	0.41759: 21121 0.38835: 21112 0.21195: 11212 0.09980: 11221 0.04899: 12211 0.03939: 12112 0.01410: 12121 0.00446: 22111 0.00429: 21211 ----- 1.58,1.11,1.37,1.34,1.59 21112→⁴E(a)	0.40978: 21112 0.24048: 21121 0.08574: 12112 0.06840: 12211 0.02499: 12121 0.00514: 11212 0.00475: 11221 0.00375: 21211 ----- 1.81,1.18,1.08,1.45,1.48 21121+21112→⁴E(b)	0.43379: 21121 0.40938: 21112 0.06828: 12211 0.06323: 12112 0.08691: 12112 0.03384: 12211 0.02044: 21211 ----- 1.67,1.32,1.05,1.44,1.49 21112+21121→⁴E(b)	0.43379: 21121 0.40938: 21112 0.06828: 12211 0.06323: 12112 0.08691: 12112 0.03384: 12211 0.02044: 21211 ----- 1.84,1.14,1.08,1.45,1.48 21121+21112→⁴E(b)
5	0.70325: 12112 0.20272: 12121 0.89097: 11212 0.07776: 11221 0.01298: 11122 0.00737: 12112 0.00684: 22111 -----	0.84647: 11212 0.11820: 11221 0.03328: 11212 0.03000: 21211 0.01620: 21112 0.01168: 11221 0.00259: 22111 -----	0.87215: 11212 0.10769: 11221 0.03445: 12112 0.01577: 22111 0.00691: 21112 0.00372: 11122 -----	0.81928: 11212 0.11744: 11221 0.03445: 12112 0.01577: 22111 0.00691: 21112 0.00266: 21121 -----	

	1.00,1.01,1.96,1.09,1.91 11212→⁴A₂	1.04,1.91,1.07,1.21,1.75 12112→⁴E(b)	1.02,1.02,1.96,1.12,1.86 11212→⁴A₂	1.01,1.08,1.98,1.11,1.88 11212→⁴A₂	1.02,1.05,1.93,1.12,1.86 11212→⁴A₂
--	--	---	--	--	--

The Atomic Overlap Model gives for energy of three lowest lying orbitals within C_{4v} symmetry following formulae²⁴.

$$E(xy) = a(\alpha) \cdot e_{\pi}(L)$$

$$E(xz) = E(yz) = b(\alpha) \cdot e_{\pi}(L) + e_{\pi}(X)$$

where $a(\alpha)$ and $b(\alpha)$ are functions of the elevation angle and $e_{\pi}(L)$ and $e_{\pi}(X)$ are the parameters of π -donation of the basal ligands and axial ligand, respectively. When going from **III** to **IV**, the basal ligands stay almost the same (three out of four ligands do not change their positions, nor quality). One can thus assume that the decisive role for change of orbital ordering is played by the π -donation ability of the axial ligand, quantified here by parameter $e_{\pi}(X)$. Indeed, this ligand is better π -donor in the case of **IV** (bromido ligand) agreeing thus with higher energy of double degenerate orbitals in **IV** than in **III**.

By inclusion of spin-orbit interaction (SOI) within the CASSCF-NEVPT2 wavefunction, a finer structure of energy eigenstates appears. More specifically, the splitting of CAS roots to the Kramers doublets becomes apparent and from their structure the SH parameters can be extracted (see also Table S4 in SI). Composition of Kramers doublets for **II-LT** and **II-HT** is shown in Table S4. Apparently, in **II-HT** lowest four doublets (states 0-7) are best described by following sequence of magnetic quantum numbers: $\pm 1/2, \pm 3/2, \pm 3/2, \pm 1/2$ which is a strong indication that they belong to a double degenerate spin quartet CFT.⁶ In contrast, no such pattern can be seen in **II-LT**

Table S4 Composition of six lowest states of **II-LT** (*left*) and **II-HT** (*right*) obtained at the CASSCF-NEVPT2+SOI level. The root labels refer to CASSCF eigenstates (see Table S3), most contributing roots are highlighted in red.

	Weight	Block	Root	Spin	Ms		Weight	Block	Root	Spin	Ms
STATE 0:	0.0000					STATE 0:	0.0000				
	0.060500	0	0	3/2	3/2		0.162356	0	0	3/2	3/2
	0.156249	0	0	3/2	1/2		0.092254	0	1	3/2	3/2
	0.029108	0	1	3/2	1/2		0.013073	0	2	3/2	3/2
	0.011361	0	2	3/2	1/2		0.044122	0	0	3/2	1/2
	0.319945	0	0	3/2	-1/2		0.347364	0	1	3/2	1/2
	0.062963	0	1	3/2	-1/2		0.180830	0	0	3/2	-1/2
	0.292075	0	0	3/2	-3/2		0.056781	0	1	3/2	-1/2
	0.042777	0	1	3/2	-3/2		0.068610	0	1	3/2	-3/2
	0.011043	0	2	3/2	-3/2						
STATE 1:	0.0000					STATE 1:	0.0000				
	0.292075	0	0	3/2	3/2		0.068610	0	1	3/2	3/2
	0.042777	0	1	3/2	3/2		0.180830	0	0	3/2	1/2
	0.011043	0	2	3/2	3/2		0.056781	0	1	3/2	1/2
	0.319945	0	0	3/2	1/2		0.044122	0	0	3/2	-1/2
	0.062963	0	1	3/2	1/2		0.347364	0	1	3/2	-1/2
	0.156249	0	0	3/2	-1/2		0.162356	0	0	3/2	-3/2
	0.029108	0	1	3/2	-1/2		0.092254	0	1	3/2	-3/2
	0.011361	0	2	3/2	-1/2		0.013073	0	2	3/2	-3/2
	0.060500	0	0	3/2	-3/2						
STATE 2:	106.3387					STATE 2:	212.1658				
	0.456390	0	0	3/2	3/2		0.200343	0	0	3/2	3/2
	0.012432	0	2	3/2	3/2		0.175676	0	1	3/2	3/2
	0.250258	0	0	3/2	1/2		0.013337	0	2	3/2	3/2
	0.139952	0	0	3/2	-1/2		0.073440	0	0	3/2	1/2
	0.014026	0	1	3/2	-1/2		0.037210	0	1	3/2	1/2
	0.075131	0	0	3/2	-3/2		0.123032	0	0	3/2	-1/2
	0.023158	0	1	3/2	-3/2		0.079406	0	1	3/2	-1/2

							0.029024	0	0	3/2	-3/2
							0.234123	0	1	3/2	-3/2
STATE 3:	106.3387						STATE 3:	212.1658			
	0.075131	0	0	3/2	3/2			0.029024	0	0	3/2
	0.023158	0	1	3/2	3/2			0.234123	0	1	3/2
	0.139952	0	0	3/2	1/2			0.123032	0	0	3/2
	0.014026	0	1	3/2	1/2			0.079406	0	1	3/2
	0.250258	0	0	3/2	-1/2			0.073440	0	0	3/2
	0.456390	0	0	3/2	-3/2			0.037210	0	1	3/2
	0.012432	0	2	3/2	-3/2			0.200343	0	0	3/2
								0.175676	0	1	3/2
								0.013337	0	2	3/2
STATE 4:	925.8687						STATE 4:	422.7297			
	0.011875	0	0	3/2	3/2			0.210255	0	0	3/2
	0.369031	0	1	3/2	3/2			0.055435	0	1	3/2
	0.012208	0	0	3/2	1/2			0.029107	0	2	3/2
	0.092034	0	1	3/2	1/2			0.137093	0	0	3/2
	0.018985	0	3	3/2	1/2			0.192934	0	1	3/2
	0.334513	0	1	3/2	-1/2			0.015245	0	2	3/2
	0.012670	0	0	3/2	-3/2			0.035085	0	1	3/2
	0.127508	0	1	3/2	-3/2			0.091615	0	0	3/2
								0.193368	0	1	3/2
STATE 5:	925.8687						STATE 5:	422.7297			
	0.012670	0	0	3/2	3/2			0.091615	0	0	3/2
	0.127508	0	1	3/2	3/2			0.193368	0	1	3/2
	0.334513	0	1	3/2	1/2			0.035085	0	1	3/2
	0.012208	0	0	3/2	-1/2			0.137093	0	0	3/2
	0.092034	0	1	3/2	-1/2			0.192934	0	1	3/2
	0.018985	0	3	3/2	-1/2			0.015245	0	2	3/2
	0.011875	0	0	3/2	-3/2			0.210255	0	0	3/2
	0.369031	0	1	3/2	-3/2			0.055435	0	1	3/2
								0.029107	0	2	3/2
STATE 6:	1083.0241						STATE 6:	724.4706			
	0.021942	0	0	3/2	3/2			0.077790	0	0	3/2
	0.248437	0	1	3/2	3/2			0.112371	0	1	3/2
	0.069464	0	0	3/2	1/2			0.325644	0	0	3/2
	0.127334	0	1	3/2	1/2			0.025430	0	1	3/2
	0.017084	0	0	3/2	-1/2			0.041273	0	0	3/2
	0.298471	0	1	3/2	-1/2			0.190836	0	1	3/2
	0.031063	0	0	3/2	-3/2			0.013850	0	2	3/2
	0.154277	0	1	3/2	-3/2			0.136009	0	0	3/2
								0.044882	0	1	3/2
STATE 7:	1083.0241						STATE 7:	724.4706			
	0.031063	0	0	3/2	3/2			0.136009	0	0	3/2
	0.154277	0	1	3/2	3/2			0.044882	0	1	3/2
	0.017084	0	0	3/2	1/2			0.041273	0	0	3/2
	0.298471	0	1	3/2	1/2			0.190836	0	1	3/2
	0.069464	0	0	3/2	-1/2			0.013850	0	2	3/2
	0.127334	0	1	3/2	-1/2			0.325644	0	0	3/2
	0.021942	0	0	3/2	-3/2			0.025430	0	1	3/2
	0.248437	0	1	3/2	-3/2			0.077790	0	0	3/2
								0.112371	0	1	3/2
STATE 8:	2341.2698						STATE 8:	1871.9416			
	0.172040	0	2	3/2	3/2			0.273620	0	2	3/2
	0.390316	0	2	3/2	1/2			0.376619	0	2	3/2
	0.012805	0	3	3/2	1/2			0.274079	0	2	3/2
	0.262041	0	2	3/2	-1/2			0.023512	0	2	3/2
	0.014606	0	3	3/2	-1/2						
	0.097286	0	2	3/2	-3/2						
STATE 9:	2341.2698						STATE 9:	1871.9416			
	0.097286	0	2	3/2	3/2			0.023512	0	2	3/2
	0.262041	0	2	3/2	1/2			0.274079	0	2	3/2
	0.014606	0	3	3/2	1/2			0.376619	0	2	3/2
	0.390316	0	2	3/2	-1/2			0.273620	0	2	3/2
	0.012805	0	3	3/2	-1/2						
	0.172040	0	2	3/2	-3/2						
STATE 10:	2409.7172						STATE 10:	1979.8452			
	0.012704	0	0	3/2	3/2			0.049826	0	0	3/2

0.271173	0	2	3/2	3/2		0.372604	0	2	3/2	3/2
0.202091	0	2	3/2	1/2		0.014966	0	3	3/2	3/2
0.071225	0	2	3/2	-1/2		0.029467	0	0	3/2	1/2
0.383600	0	2	3/2	-3/2		0.238685	0	2	3/2	1/2
						0.010918	0	3	3/2	1/2
						0.014999	0	0	3/2	-1/2
						0.017110	0	2	3/2	-1/2
						0.014722	0	0	3/2	-3/2
						0.217226	0	2	3/2	-3/2
STATE 11: 2409.7172					STATE 11: 1979.8452					
0.383600	0	2	3/2	3/2		0.014722	0	0	3/2	3/2
0.071225	0	2	3/2	1/2		0.217226	0	2	3/2	3/2
0.202091	0	2	3/2	-1/2		0.014999	0	0	3/2	1/2
0.012704	0	0	3/2	-3/2		0.017110	0	2	3/2	1/2
0.271173	0	2	3/2	-3/2		0.029467	0	0	3/2	-1/2

Table S5 Calculated values of *g*-factors of ground Kramers' doublets for **I-IV** and energy of first excited Kramers doublet (all obtained at the CASSCF-NEVPT2 level).

	1	2LT	2HT	3	4
g_1	1.31	1.75	1.30	0.99	1.19
g_2	1.88	3.08	1.58	1.16	1.58
g_3	7.84	7.19	8.62	8.71	8.70
$E_I (cm^{-1})$	135.6	106.3	212.2	189.9	208.3

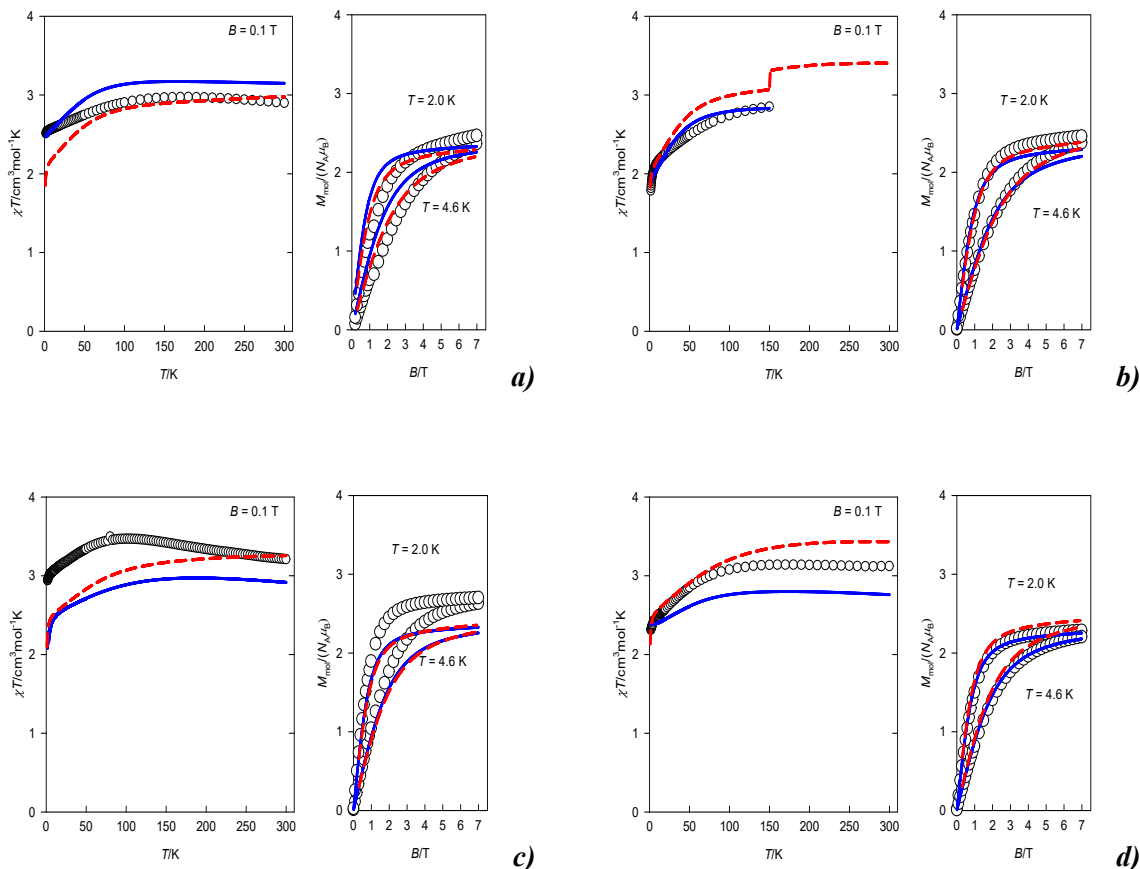
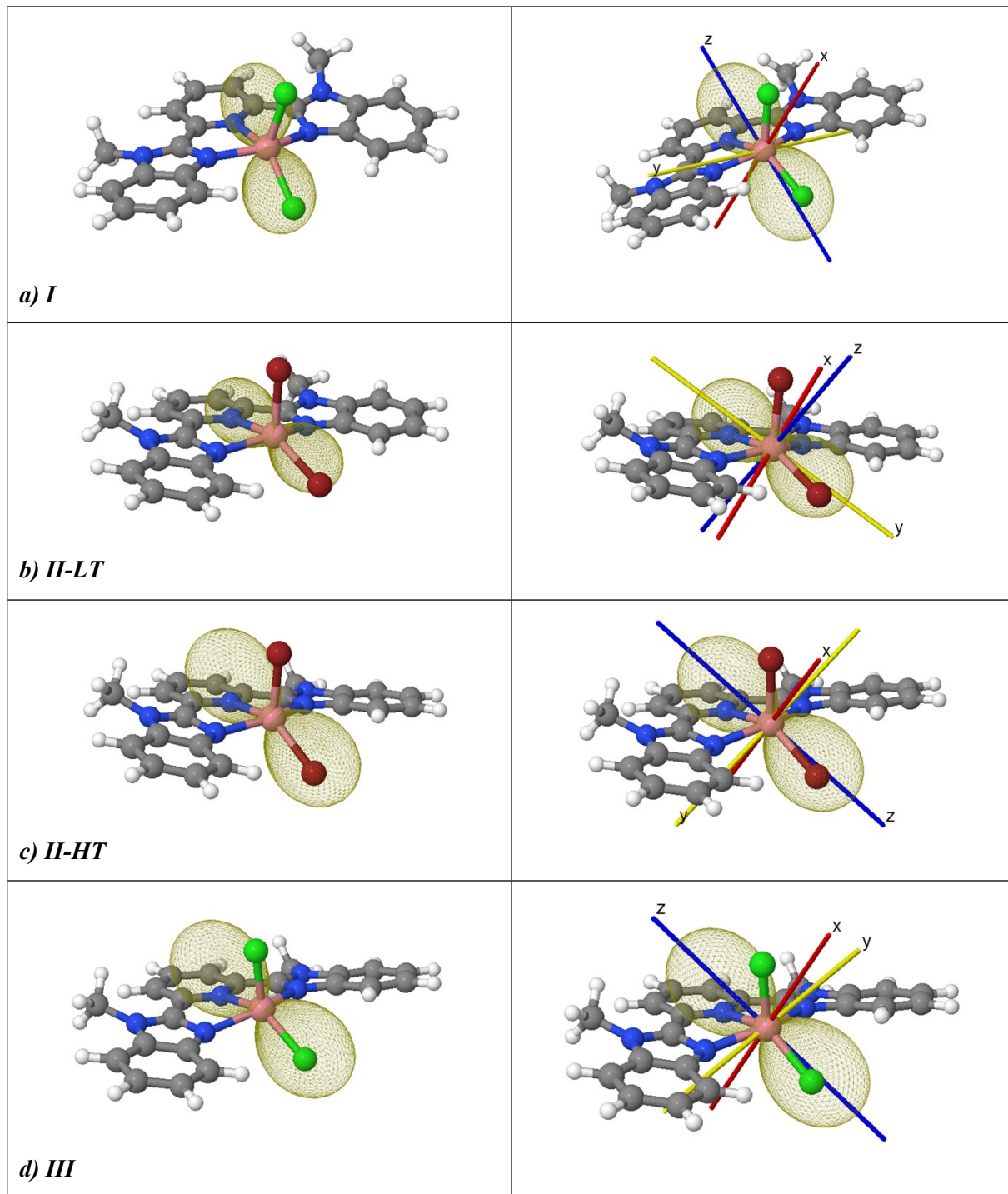


Figure S23 Magnetic functions analyzed by Griffith-Figgis Hamiltonian for compound **1** (**a**); compound **2** (**b**); compound **3** (**c**) and compound **4** (**d**). Left: susceptibility-temperature product with respect to temperature, right:

magnetization per center with respect to magnetic field; empty circles: experiment, blue solid line: optimum fit, red dashed line: *ab-initio* prediction based on model molecules.



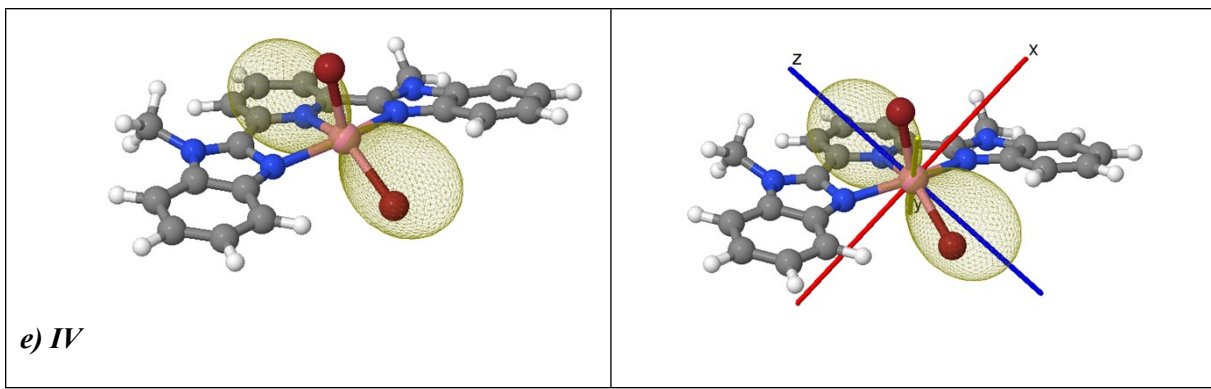


Figure S24 Comparison of orientational dependence of molecular magnetization with respect to the molecular frame for **I-IV** calculated from CASSCF-NEVPT2 wavefunction (*left*) and spin Hamiltonian (*right*). In the case of spin Hamiltonian, the main axes of *D*-tensor are displayed, too.

S5 EPR spectroscopy

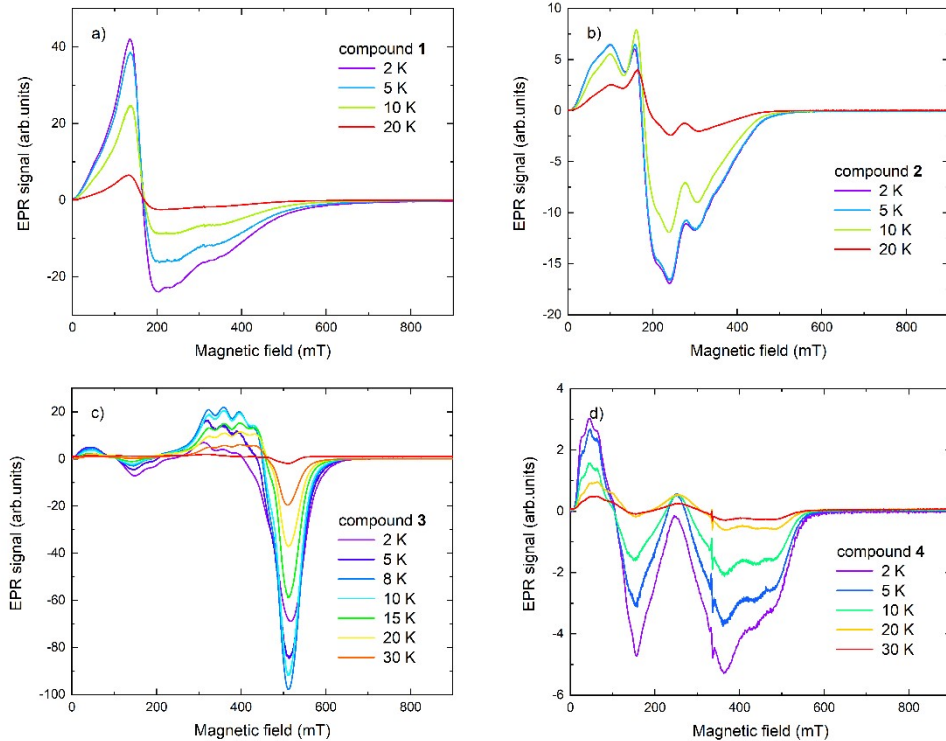


Figure S25 Temperature evolution of X-band solid state EPR spectra for **1-4**.

S6 Far IR magnetic spectroscopy

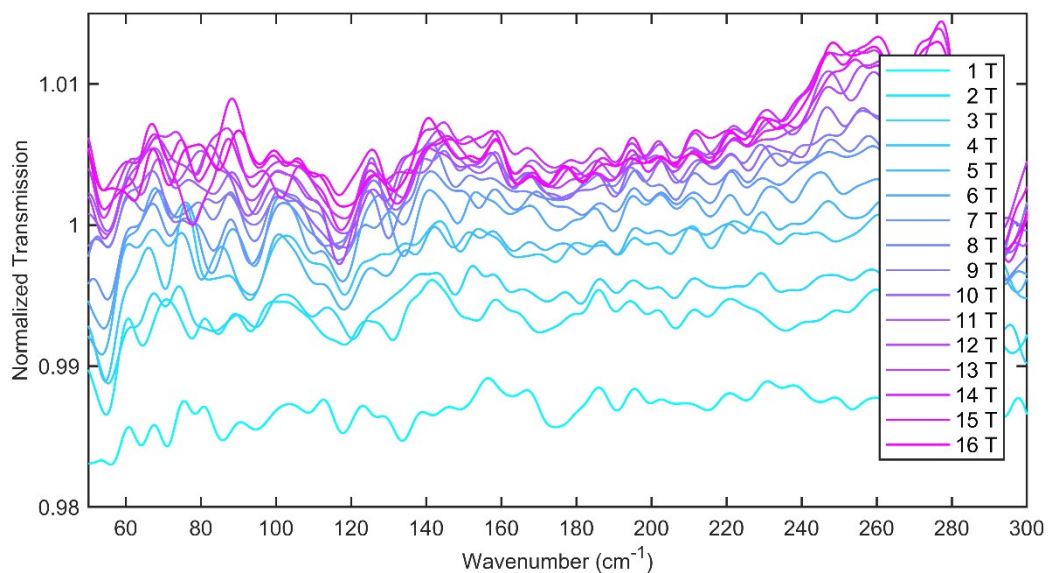


Figure S26 Normalized FIRMS transmission spectra recorded on pressed powder pellet of complex **1** at T = 4.2 K and magnetic field up to 16 T. Spectra were normalized by zero-field transmission spectra division and corresponding reference transmission spectra division.

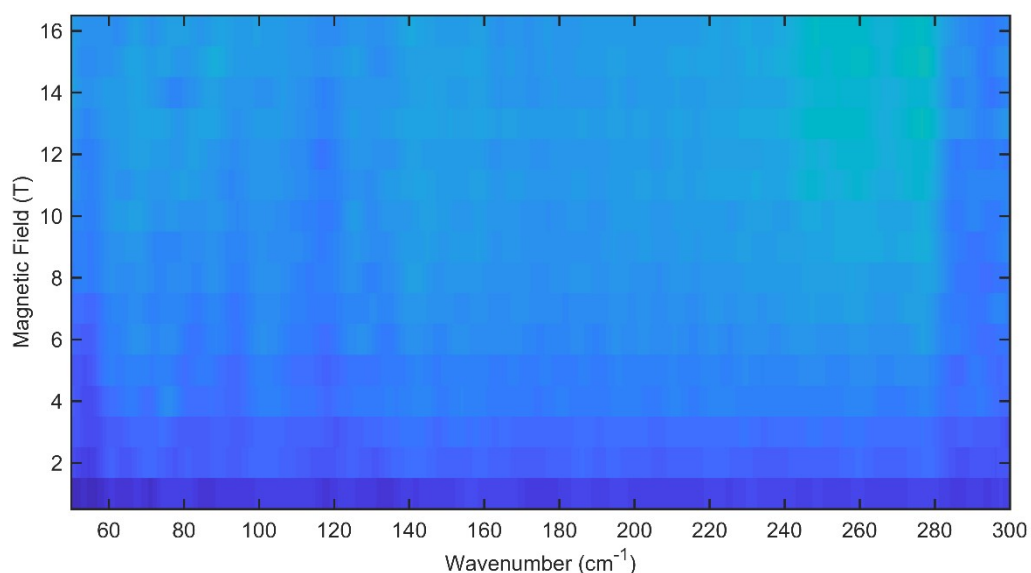


Figure S27 A color map of normalized FIRMS transmission spectra recorded on pressed powder pellet of complex **1** at T = 4.2 K and magnetic field up to 16 T. Spectra were normalized by zero-field transmission spectra division and corresponding reference transmission spectra division.

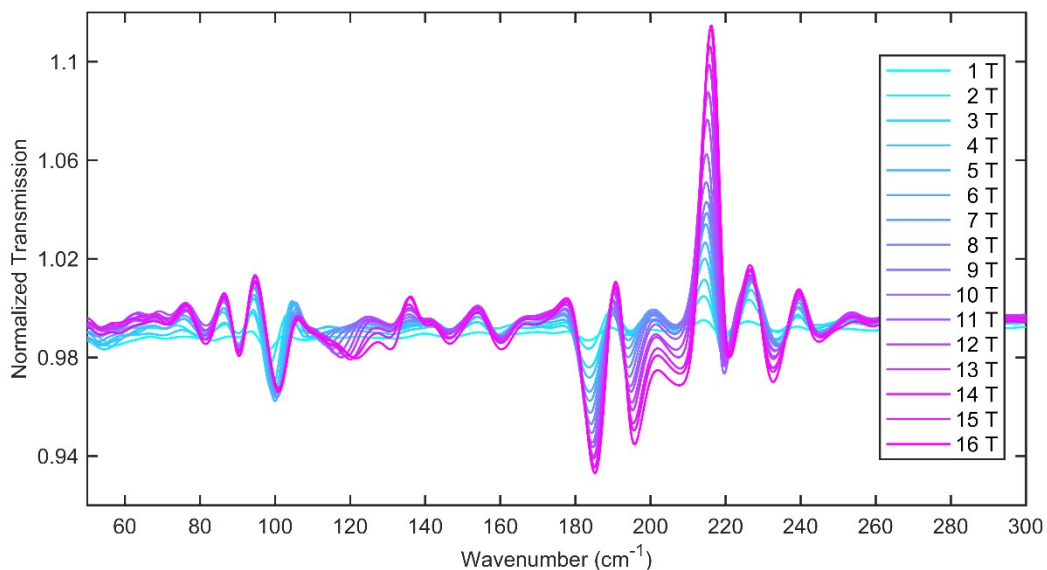


Figure S28 Normalized FIRMS transmission spectra recorded on pressed powder pellet of complex **2** at $T = 4.2\text{ K}$ and magnetic field up to 16 T . Spectra were normalized by zero-field transmission spectra division and corresponding reference transmission spectra division.

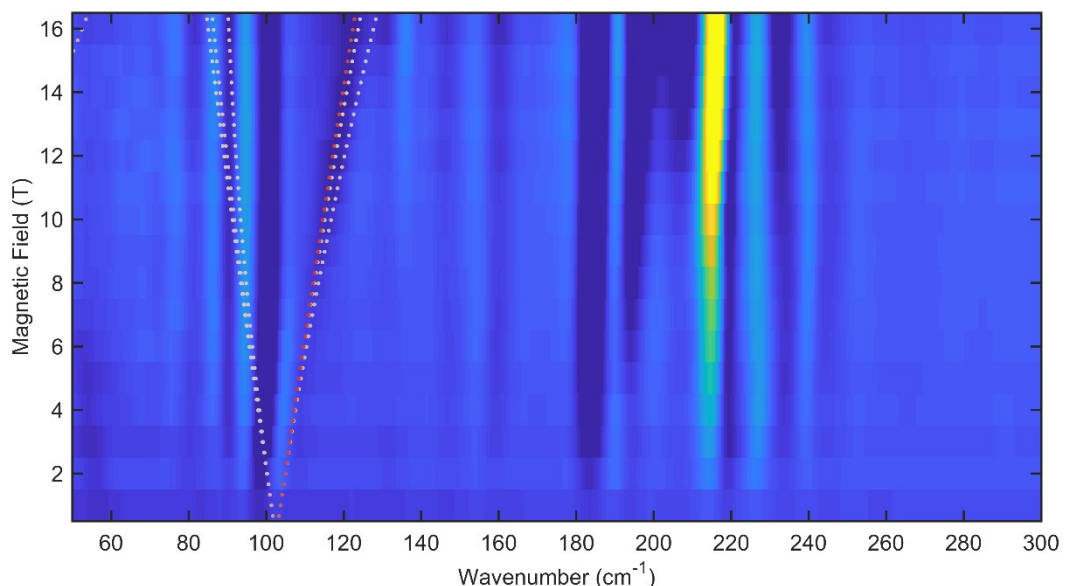


Figure S29 A color map of normalized FIRMS transmission spectra recorded on pressed powder pellet of complex **2** at $T = 4.2\text{ K}$ and magnetic field up to 16 T . Simulation with the SH ($S = 3/2$, $D = -47\text{ cm}^{-1}$, $E/D = 0.251$, $g_{\text{iso}} = 2.5$) is shown as dotted lines. Red color represents the strongly allowed transitions; grey color indicates forbidden/weakly allowed transitions. The tendency toward the yellow color means the absorption is suppressed by the magnetic field, whereas the dark blue color corresponds to the absorption induced by the magnetic field. Spectra were normalized by zero-field transmission spectra division and corresponding reference transmission spectra division.

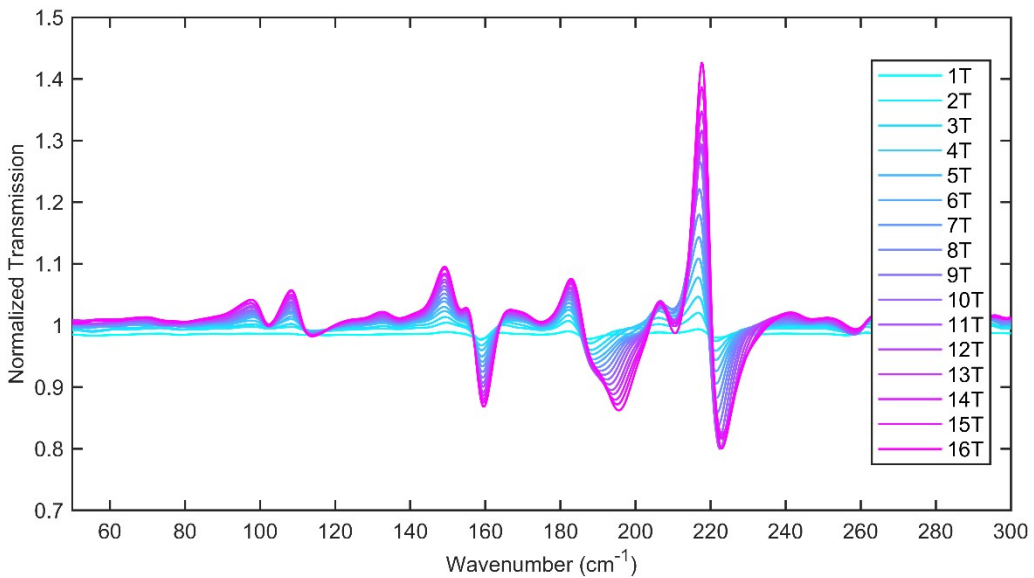


Figure S30 Normalized FIRMS transmission spectra recorded on pressed powder pellet of complex **3** at $T = 4.2\text{ K}$ and magnetic field up to 16 T . Spectra were normalized by zero-field transmission spectra division and corresponding reference transmission spectra division.

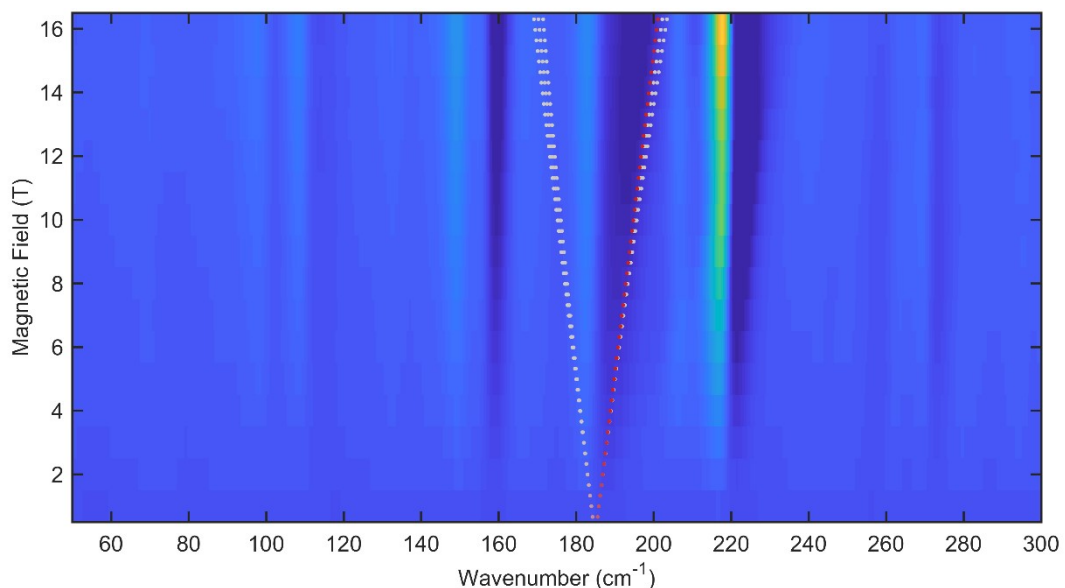


Figure S31 A color map of normalized FIRMS transmission spectra recorded on pressed powder pellet of complex **3** at $T = 4.2\text{ K}$ and magnetic field up to 16 T . Simulation with the SH ($S = 3/2$, $D = -89\text{ cm}^{-1}$, $E/D = 0.162$, $g_{\text{iso}} = 2.1$) is shown as dotted lines. Red color represents the strongly allowed transitions; grey color indicates forbidden/weakly allowed transitions. The tendency toward the yellow color means the absorption is suppressed by the magnetic field, whereas the dark blue color corresponds to the absorption induced by the magnetic field. Spectra were normalized by zero-field transmission spectra division and corresponding reference transmission spectra division.

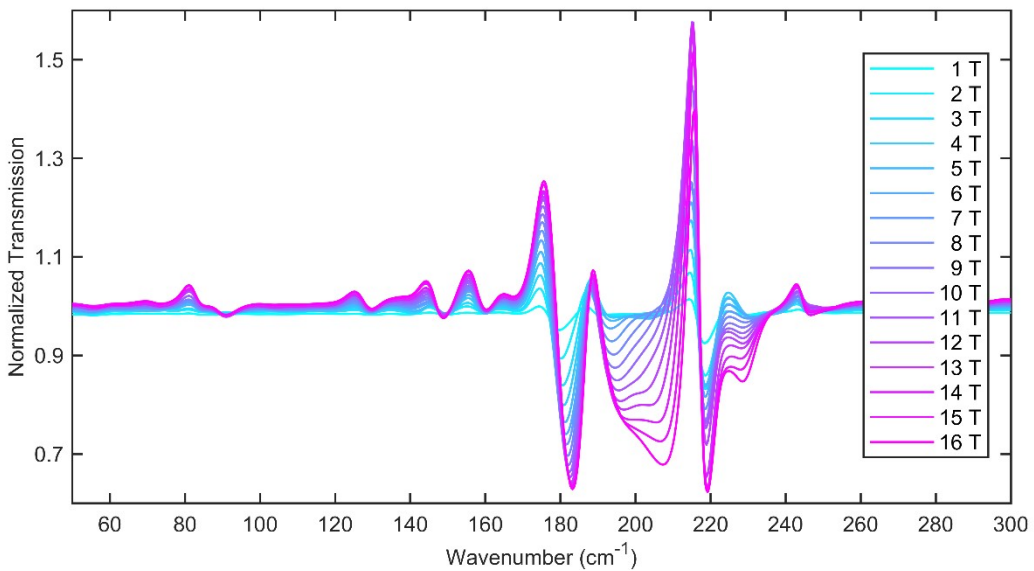


Figure S32 Normalized FIRMS transmission spectra recorded on pressed powder pellet of complex **4** at $T = 4.2\text{ K}$ and magnetic field up to 16 T . Spectra were normalized by zero-field transmission spectra division and corresponding reference transmission spectra division.

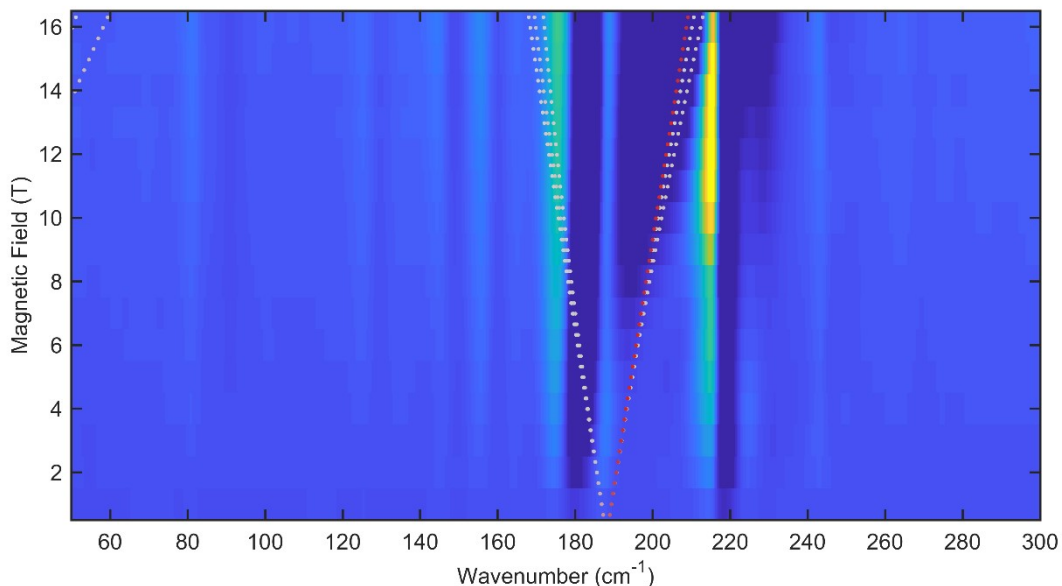


Figure S33 A color map of normalized FIRMS transmission spectra recorded on pressed powder pellet of complex **4** at $T = 4.2\text{ K}$ and magnetic field up to 16 T . Simulation with the SH ($S = 3/2$, $D = -89\text{ cm}^{-1}$, $E/D = 0.197$, $g_{\text{iso}} = 2.7$). Red color represents the strongly allowed transitions; grey color indicates forbidden/weakly allowed transitions. The tendency toward the yellow color means the absorption is suppressed by the magnetic field, whereas the dark blue color corresponds to the absorption induced by the magnetic field. Spectra were normalized by zero-field transmission spectra division and corresponding reference transmission spectra division.

In addition, spectra were normalized by dividing a transmission spectrum measured at B_0 by a spectrum measured at $B_0 + 1\text{ T}$ and depicted as a color map (see Figures S34- S37).

In the FIRMS color map of **1** (Figure S34), no features are observed. However, the FIRMS color map of **2** (Figure S35) revealed several weak field-dependent parallel features moving with the field to the right that appeared at zero-field around 100 cm^{-1} , 190 cm^{-1} , and 220 cm^{-1} . For complex **3** (Figure S36), these features we observed around 160 cm^{-1} , 190 cm^{-1} , and

220 cm^{-1} . In case of complex **4** (Figure S37), they occurred around 140 cm^{-1} , 190 cm^{-1} , and 220 cm^{-1} . We do not have satisfactory explanations for these interesting features yet, but they could be related to vibronic (spin-phonon) coupling^{26,27}. Since our main interest in this work was to find ZFS parameters, appropriate interpretation of these features will be our concern in future work.

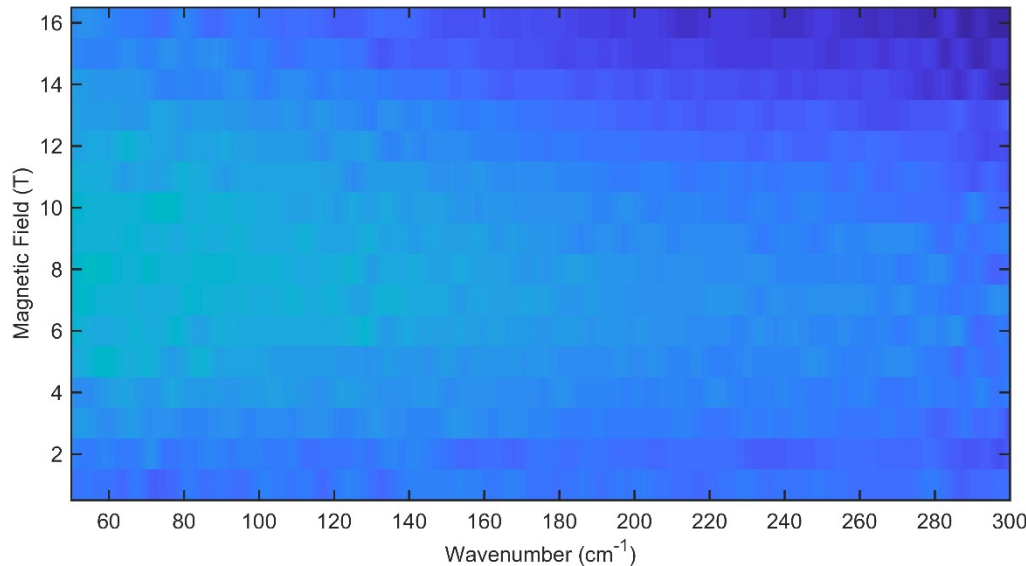


Figure S34 A color map of normalized FIRMS transmission spectra recorded on pressed powder pellet of complex **1** at $T = 4.2\text{ K}$ and magnetic field up to 16 T . Spectra were normalized by dividing a spectrum measured at B_0 by a spectrum measured at $B_0 + 1\text{ T}$.

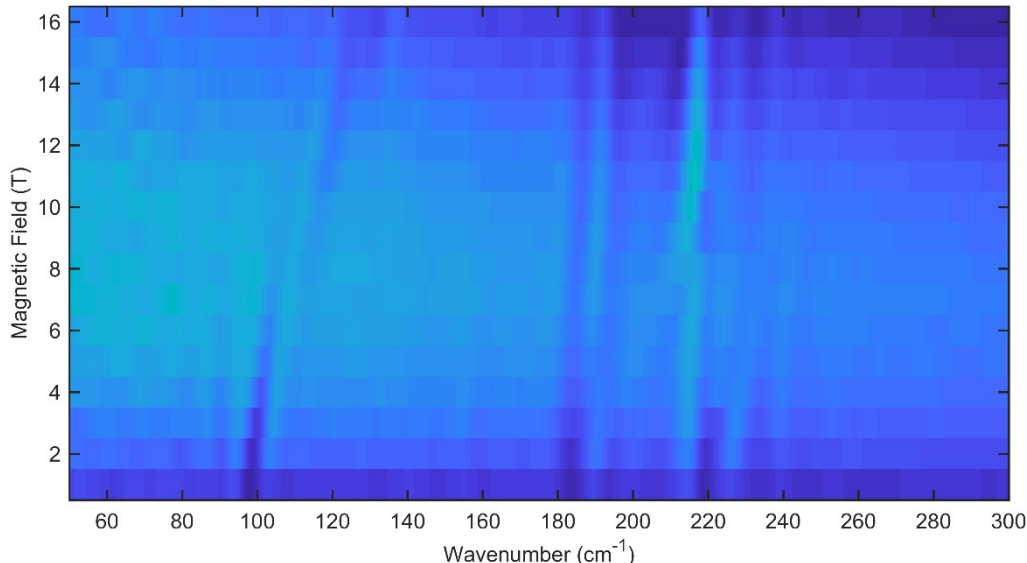


Figure S35 A color map of normalized FIRMS transmission spectra recorded on pressed powder pellet of complex **2** at $T = 4.2\text{ K}$ and magnetic field up to 16 T . Spectra were normalized by dividing a spectrum measured at B_0 by a spectrum measured at $B_0 + 1\text{ T}$. The appearance of the weak field-dependent parallel features moving with the field to the right at zero-field around 100 cm^{-1} , 190 cm^{-1} , and 220 cm^{-1} .

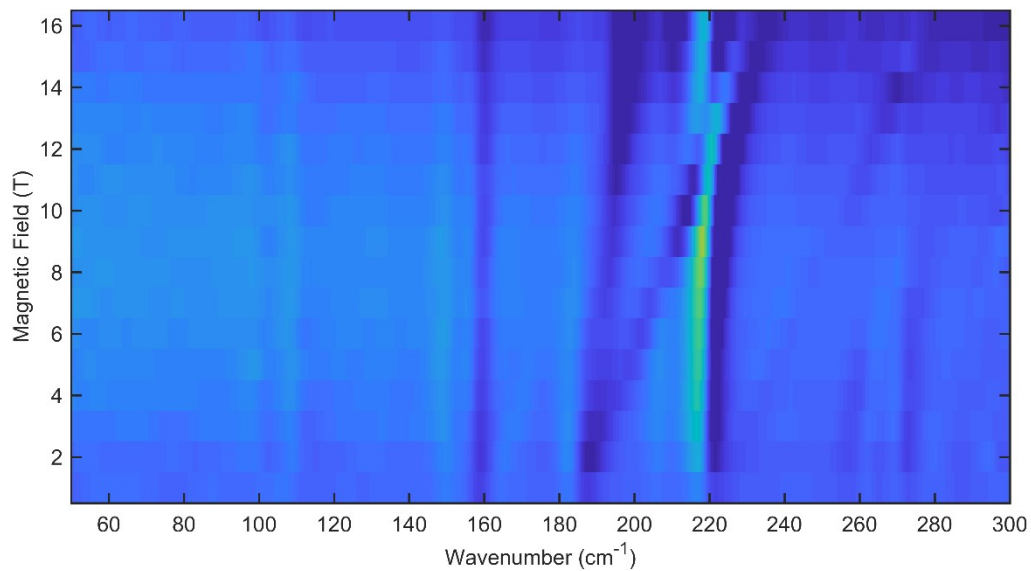


Figure S36 A color map of normalized FIRMS transmission spectra recorded on pressed powder pellet of complex 3 at $T = 4.2 \text{ K}$ and magnetic field up to 16 T. Spectra were normalized by dividing a spectrum measured at B_0 by a spectrum measured at $B_0 + 1 \text{ T}$. The appearance of the weak field-dependent parallel features moving with the field to the right at zero-field around 160 cm^{-1} , 190 cm^{-1} , and 220 cm^{-1} .

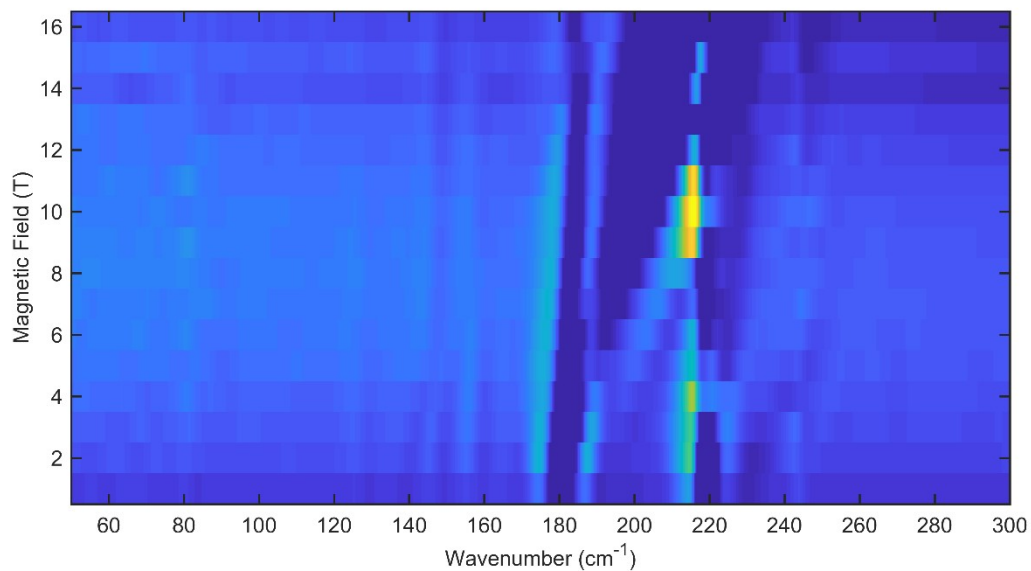


Figure S37 A color map of normalized FIRMS transmission spectra recorded on pressed powder pellet of complex 4 at $T = 4.2 \text{ K}$ and magnetic field up to 16 T. Spectra were normalized by dividing a spectrum measured at B_0 by a spectrum measured at $B_0 + 1 \text{ T}$. The appearance of the weak field-dependent parallel features moving with the field to the right at zero-field around 140 cm^{-1} , 190 cm^{-1} , and 220 cm^{-1} .

S7 Dynamic magnetic investigation

The magnetic data induced by the oscillating, alternating-current (AC) magnetic field were obtained at an amplitude of $B_{AC} = 0.38$ mT. In order to determine the optimum DC field to suppress the quantum tunnelling of magnetization, AC susceptibility measurements under various DC fields were applied at 2 K (Figure S38). The out-of-phase components χ'' reach the maximal response at $B_{DC} = 0.1$ T, therefore the following temperature and frequency dependent AC susceptibility experiments were done at this field.

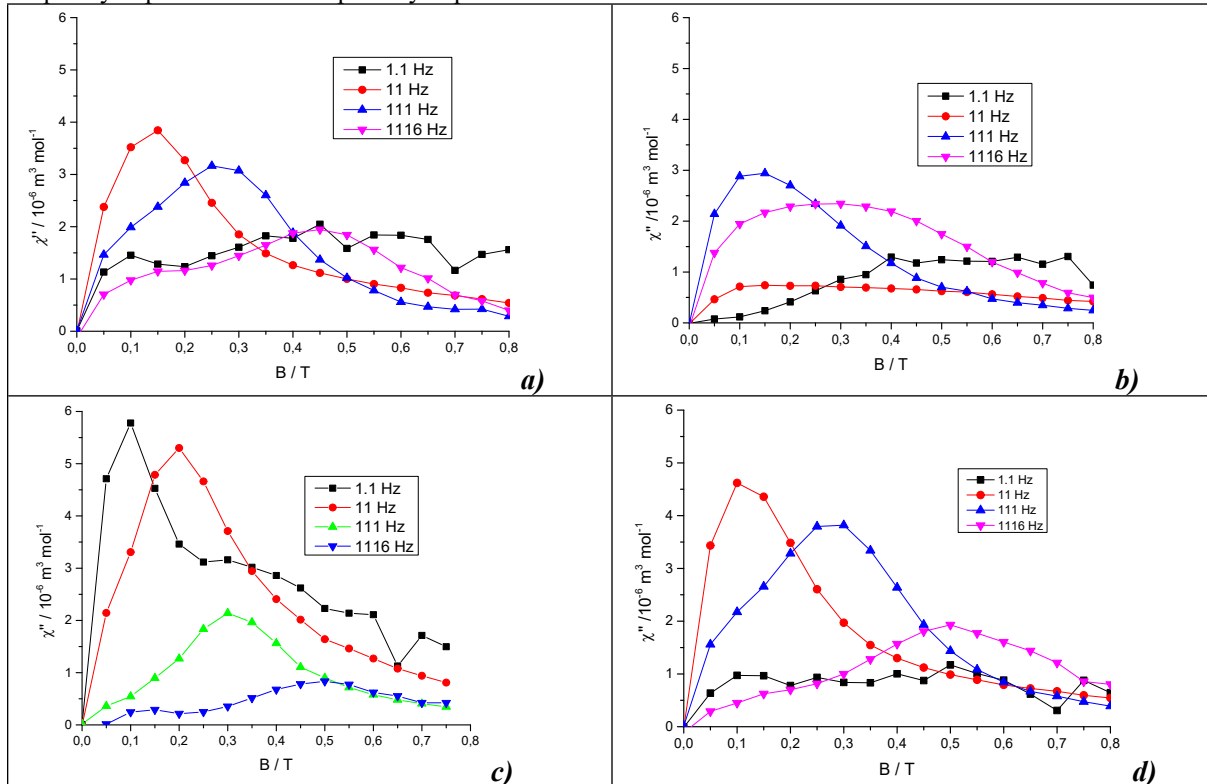


Figure S38 Mapping of the out-of-phase susceptibility components χ'' as functions of the applied external B_{DC} field for a set of four frequencies of the B_{AC} field at $T = 2.0$ K: complex **1** (**a**), **2LT** (**b**), **3** (**c**) and complex **4** (**d**).

Table S6 Conditions of AC magnetic experiments for compounds **1-4**.

	B_{DC} / T	B_{AC} / mT	Temperature range	Frequency range
1	0.1	3.8	1.9-6.3 K (23 steps)	0.1 Hz -1488.1 Hz (22 steps)
2	0.1	3.8	1.9-4.9 K (22 steps)	0.1 Hz -1488.1 Hz (22 steps)
3	0.1	3.8	1.85-6.46 (25 steps)	0.1 Hz -1488.1 Hz (22 steps)
4	0.1	3.5	1.9-5.7 K (21 steps)	0.1 Hz -1488.1 Hz (22 steps)

Collected sets of χ' and χ'' (susceptibilities (22 χ' and 22 χ'') at each temperature were fitted using the formulas for extended one-set Debye model (case of **3** and **4**)

$$\chi'(\omega) = \chi_s + (\chi_t - \chi_s) \frac{1 + (\omega\tau)^{(1-\alpha)} \sin(\pi\alpha/2)}{1 + 2(\omega\tau)^{(1-\alpha)} \sin(\pi\alpha/2) + (\omega\tau)^{(2-2\alpha)}} \quad (\text{S1})$$

$$\chi''(\omega) = (\chi_t - \chi_s) \frac{(\omega\tau)^{(1-\alpha)} \cos(\pi\alpha/2)}{1 + 2(\omega\tau)^{(1-\alpha)} \sin(\pi\alpha/2) + (\omega\tau)^{(2-2\alpha)}} \quad (\text{S2})$$

or two-set Debye model (case of **1** and **2**)

$$\chi'(\omega) = \chi_s + (\chi_{T1} - \chi_s) \frac{1 + (\omega\tau_1)^{(1-\alpha_1)} \sin(\pi\alpha_1/2)}{1 + 2(\omega\tau_1)^{(1-\alpha_1)} \sin(\pi\alpha_1/2) + (\omega\tau_1)^{(2-2\alpha_1)}} \\ + (\chi_{T2} - \chi_{T1}) \frac{1 + (\omega\tau_2)^{(1-\alpha_2)} \sin(\pi\alpha_2/2)}{1 + 2(\omega\tau_2)^{(1-\alpha_2)} \sin(\pi\alpha_2/2) + (\omega\tau_2)^{(2-2\alpha_2)}} \quad (S3)$$

$$\chi''(\omega) = (\chi_{T1} - \chi_s) \frac{(\omega\tau_1)^{(1-\alpha_1)} \cos(\pi\alpha_1/2)}{1 + 2(\omega\tau_1)^{(1-\alpha_1)} \sin(\pi\alpha_1/2) + (\omega\tau_1)^{(2-2\alpha_1)}} \\ + (\chi_{T2} - \chi_{T1}) \frac{(\omega\tau_2)^{(1-\alpha_2)} \cos(\pi\alpha_2/2)}{1 + 2(\omega\tau_2)^{(1-\alpha_2)} \sin(\pi\alpha_2/2) + (\omega\tau_2)^{(2-2\alpha_2)}} \quad (S4)$$

Four (for one relaxation channel; eq S1 and S2l case of **3** and **4**) or seven (for two relaxation channels; eq. S3 and S4; case of **1** and **2**) free parameters can be retrieved reliably by using 22 experimental data points for each temperature.

Table S7 Parameters of the two-set Debye model (eq. S3 and S4) for **1** at $B_{DC} = 0.1$ T.

T / K	$\chi_s /$ 10^{-6} m^3 mol^{-1}	$\chi_{T,LF} /$ 10^{-6} m^3 mol^{-1}	$\chi_{T,HF} /$ 10^{-6} m^3 mol^{-1}	α_{LF}	α_{HF}	τ_{LF} / s	τ_{HF} / s
1.9	2.82967	7.69277	15.01982	0.08358	0.43995	0.02592	0.00321
2.1	2.79084	7.3907	13.62831	0.09086	0.39596	0.02025	0.00257
2.3	2.70399	6.88544	12.65767	0.09921	0.36351	0.01668	0.00234
2.5	2.56979	6.90356	11.65458	0.09845	0.32612	0.01196	0.00159
2.7	2.43464	6.73166	10.85006	0.09555	0.29395	0.00835	0.00118
2.9	2.19331	6.69633	10.16465	0.09085	0.28832	0.00532	7.75069E-4
3.1	2.06848	6.88986	9.55491	0.08815	0.25146	0.00342	4.63414E-4
3.3	1.9508	7.08822	9.03106	0.08927	0.21697	0.00218	2.80009E-4
3.5	1.79247	7.01183	8.56088	0.08739	0.19976	0.00144	1.72463E-4
3.7	1.59816	6.67214	8.13428	0.06916	0.22291	9.78452E-4	1.19871E-4
3.9	1.51248	6.61157	7.75407	0.06865	0.21079	6.64531E-4	7.37945E-5
4.1	1.27538	6.25293	7.40026	0.06091	0.26072	4.63289E-4	4.19526E-5
4.3	1.23575	6.1035	7.08023	0.03925	0.22386	3.28882E-4	2.50624E-5
4.5	1.25735	5.38346	6.78783	0.00447	0.24258	4.63289E-4	5.09381E-5
4.7	1.23847	5.3923	6.52438	0.00421	0.22685	1.92869E-4	3.17468E-5
4.9	1.22416	5.33469	6.27589	0.00439	0.22964	1.41345E-4	2.75411E-5
5.1	1.24717	5.24802	6.05526	0.00451	0.22754	1.08024E-4	2.15009E-5
5.3	1.19601	4.96895	5.84634	0.00446	0.1889	8.42509E-5	2.05434E-5
5.5	1.24251	5.17655	5.64381	0.00506	0.10984	6.42112E-5	1.1643E-5
5.7	1.28951	5.05945	5.45414	0.00517	0.10649	5.15693E-5	8.21952E-6
5.9	1.34293	4.67873	5.28212	0.00463	0.13355	4.39481E-5	9.09615E-6

6.1	1.40305	4.83709	5.11529	0.00473	0.11468	3.41161E-5	6.08826E-6
-----	---------	---------	---------	---------	---------	------------	------------

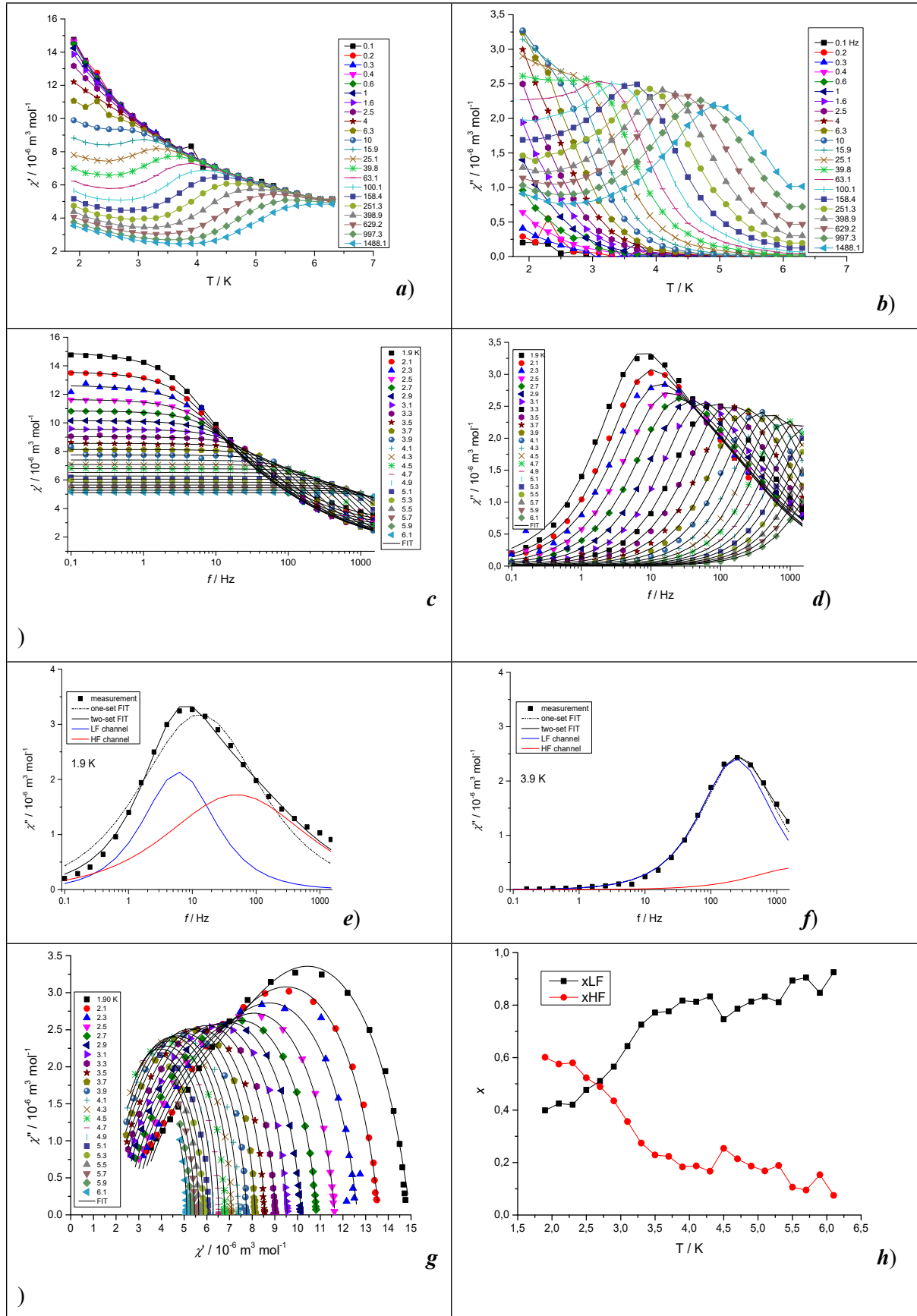
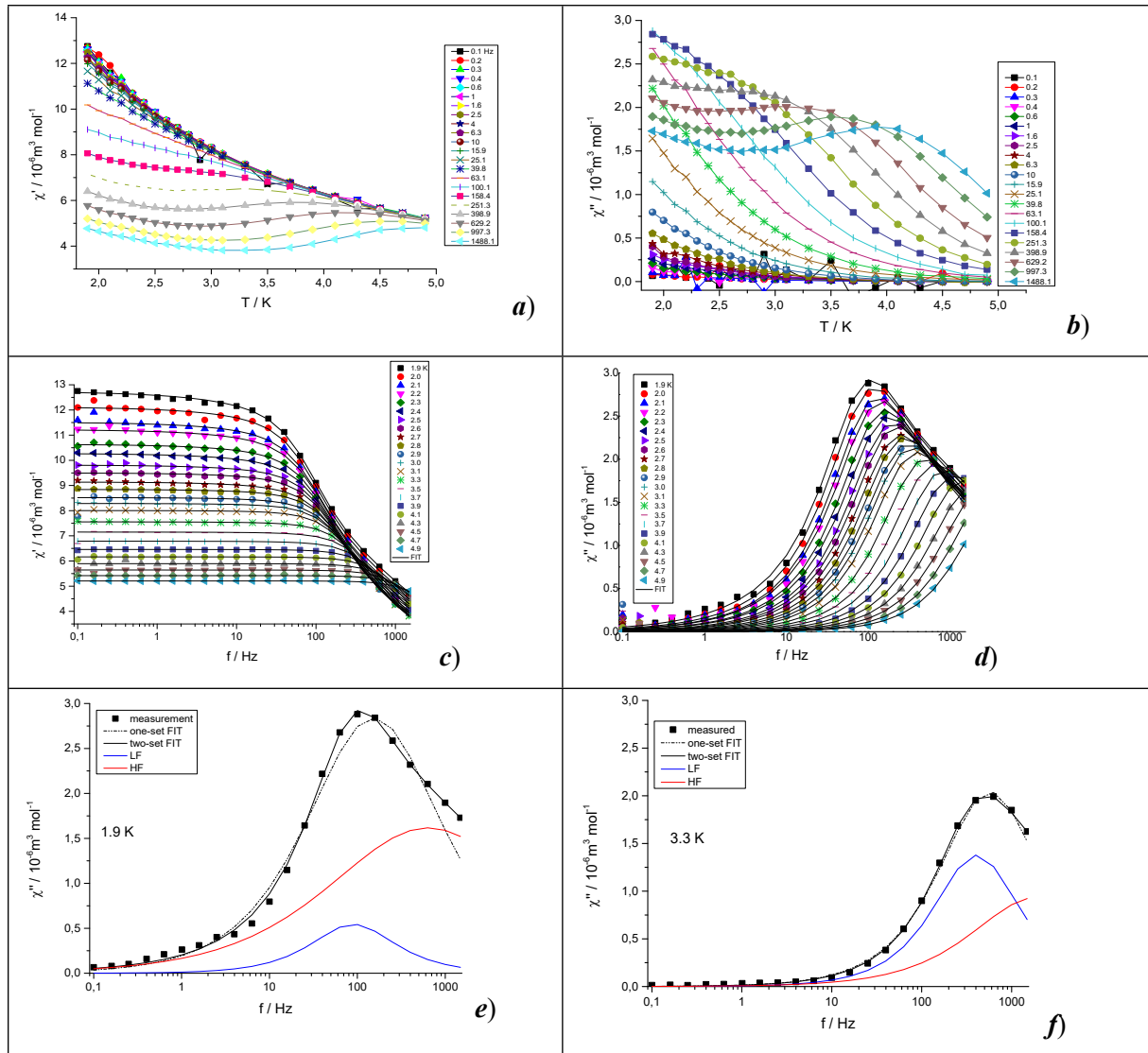


Figure S39 AC susceptibility data for **1** recorded at $B_{DC}=0.1$ T: Temperature dependence of in-phase χ' (**a**) and out-of-phase χ'' (**b**) components of AC susceptibility (solid lines are guides for the eyes). Frequency dependent in-phase χ' (**c**) and out-of-phase χ'' (**d**) component of AC susceptibility; solid lines are fits according to equations S3 and S4. The best fits of out-of-phase AC susceptibility with respect to one-set (dotted black line) and two-set (solid black line) Debye model and deconvolution of two-set fit to LF (blue solid line) and HF (red solid line) relaxation channels for temperatures 1.9 K (**e**) and 3.3 K (**f**). Cole-Cole diagram (**g**). Temperature evolution of LF and HF branches (**h**).

Table S8 Parameters of the two-set Debye model (eq. S3 and S4) for **2** at $B_{DC} = 0.1$ T.

T/K	$\chi_s / 10^{-6} \text{ mol}^{-1} \text{ m}^3$	$\chi_{T,LF} / 10^{-6} \text{ mol}^{-1} \text{ m}^3$	$\chi_{T,HF} / 10^{-6} \text{ mol}^{-1} \text{ m}^3$	α_{LF}	α_{HF}	τ_{LF} / s	τ_{HF} / s
1.9	2.05817	5.46099	12.73431	3.65E-16	0.46637	0.00177	2.5015E-4
2	2.17846	5.57448	12.11642	3.86E-16	0.43632	0.00164	2.34392E-4
2.1	2.07875	5.46998	11.51318	4.21E-16	0.42993	0.00148	1.96093E-4
2.2	2.10538	5.39612	11.22119	4.41E-16	0.42989	0.00135	1.99653E-4
2.3	1.98778	5.30437	10.63689	4.65E-16	0.41606	0.0012	1.58848E-4
2.4	1.87905	5.08995	10.27351	5.28E-16	0.4199	0.00107	1.45728E-4
2.5	1.9745	5.19393	9.81165	5.54E-16	0.39298	9.52564E-4	1.32978E-4
2.6	2.02981	5.18967	9.49982	5.92E-16	0.3746	8.6127E-4	1.35094E-4
2.7	2.20997	5.1246	9.13746	6.78E-16	0.35221	7.77973E-4	1.53679E-4
2.8	2.0573	5.08807	8.84412	7.42E-16	0.33404	6.98687E-4	1.17373E-4
2.9	2.1343	5.03965	8.52015	9.09E-16	0.30164	6.36066E-4	1.19222E-4
3.0	2.19112	5.05659	8.28547	10.29E-16	0.26245	5.86159E-4	1.14324E-4
3.1	2.30654	4.9927	8.00443	11.81E-16	0.21914	5.28294E-4	1.22386E-4
3.3	2.08486	4.84267	7.55507	11.07E-16	0.2329	3.90686E-4	8.51685E-5
3.5	1.82486	4.65829	7.15064	11.74E-16	0.25191	2.86057E-4	5.47501E-5
3.7	1.64549	4.4624	6.7876	12.77E-16	0.2447	2.21247E-4	3.7926E-5
3.9	0.33681	3.12073	6.4591	27.48E-16	0.19413	1.78464E-4	1.46197E-5
4.1	0.35391	3.08795	6.1654	26.34E-16	0.18692	1.34105E-4	1.12346E-5
4.3	0.36218	3.05051	5.89475	25.86E-16	0.18489	1.01505E-4	7.71289E-6

4.5	0.36347	3.00404	5.64301	25.65E-16	0.18387	7.64144E-5	5.923E-6
4.7	0.37213	3.08268	5.41998	28.37E-16	0.15735	5.71372E-5	4.04331E-6
4.9	0.25616	2.8994	5.20805	28.24E-16	0.1519	4.4502E-5	2.11233E-6



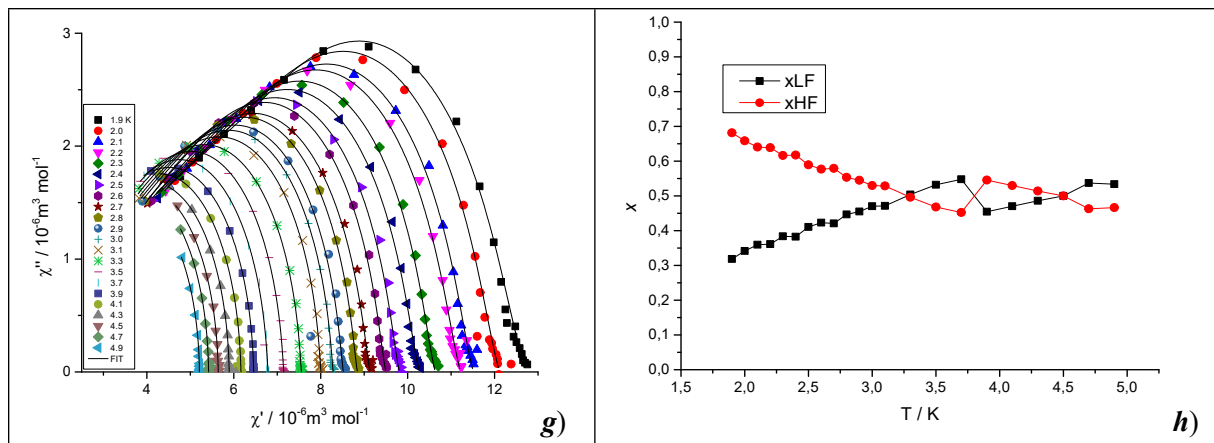


Figure S40 AC susceptibility data for **2** recorded at $B_{DC}=0.1$ T: Temperature dependence of in-phase χ' (**a**) and out-of-phase χ'' (**b**) components of AC susceptibility (solid lines are guides for the eyes). Frequency dependent in-phase χ' (**c**) and out-of-phase χ'' (**d**) component of AC susceptibility; solid lines are fits according to equations S3 and S4. The best fits of out-of-phase AC susceptibility with respect to one-set (dotted black line) and two-set (solid black line) Debye model and deconvolution of two-set fit to LF (blue solid line) and HF (red solid line) relaxation channels for temperatures 1.9 K (**e**) and 3.3 K (**f**). Cole-Cole diagram (**g**). Temperature evolution of LF and HF branches (**h**).

Table S9 Parameters of the extended one-set Debye model (eq. S1 and S2) for **3** at $B_{DC} = 0.1$ T.

T/K	$\chi_s/10^{-6} \text{ m}^3 \text{ mol}^{-1}$	$\chi_t/10^{-6} \text{ m}^3 \text{ mol}^{-1}$	α	τ/s
1.85	2.83148	21.63659	0.11568	0.08861
2.0	2.59581	20.12841	0.11606	0.07271
2.21	2.39672	18.58346	0.11073	0.05793
2.41	2.17864	16.93429	0.11203	0.04212
2.61	1.99603	15.60205	0.10431	0.03008
2.81	1.84397	14.41552	0.09864	0.02026
3.02	1.71639	13.4784	0.0902	0.01336
3.22	1.6024	12.63426	0.07707	0.00845
3.42	1.51346	11.86551	0.06042	0.00525
3.62	1.42167	11.21387	0.04832	0.00329
3.83	1.34735	10.62505	0.03789	0.00208
4.03	1.23818	10.13485	0.04273	0.00133
4.23	1.21477	9.64539	0.02582	8.79772E-4
4.43	1.08729	9.21046	0.02519	5.79826E-4
4.64	1.06591	8.82117	0.01989	4.00549E-4
4.84	1.00412	8.46634	0.01898	2.81474E-4
5.04	0.93292	8.13632	0.01848	2.00132E-4
5.24	0.89518	7.83745	0.01946	1.45899E-4
5.44	0.76136	7.55958	0.02231	1.06836E-4
5.65	0.68533	7.29268	0.02524	7.96902E-5
5.85	0.7115	7.04933	0.02366	6.16282E-5

6.05	0.7378	6.81749	0.02372	4.82258E-5
6.26	0.66823	6.59738	0.01558	3.80864E-5
6.46	0.71908	6.39836	0.01757	3.07219E-5

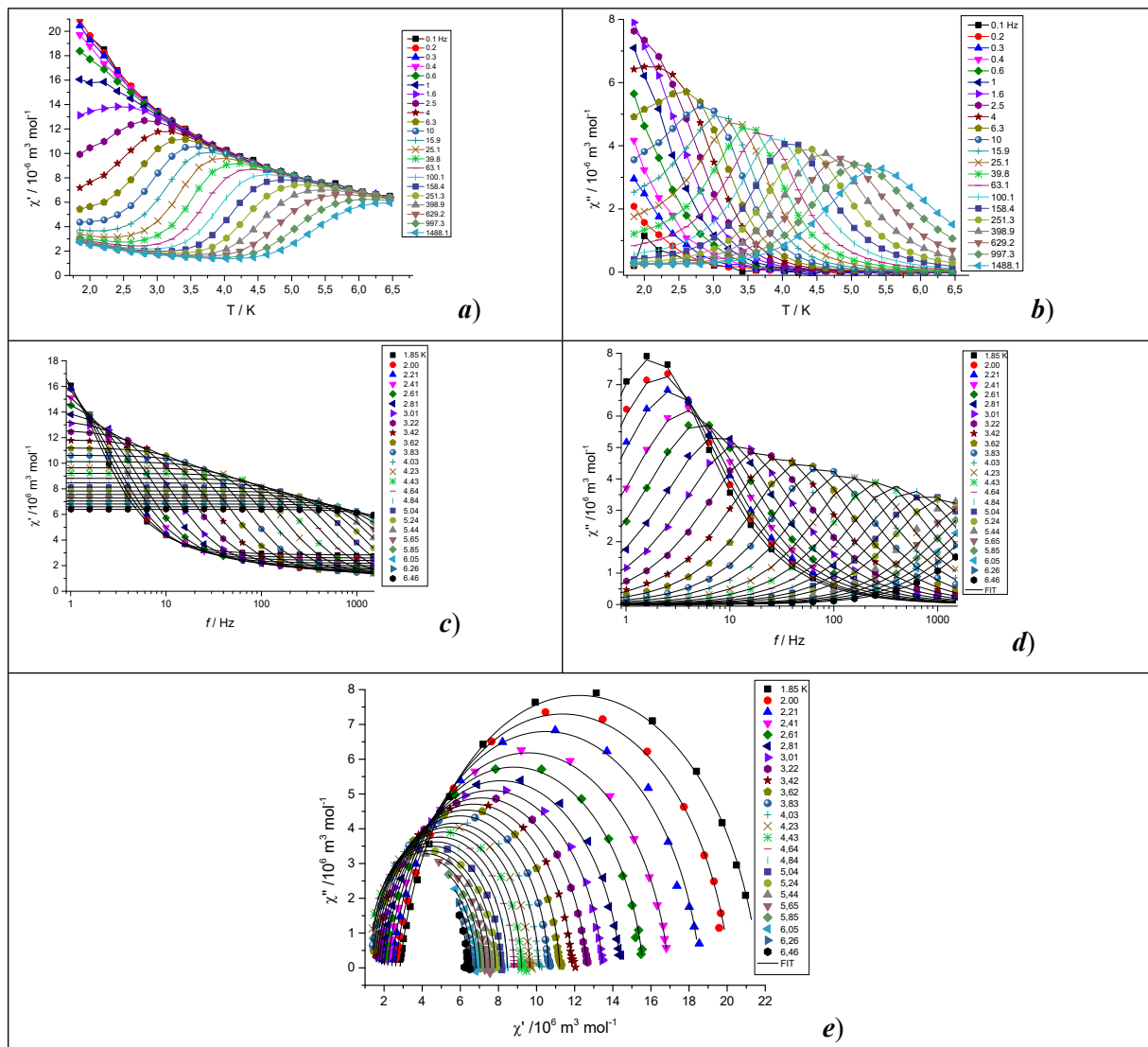
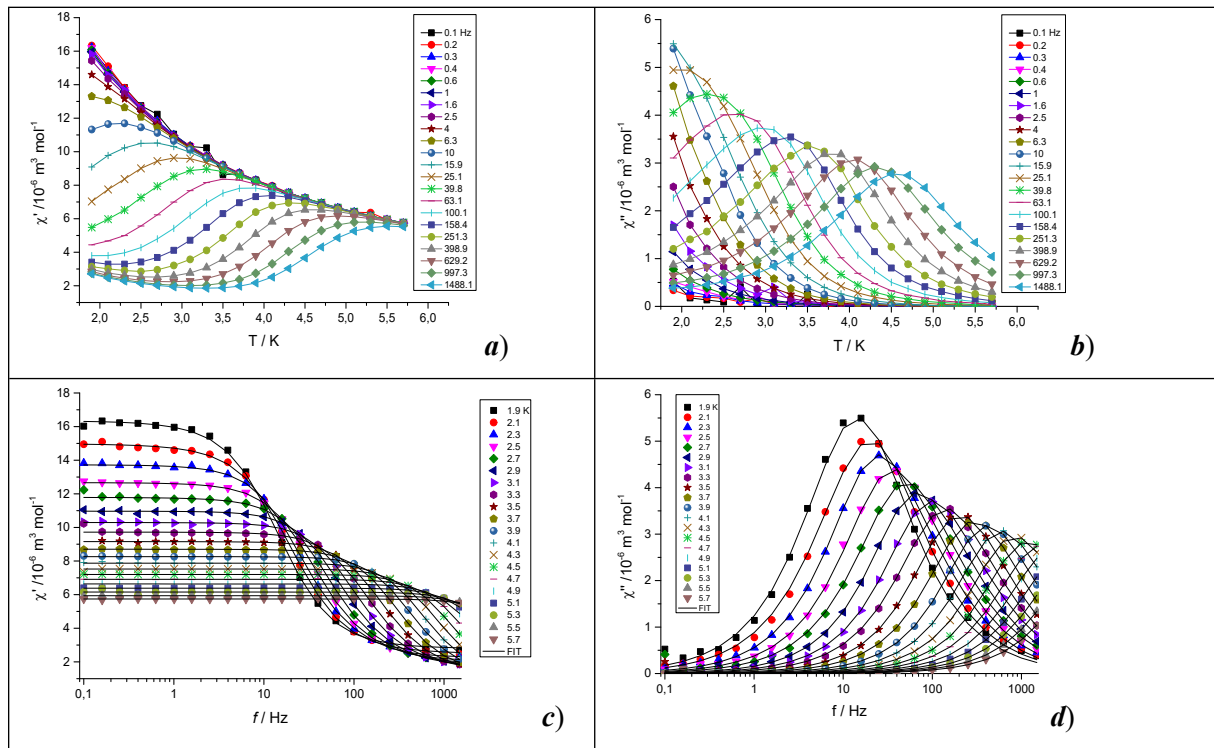


Figure S41 AC susceptibility data for **3** recorded at $B_{DC}=0.1$ T: Temperature dependence of in-phase χ' (**a**) and out-of-phase χ'' (**b**) components of AC susceptibility (solid lines are guides for the eyes). Frequency dependent in-phase χ' (**c**) and out-of-phase χ'' (**d**) component of AC susceptibility; solid lines are results of fits according to equations S1 and S2. Cole-Cole diagram (**e**).

Table S10 Parameters of the extended one-set Debye model (eq. S1 and S2) for **4** at $B_{DC} = 0.1$ T.

T / K	$\chi_s / 10^{-6} \text{ m}^3 \text{ mol}^{-1}$	$\chi_T / 10^{-6} \text{ m}^3 \text{ mol}^{-1}$	α	τ / s
1.9	2.78311	16.34926	0.13154	0.01096
2.1	2.48498	14.97783	0.13821	0.00783
2.3	2.25155	13.84417	0.13172	0.00573
2.5	2.07039	12.7239	0.12563	0.00409
2.7	1.91923	11.83657	0.12102	0.00291
2.9	1.81026	11.00735	0.10123	0.00209

3.1	1.70231	10.32408	0.09666	0.00149
3.3	1.62528	9.71989	0.08185	0.00105
3.5	1.57141	9.17345	0.0627	7.44706E-4
3.7	1.50827	8.70038	0.05582	5.17955E-4
3.9	1.46439	8.27128	0.04092	3.64948E-4
4.1	1.3915	7.88776	0.03484	2.60293E-4
4.3	1.32232	7.52783	0.02634	1.85529E-4
4.5	1.33004	7.20663	0.02029	1.35556E-4
4.7	1.25691	6.91354	0.01888	9.9037E-5
4.9	1.15581	6.64005	0.01949	7.24514E-5
5.1	1.10283	6.38978	0.02067	5.37001E-5
5.3	0.88734	6.15873	0.0233	3.90019E-5
5.5	1.04804	5.94181	0.01892	3.14955E-5
5.7	1.07254	5.74106	0.00519	2.5137E-5



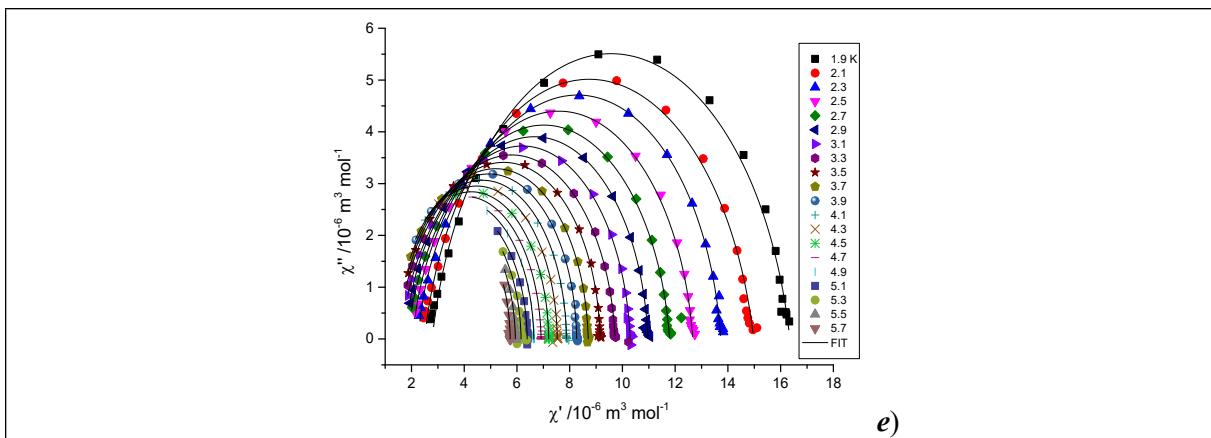


Figure S42 AC susceptibility data for **4** recorded at $B_{DC}=0.1$ T: Temperature dependence of in-phase χ' (**a**) and out-of-phase χ'' (**b**) components of AC susceptibility (solid lines are guides for the eyes). Frequency dependent in-phase χ' (**c**) and out-of-phase χ'' (**d**) component of AC susceptibility; solid lines are results of fits according to equations S1 and S2. Cole-Cole diagram (**e**).

Table S11 Relaxation parameters at $B_{DC} = 0.1$ T for compound **1** using the respective combinations of Orbach, Raman and direct processes of relaxation.

Model	$U/k_B / K$	τ_0/s	$C / K^{-n} s^{-1}; n$	$AB^m / T^{-m} K^{-1} s^{-1}$	R^2
LF channel					
Orbach+Raman	32.7(6)	$1.8(2) \times 10^{-7}$	6.8(13) 2.6(3)	-	0.9994
Orbach+direct	30.4(5)	$2.8(3) \times 10^{-7}$	-	23.1(11)	0.9985
Raman+direct	-	-	$8.3(12) \times 10^{-2}$	14.3(12)	0.9988
Orbach+Raman+direct	28.1(12)	$9(2) \times 10^{-7}$	$2(1) \times 10^{-2}$ 7.1(1) 7.6(3)	19.2(8)	0.9999
HF channel					
Orbach+Raman	26.3(12)	$1.0(3) \times 10^{-7}$	322(132) 9×10^{-13}	-	0.9864
Orbach+direct	27.0(12)	$9.0(25) \times 10^{-8}$	-	156(24)	0.9869
Raman+direct	-	-	1.6(9) 6.4(3)	79(39)	0.9799
Orbach+Raman+direct	28.1(12)	$9(2) \times 10^{-7}$	0.02(1) 7.6(3)	19.2(8)	0.99988

Table S12 Relaxation parameters at $B_{DC} = 0.1$ T for compound **2** using the respective combinations of Orbach, Raman and Direct processes of relaxation.

Model	$U/k_B / K$	τ_0/s	$C / K^{-n} s^{-1}; n$	$AB^m / T^{-m} K^{-1} s^{-1}$	R^2
LF channel					
Orbach+Raman	33.4(11)	$6.2(15) \times 10^{-8}$	122(9) 2.3(1)	-	0.9994
Orbach+direct	24.9(9)	$3.4(7) \times 10^{-7}$	-	330(11)	0.9957
Raman+direct	-	-	0.9(1) 6.3(1)	283(7)	0.9990
Orbach+Raman+direct	38(4)	$3(2) \times 10^{-8}$	11(11) 4.2(9)	212(43)	0.9994
HF channel					

Orbach+Raman	45(3)	$1.9(14) \times 10^{-10}$	1953(554)	-	0.9901
Orbach+direct	45(2)	$2.5(14) \times 10^{-10}$	1.3(3)	2487(112)	0.9901
Raman+direct	-	-	$1.3(12) \times 10^{-2}$	2374(132)	0.9883
Orbach+Raman+direct	46(4)	$1.9(15) \times 10^{-10}$	1950(1393)	10.9(6) 1.3(4)	0

Table S13 Relaxation parameters at $B_{DC} = 0.1$ T for compound **3** using the respective combinations of Orbach, Raman and Direct processes of relaxation.

Model	$U/k_B / K$	τ_0/s	$C / K^{-n} s^{-1}; n$	$AB^m / T^m K^{-1} s^{-1}$	R^2
Orbach	37.0(7)	$1.19(1) \times 10^{-7}$	-	-	0.9935
Raman	-	-	$8.30(3) \times 10^{-3}$ 8.20(6)	-	0.9993
Obach+Raman	41.6(5)	$5.3(5) \times 10^{-8}$	1.3(2) 3.3(1)	-	0.9996
Orbach+direct	37.4(8)	$1.1(2) \times 10^{-7}$	-	8.1(6)	0.9967
Raman+direct	-	-	$6.0(6) \times 10^{-3}$ 8.39(6)	5.6(3)	0.9995
Orbach+Raman+direct	44.9(2)	$4.4(3) \times 10^{-8}$	$2.2(4) \times 10^{-2}$ 7.0(2)	5.3(1)	0.9999

^afor data in the range 3.22 K -6.46 K

Table S14 Relaxation parameters at $B_{DC} = 0.1$ T for compound **4** using the respective combinations of Orbach, Raman and Direct processes of relaxation.

Model	$U/k_B / K$	τ_0/s	$C / K^{-n} s^{-1}; n$	$AB^m / T^m K^{-1} s^{-1}$	R^2
Orbach ^a	31.3(8)	$1.16(2) \times 10^{-7}$	-	-	0.9921
Raman ^a	-	-	0.184(7) 7.07(6)	-	0.9993
Obach+Raman	39.7(7)	$2.8(4) \times 10^{-8}$	7.6(5) 3.81(8)	-	0.9998
Orbach+direct	29.9(11)	$1.6(4) \times 10^{-7}$	-	65.6(58)	0.9933
Raman+direct	-	-	0.18(2) 7.08(8)	44.6(22)	0.9993
Orbach+Raman+direct	43.9(11)	$1.7(2) \times 10^{-8}$	1.5(4) 5.2(2)	26(3)	0.9999

^afor data in the range 3.5 K -5.7 K

Table S15 Isostructural and isomorphic pentacoordinate complexes with chlorido (green) and bromido (brown) terminal ligands.

Isostructural couples, closest symmetry of polyhedra, parameter	D / cm ⁻¹ ; E / D	Relaxation time τ /ms	Relaxation parameters			ref.
			U / K τ_0 / s	C / K ⁻ⁿ s ⁻¹ n / s	AB ^m / T ^{-m} K ⁻¹ s ⁻¹	
1 [Co(C8bbp)Cl₂]	-69; 0 ^m	@1.9K: $\tau_{LF}=25.92$; $\tau_{HF}=3.21$	<i>LF:</i> 30.4 ^{OD} 2.8×10^{-7} <i>HF:</i> 27.0 ^{OD} 9×10^{-8}	<i>LF:</i> 0.08 RD 7.1 <i>HF:</i> 1.6 RD 6.4	<i>LF:</i> 23.1 ^{OD} 14.3 RD <i>HF:</i> 155 ^{OD} 79 RD	
2LT Co(C8bbp)Br₂	-42.9; 0 ^m	@1.9K: $\tau_{LF}=1.77$; $\tau_{HF}=0.25$	<i>LF:</i> 25.0 ^{OD} 3.4×10^{-7} <i>HF:</i> 44.9 ^{OD} 2×10^{-10}	<i>LF:</i> 0.9 RD 6.3 <i>HF:</i> 0.01 RD 10.9	<i>LF:</i> 330 ^{OD} 283 RD <i>HF:</i> 2487 ^{OD} 2374 RD	t h i s w o r k
SPY, $\delta = 34.13^\circ$			$\tau_1(Cl)/\tau_1(Br) = 14.6$ $\tau_2(Cl)/\tau_2(Br) = 12.8$			
1 [Co(C8bbp)Cl₂]	-69; 0 ^m	@1.9K: $\tau_{LF}=25.92$; $\tau_{HF}=3.21$	-	-	-	
2HT[Co(C8bbp)Br₂] 1	-98; 0 ^a	-	-	-	-	
SPY, $\delta = 14.8^\circ$						
3 Co(C12bbp)Cl₂]	-78(2); 0 ^m	@1.85K: $\tau=88.61$	44.9 ^f 4.4×10^{-8}	0.02 ^f 7.0	5.3 ^f	
4 [Co(C12bbp)Br₂]	-66(1); 0 ^m	@1.9K: $\tau=10.96$	43.9 ^f 1.7×10^{-8}	1.5 ^f 5.2	26 ^f	
SPY, $\delta (3-4) = 5.15^\circ$			$\tau(Cl)/\tau(Br)=8.1$			
[Co(bbP)Cl₂]·MeOH	+14.5; 0.0 ^m	@2K: $\tau=9.1$	19.6; 5.8×10^{-5}	no	no	28
[Co(bbP)Br₂]·MeOH	+8.4; 0 ^m	@2K: $\tau=4.8$	8.2; 3.1×10^{-5}	no	no	
SPY, $\delta = 17.5^\circ$			$\tau(Cl)/\tau(Br)=1.9$			
[Co(bbP)Cl₂]·DMF	+58.4; 0 ^m	@2K: $\tau_{LF}=162$; $\tau_{HF}=0.3$	33.2 ^{OD} 4.7×10^{-8}	4.2 RD 5	1808 ^{OD} 652 RD	29
[Co(bbP)Br₂]·DMF	+47.0; 0 ^m	@2K: $\tau_{LF}=19.3$; $\tau_{HF}=0.5$	21 5.7×10^{-7}	9.31 RD 5	252 RD	
SPY, $\delta = 4.72^\circ$			$\tau_{LF}(Cl)/\tau_{LF}(Br) = 8.4$ $\tau_{HF}(Cl)/\tau_{HF}(Br) = 0.6$			
[Co(tBuBzbbp)Cl₂]	+26.4; 1/3 ^m	@2K: $\tau=0.5$	19 ^{OD} 2.3×10^{-7}	14.9 RD 5.8	893 ^{OD} 633 RD	30
[Co(tBuBzbbp)Br₂]	+39.2; 1/3 ^m	@2K: $\tau=0.6$	20 ^{OD} 7×10^{-8}	5 RD 7.4	713 ^{OD} 559 RD	
TBPY, $\delta = 16.5^\circ$			$\tau(Cl)/\tau(Br) = 0.8$			
[Co(L)Cl]Cl cubic	-8.49; 0 ^m	@1.8K: $\tau_{LF}=14.4$; $\tau_{HF}=0.12$	<i>LF:</i> 18 ^{OR} 2.3×10^{-7}	<i>LF:</i> 0.0086 ^{OR} 6.46	no	31
[Co(L)Br]Br cubic	-7.18; 0 ^m	@1.8K: $\tau_{LF}=0.72$	<i>LF:</i> 20 ^{OR} 3.6×10^{-1}	<i>LF:</i> 0.0042 ^{OR} 7.05	no	

TBPY, $\delta = 1.1^\circ$	$\tau_{LF}(Cl)/\tau_{LF}(Br) = 2.5$	O	
----------------------------	-------------------------------------	---	--

a-ab *initio* calculations; **m**-magnetic experiments; **no**-not operative; **OD**-Orbach+direct fitting; **RD**-Raman+direct fitting; **OR**-Orbach+Raman fitting; **f**- Orbach+Raman+direct fitting; **LF**-parameters for low-frequency channel, **HF**- parameters for high-frequency channel. bbp = 2,6-bis(benzimidazole-1-yl)pyridine, tBuBzbbp=2,6-Bis(1-(3,5-di-tert-butylbenzyl)-1*H*-benzimidazol-2-yl)pyridine and L=tris(2-pyridylmethyl)amine.

S8 Lithography and sublimation deposition

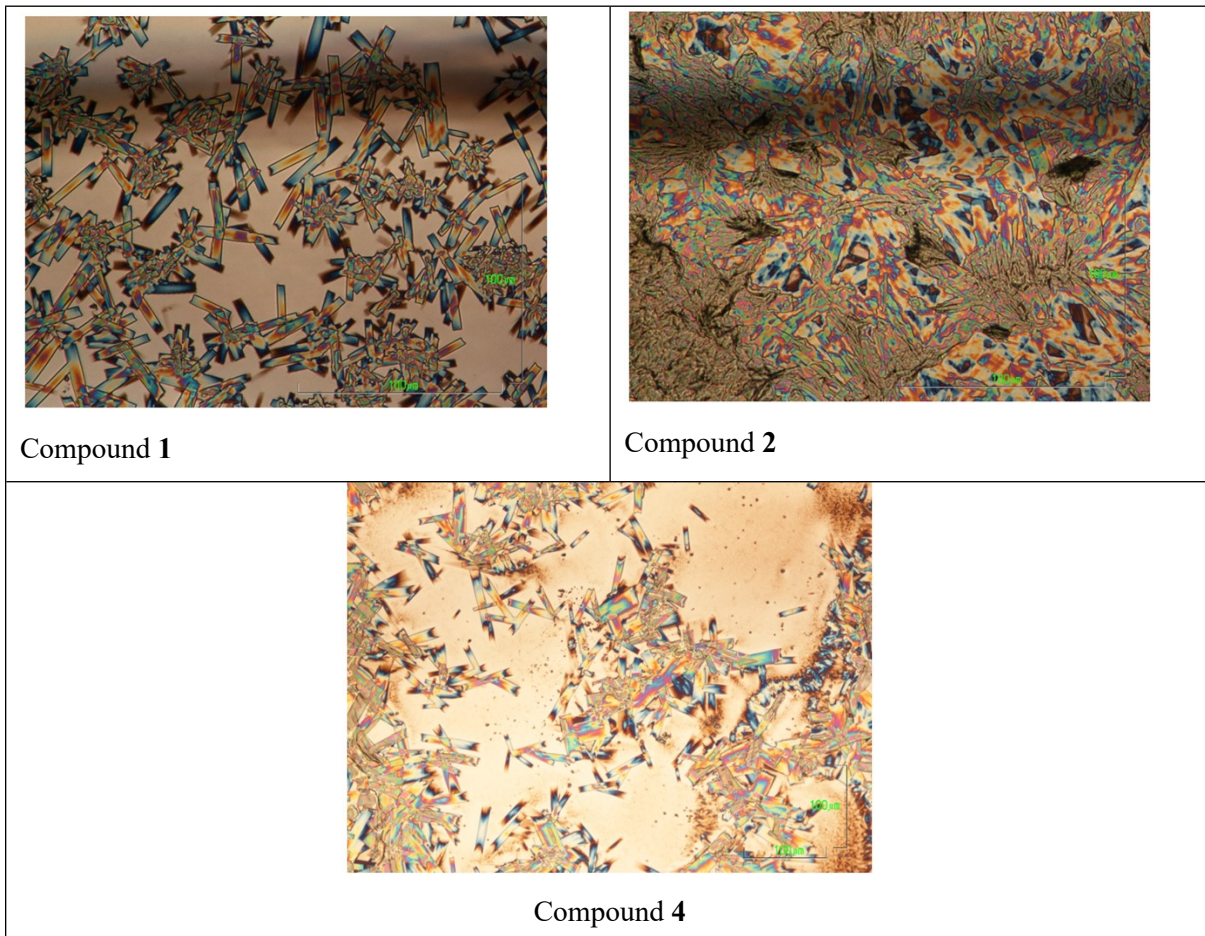


Figure S43 Thin deposit of **1**, **2** and **4** grown by drop casting on silicon surface.

The chemical composition before and after sublimation for compounds **1** and **2** was probed by XPS as shown in following Figure S44- Figure S51. The bulk and after sublimation compound 1 spectrum exhibited photoelectron peaks—Co 2p, Cl 2p, N 1s, C 1s, and O 1s. The bulk compound **2** spectrum exhibited photoelectron peaks—Co 2p, Br 3d, N 1s, C 1s, and O 1s. Carbon and oxygen contributions were discarded since they are affected by adventitious contaminations due to the *ex situ* sample preparation procedures. The detailed spectra of the selected peaks revealed specific chemical bonds. The N 1s peak was deconvoluted to two components: pyridinic N and pyrrolic N.³¹ The photoelectron peaks emitted from the p, d, and f electronic levels are further split by spin-orbit interactions. This helped us to distinguish, in the Cl 2p and Br 3d spectrum, between organic and inorganic components.³² Co 2p exhibited two main components and shake-up satellites. The spin-orbit shift of the main components Co 2p_{3/2} and Co 2p_{1/2} depends on the oxidation state, and with 15.8 eV, the Co(II) high-spin state predominates.³³

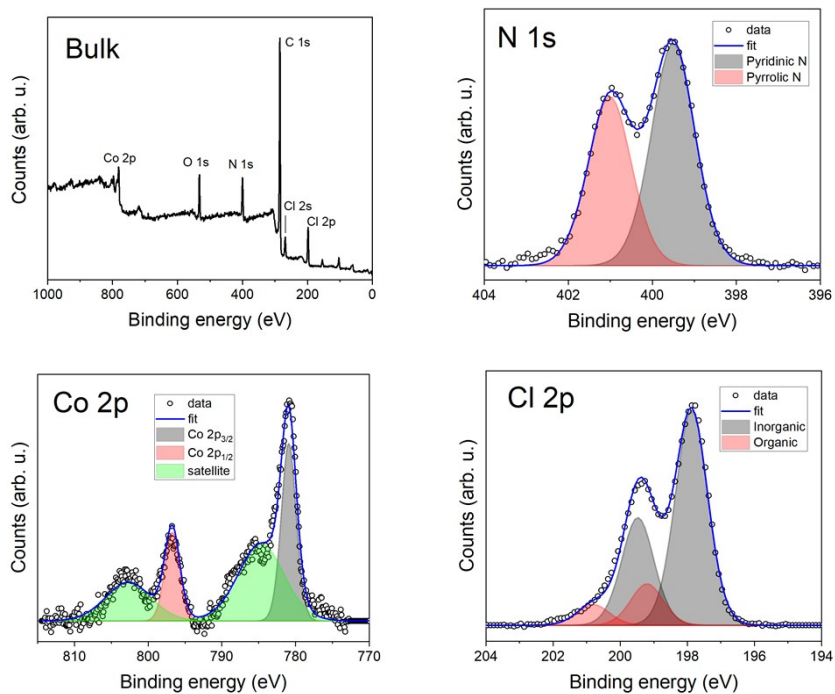


Figure S44 Survey and detailed XPS spectra for bulk as-synthesized compound 1.

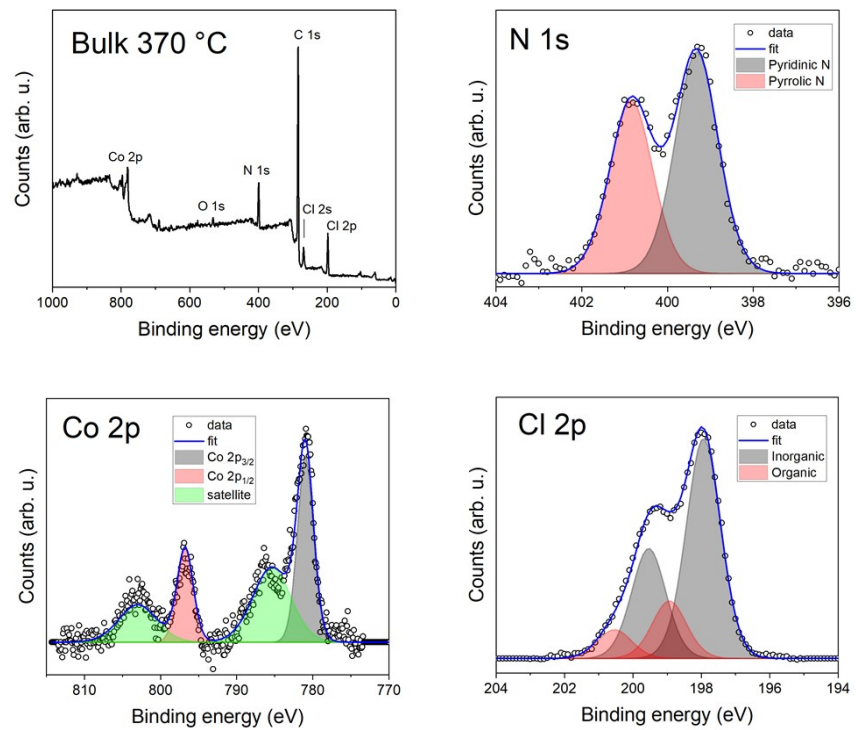


Figure S45 Survey and detailed XPS spectra for bulk compound 1 powder taken from crucible after sublimation at 370 °C.

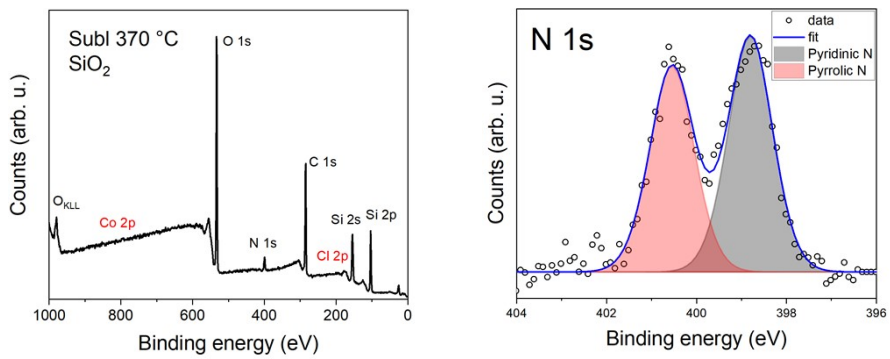


Figure S46 Survey and detailed XPS spectra for sublimated compound **1** on SiO₂ wafer. There were no Co 2p nor Cl 2p detected. A partial decomposition of compound **1** on the surface was observed.

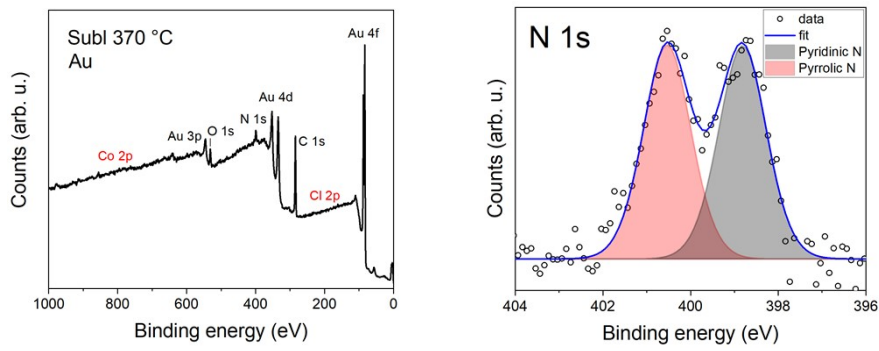


Figure S47 Survey and detailed XPS spectra for sublimated compound **1** on Au substrate. There were no Co 2p nor Cl 2p detected. A partial decomposition of compound **1** on the surface was observed.

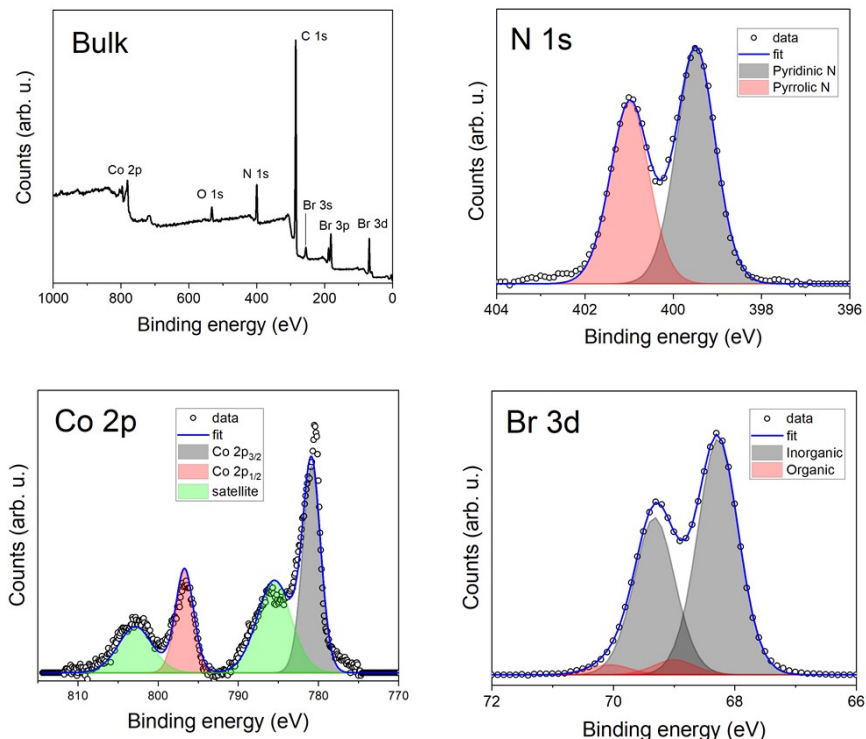


Figure S48 Survey and detailed XPS spectra for bulk as-synthesized compound 2.

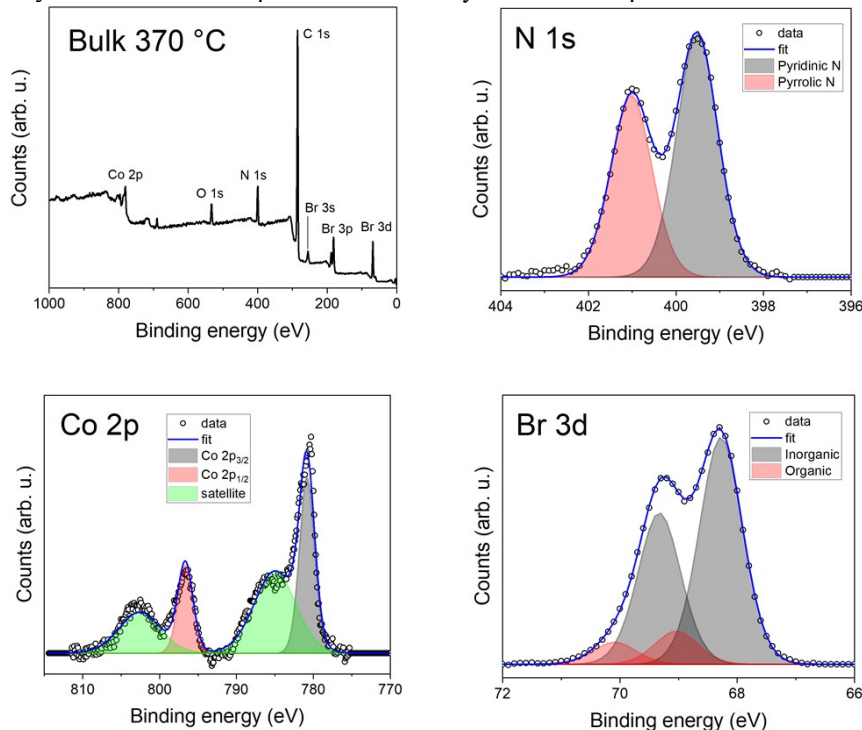


Figure S49 Survey and detailed XPS spectra for bulk compound 2 powder taken from crucible after sublimation at 370 °C.

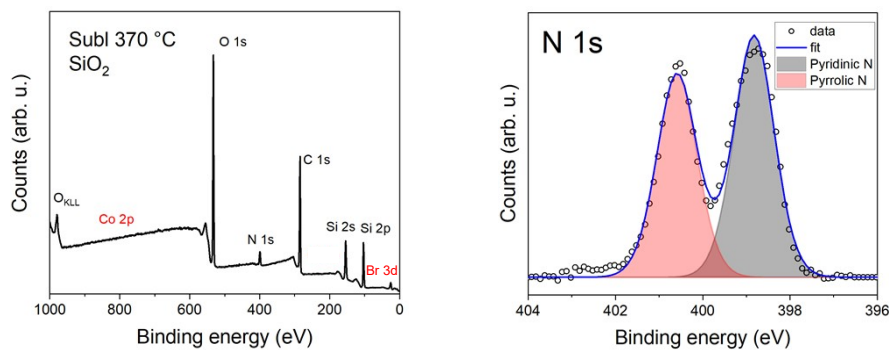


Figure S50 Survey and detailed XPS spectra for sublimated compound 2 on SiO₂ wafer. There were no Co 2p nor Br 3d detected. A partial decomposition of compound 2 on the surface was observed.

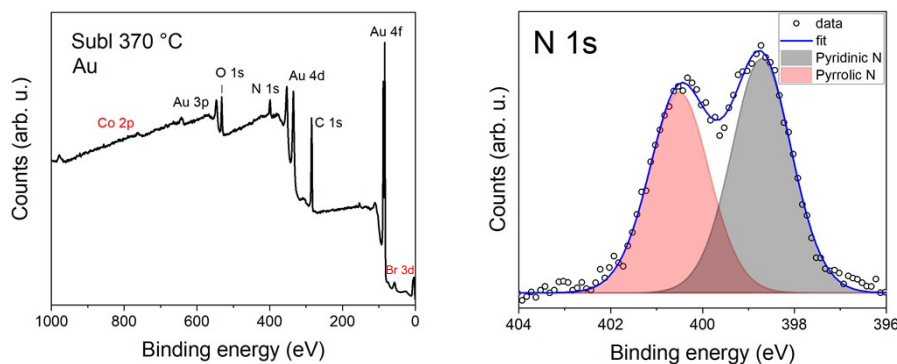


Figure S51 Survey and detailed XPS spectra for sublimated compound **2** on Au substrate. There were no Co 2p nor Br 3d peaks detected. A partial decomposition of compound **2** on the surface was observed.

References

1. A. Addison, P. Burke, Synthesis of Some Imidazole- and Pyrazole- Derived Chelating Agents, *J. Heterocycl. Chem.* **1981**, 18, 803–805.
2. M.C. Burla, R. Caliandro, M. Camalli, B. Carrozzini, G.L. Cascarano, C. Giacovazzo, M. Mallamo, A. Mazzzone, G. Polidori, R. Spagna, SIR2011: a new package for crystal structure determination and refinement. *J. Appl. Crystallogr.* **2012**, 45, 357-361.
3. G.M. Sheldrick, SHELXT - Integrated space-group and crystal-structure determination. *Acta Crystallogr. Sect. A* **2015**, A71, 3-8.
4. G.M. Sheldrick, Crystal structure refinement with SHELXL. *Acta Crystallogr. Sect. C* **2015**, C71, 3-8.
5. O.V. Dolomanov, L.J. Bourhis, R.J. Gildea, J.A.K. Howard, H. Puschmann, OLEX2: a complete structure solution, refinement and analysis program. *J. Appl. Crystallogr.* **2009**, 42, 339-341.
6. R. Boča, Theoretical Foundations of Molecular Magnetism, Elsevier, Amsterdam, 1999.
7. N. F. Chilton, R. P. Anderson, L. D. Turner, A. Soncini, K. S. Murray, PHI: a powerful new program for the analysis of anisotropic monomeric and exchange-coupled polynuclear d- and f-block complexes. *J. Comput. Chem.*, **2013**, 34 (13), 1164-1175.
8. F. Neese, Software update: the ORCA program system, version 4.0. *WIREs Comput. Mol. Sci.* **2018**, 8 (1), 1327.
9. P. A. Malmqvist, B. O. Roos, The CASSCF state interaction method. *Chem. Phys. Lett.* **1989**, 155 (2), 189–194.
10. (a) C. Angeli, R. Cimiraglia, J.-P. Malrieu, N-electron valence state perturbation theory: a fast implementation of the strongly contracted variant. *Chem. Phys. Lett.* **2001**, 350 (3-4), 297–305. (b) C. Angeli, R. Cimiraglia, S. Evangelisti, T. Leininger, J.-P. Malrieu, Introduction of n-electron valence states for multireference perturbation theory. *J. Chem. Phys.* **2001**, 114 (23), 10252–10264. (c) C. Angeli, R. Cimiraglia, J.-P. Malrieu, N-electron valence state perturbation theory: A spinless formulation and an efficient implementation of the strongly contracted and of the partially contracted variants. *J. Chem. Phys.* **2002**, 117 (20), 9138–9153.
11. T. Nakajima, The Douglas–Kroll–Hess Approach. *Chem. Rev.* **2012**, 112 (1), 385-402.
12. R. Izsak, F. Neese, An overlap fitted chain of spheres exchange method. *J. Chem. Phys.* **2011**, 135 (14), 144105.
13. F. Weigend, M. Kattanneck, R. Ahlrich R. Approximated electron repulsion integrals: Cholesky decomposition versus resolution of the identity methods *J. Chem. Phys.*, **2009**, 130, p. 164106.
14. F. Weigend, R. Ahlrichs, Balanced basis sets of split valence, triple zeta valence and quadruple zeta valence quality for H to Rn: Design and assessment of accuracy. *Phys. Chem. Chem. Phys.* **2005**, 7 (18), 3297-3305.
15. G. L. Stoychev, A. A. Auer, F. Neese, Automatic Generation of Auxiliary Basis Sets. *J. Chem. Theory Comput.* **2017**, 13 (2), 554-562.
16. S. Grimme, J. G. Brandenburg, C. Bannwarth, A. Hansen, Consistent structures and interactions by density functional theory with small atomic orbital basis sets. *J. Chem. Phys.* **2015**, 143 (5), 054107.
17. D. Ganyushin, F. Neese, First-principles calculations of zero-field splitting parameters. *J. Chem. Phys.* **2006**, 125 (2), 024103.
18. F. Neese, F. Efficient and accurate approximations to the molecular spin-orbit coupling operator and their use in molecular g-tensor calculations. *J. Chem. Phys.* **2005**, 122 (3), 034107.
19. R. Maurice, R. Bastardis, C. de Graaf, N. Suaud, T. Mallah, N. Guihéry, Universal Theoretical Approach to Extract Anisotropic Spin Hamiltonians. *J. Chem. Theory Comput.* **2009**, 5 (11), 2977–2984.
20. M. Cavallini, D. Gentili, P. Greco, F. Valle, F. Biscarini, *Nature Protocols*, **2012**, 7, 1668-1676.
21. Shirley, D. A. High-Resolution x-Ray Photoemission Spectrum of the Valence Bands of Gold. *Phys. Rev. B* **1972**, 5 (12), 4709–4714.
22. T. Jurca, A. Farghal, P. Lin, I. Korobkov, M. Murugesu, D. S. Richeson, Single-Molecule Magnet Behavior with a Single Metal Center Enhanced through Peripheral Ligand Modifications. *J. Am. Chem. Soc.* **2011**, 133, 15814-15817.
23. Atanasov, M.; Ganyushin, D.; Sivalingam, K.; Neese, F. In *Molecular Electronic Structures of Transition Metal Complexes II*; Mingos, D. M. P., Day, P., Dahl, J. P., Eds.; Springer Berlin Heidelberg: Berlin, Heidelberg, **2012**; pp 149– 220.
24. B. N. Figgis, M. A. Hitchman. Ligand Field Theory and Its Applications, Wiley-VCH, New York, 2000.
25. Banci, L.; Bencini, A.; Benelli, C.; Gatteschi, D.; Zanchini, C. Spectral-Structural Correlations in High-Spin Cobalt(II) Complexes. *Struct. Bond.* **1982**, 52: 37-86.

26. Marbey, J., Kragskow, J. G. C., Buch, C. D., Nehrkorn, J., Ozerov, M., Piligkos, S., et al. Vibronic Coupling in a Molecular 4f Qubit. *ChemRxiv*. Cambridge: Cambridge Open Engage; 2021; This content is a preprint and has not been peer-reviewed. [10.26434/chemrxiv.13725904.v1](https://doi.org/10.26434/chemrxiv.13725904.v1)
27. D. H. Moseley, S. E. Stavretis, K. Thirunavukkuarasu, M. Ozerov, Y. Cheng, L. L. Daemen, J. Ludwig, Z. Lu, D. Smirnov, C. M. Brown, A. Pandey, A. J. Ramirez-Cuesta, A. C. Lamb, M. Atanasov, E. Bill, F. Neese, Z. Xue, Spin–phonon couplings in transition metal complexes with slow magnetic relaxation. *Nat Commun* 2018, 9, 2572.
28. A. K. Mondal, T. Goswami, A. Misra, S. Konar, *Inorg. Chem.* **2017**, 56, 6870.
29. C. Rajnák, F. Varga, J. Titěš, J. Moncoľ, R. Boča, *Eur. J. Inorg. Chem.* **2017**, 1915–1922.
30. B. Brachňáková, S. Matejová, J. Moncol, R. Herchel, J. Pavlik, E. Moreno-Pineda, M. Ruben, I. Šalitroš *Dalton Trans.*, 2020, 49, 1249.
31. T. J. Woods, M. F. Ballesteros-Rivas, S. Gomez-Coca, E. Ruiz, K. R. Dunbar *J. Am. Chem. Soc.* **2016**, 138, 16407–16416.
32. Stańczyk, K.; Dziembaj, R.; Piwowarska, Z.; Witkowski, S. Transformation of Nitrogen Structures in Carbonization of Model Compounds Determined by XPS. *Carbon N. Y.* **1995**, 33 (10), 1383–1392.
33. Fiedler, R.; Herzschuh, R. An XPS Investigation of the Effects of Heat Treatment on the Chlorine Surface Chemistry of Some Lignites. *Fuel* **1993**, 72 (11), 1501–1505.
34. Poneti, G.; Mannini, M.; Cortigiani, B.; Poggini, L.; Sorace, L.; Otero, E.; Sainctavit, P.; Sessoli, R.; Dei, A. Magnetic and Spectroscopic Investigation of Thermally and Optically Driven Valence Tautomerism in Thioether-Bridged Dinuclear Cobalt-Dioxolene Complexes. *Inorg. Chem.* **2013**, 52 (20), 11798–11805.